A study on axially rotating pipe and swirling jet flows

by

Luca Facciolo

February 2006
Technical Reports from
Royal Institute of Technology
Department of Mechanics
S-100 44 Stockholm, Sweden

Akademisk avhandling som med tillstånd av Kungliga Tekniska Högskolan i Stockholm framlägges till offentlig granskning för avläggande av teknologie doktorsexamen fredagen den 10:e mars 2006 kl 10.15 i Sal E3, Osquars backe 14, KTH, Stockholm.

Universitetsservice US AB, Stockholm 2006

A Giuseppe e Angiolina

Luca Facciolo 2006 A study on axially rotating pipe and swirling jet flows
KTH Mechanics
S-100 44 Stockholm, Sweden

Abstract

The present study is an experimental and numerical investigation on rotating flows. A special facility has been built in order to produce a turbulent swirling jet generated by a fully developed rotating pipe flow and a Direct Numerical Simulation (DNS) code has been used to support and to complemen the experimental data. The work is so naturally divided into two main parts: the turbulent rotating pipe flow and the swirling jet.

The turbulent pipe flow has been investigated at the outlet of the pipe both by hot-wire anemometry and Laser Doppler Velocimetry (LDV). The LDV has also been used to measure the axial velocity component inside the pipe. The research presents the effects of the rotation and Reynolds number ($12000 \leqslant Re \leqslant 33500$) on a turbulent flow and compares the experimental results with theory and simulations. In particular a comparison with the recent theoretical scalings by Oberlack (1999) is made.

The rotating pipe flow also represents the initial condition of the jet. The rotation applied to the jet drastically changes the characteristics of the flow field. The present experiment, investigated with the use of hot-wire, LDV and stereoscopic Particle Image Velocimerty (PIV) and supported by DNS calculation, has been performed mainly for weak swirl numbers ($0 \leqslant S \leqslant 0.5$). All the velocity components and their moments are presented together with spectra along the centreline and entrainment data.

Time resolved stereoscopic PIV measurement showed that the flow structures within the jet differed substantially between the swirling and no swirling cases.

The research had led to the discovery of a new phenomenon, the formation of a counter rotating core in the near field of a swirling jet. Its presence has been confirmed by all the investigation techniques applied in the work.

Descriptors: Fluid mechanics, rotating pipe flow, swirling jet, turbulence, hot-wire anemometry, LDV, Stereo PIV, DNS.

Parts of this work has been published at:

Facciolo, L. Tillmark, N. & Talamelli, A. 2003 Experimental investigation of jets produced by rotating fully developed pipe flow, *TSFP3 conference proceedings*, 1217–1222.

Facciolo, L. & Alfredsson, P. H. 2004 The counter-rotating core of a swirling turbulent jet issued from a rotating pipe flow, *Phys. Fluids 16*, L71-L73

Facciolo, L. Orlandi, P. & Alfredsson, P. H. 2005 Swirling jet issued form fully developed rotating pipe flow - experiments and numerics, *TSFP4 conference proceedings*, 1243-1248

The work has also been orally presented at:

The Swedish mechanics days, 11-13 June 2001 *Linköping, Sweden*
APS meeting, 21-23 November 2004 *Seattle, WA, USA*
APS meeting, 20-22 November 2005, *Chicago, IL, USA*

Contents

CHAPTER 1

Introduction

1.1. Background and motivation

A jet is, by definition, a fluid stream forced under pressure out of an opening or nozzle. Applications of such flow can be found in nature, for instance the propulsion system of many marine animals like coelenterates, volcanos emissions, as well as in many technical applications like fountains, fluid injection engines, aircraft propulsion, cooling systems.

Swirling jets, where an azimuthal velocity is superimposed on the axial flow, are of importance in many technical and industrial applications. For instance, they are used in combustion systems both to enhance the forced convective cooling, to increase turbulent mixing of fuel with air and to stabilize the flame. Despite the importance of this type of flow and the large number of studies carried out in the past, there is still a lack of experimental data over a wide range of Reynolds number and swirl ratios, to both enhance the physical understanding of this type of flow as well as to assist in evaluating turbulence models and the development of Computational Fluid Dynamics (CFD) codes. A large number of the previous experimental investigations has used short stationary pipes with blades or vanes at the outlet to attain a swirling jet profile which therefore contains traces of the swirl generator, hence perturbing the axial symmetry of the flow. In order to increase flow homogeneity and to decrease the influence of upstream disturbances, axi-symmetric contractions are sometimes used before the jet exit. However, in this way, swirled jets with top-hat exit profiles, characterized by thin mixing layers, are obtained. These type of jets may differ significantly from several industrial applications where fully developed pipe flow may better represent the real boundary conditions.

This thesis reports measurements and analysis both of the flow field in a fully developed rotating pipe as well as the resulting flow field of the emanating jet. This work is part of a larger project aimed at the studying of the effects of the impingement of a turbulent swirling jet on a flat plate, positioned relatively close to the pipe exit. For this reason the present experimental study is limited to the analysis of the initial near-exit and intermediate (or transitional) region.

1.2. Layout of the thesis

The thesis is organised in two parts: the study of the rotating pipe flow and the study of the swirling jet. Chapter 2 states the equations of the motion (i.e.

continuity and Navier-Stokes equations) in a cylindrical coordinate system and also derives some integral relations for the two flow fields.

Chapters 3 and 4 present a part of the literature dedicated respectively to the rotating pipe flow and to the axisymmetric jet with and without a swirl component. The reviews include experiments, simulations, theoretical analysis and models.

Chapter 5 is dedicated to the description of the experimental apparatus built at the Fluid Physics Laboratory of KTH Mechanics and to the introduction of measurement techniques used to perform the experiments. Chapter 6, in a parallel way, introduces the numerical tool used in the study to corroborate and to help in the interpretation of the experimental data.

In Chapter 7 all the results for the pipe flow are presented. This also represents the initial stage of the jet. Data from the experiments are compared with the simulations results and theoretical studies. Chapter 8 is addressed to the investigation of the jet flow at moderate swirl numbers in the near field region. Data and analysis for all the three velocity components are presented which have been obtained using different measurement techniques as well as numerical simulation. Chapter 8 ends with the presentation of a new and unexpected phenomenon: the presence of a counter rotating core in the near field of the swirling jet. Chapter 9 includes the discussion and the conclusions of the present work.

CHAPTER 2

Theoretical considerations

2.1. Equations of motion

We will here first give the Navier-Stokes equations in cylindrical coordinates, and thereafter use Reynolds' decomposition to obtain the equations for the mean flow. When studying rotating flows it is possible to either use an inertial frame (laboratory fixed) or a rotating frame. In the first choice the rotation is felt through the boundary conditions, in the second the rotation is taken into account by adding body forces due to centrifugal and Coriolis effects. We write the equations in a general form in cylindrical coordinates such that both approaches will be possible. We denote the radial, azimuthal and axial directions with (r, θ, x) and the respective velocity components with (w, v, u), respectively. In the following we assume that the rotation is along the axial direction (in the laboratory frame the rotation vector can hence be written $\mathbf{\Omega} = \Omega \mathbf{e_x}$). Furthermore we assume that the flow is incompressible, i.e. the density ρ is constant as well as the temperature. As a consequence also the kinematic viscosity (ν) is constant. With these assumptions the conservation equation of mass (continuity equation) becomes

$$\frac{\partial w}{\partial r} + \frac{w}{r} + \frac{1}{r}\frac{\partial v}{\partial \theta} + \frac{\partial u}{\partial x} = 0 \tag{2.1}$$

whereas the conservation of momentum (Navier-Stokes equations) can be written

$$\begin{aligned} &\frac{\partial w}{\partial t} + w\frac{\partial w}{\partial r} + \frac{v}{r}\frac{\partial w}{\partial \theta} + u\frac{\partial w}{\partial x} - \frac{v^2}{r} = \\ -&\frac{1}{\rho}\frac{\partial p}{\partial r} + \nu\left(\mathcal{D}w - \frac{w}{r^2} - \frac{2}{r^2}\frac{\partial v}{\partial \theta}\right) - 2\Omega v \end{aligned} \tag{2.2}$$

$$\begin{aligned} &\frac{\partial v}{\partial t} + w\frac{\partial v}{\partial r} + \frac{vw}{r} + \frac{v}{r}\frac{\partial v}{\partial \theta} + u\frac{\partial v}{\partial x} = \\ -&\frac{1}{\rho r}\frac{\partial p}{\partial \theta} + \nu\left(\mathcal{D}v - \frac{v}{r^2} + \frac{2}{r^2}\frac{\partial w}{\partial \theta}\right) + 2\Omega w \end{aligned} \tag{2.3}$$

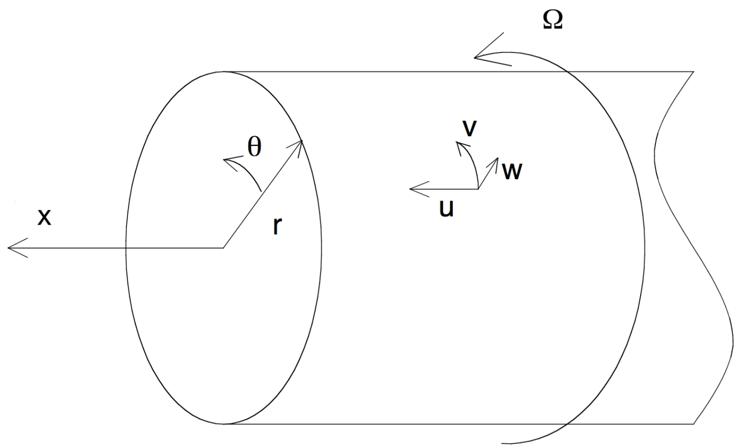

FIGURE 2.1. Coordinate system.

$$\frac{\partial u}{\partial t} + w\frac{\partial u}{\partial r} + \frac{v}{r}\frac{\partial u}{\partial \theta} + u\frac{\partial u}{\partial x} = -\frac{1}{\rho}\frac{\partial p}{\partial x} + \nu \mathcal{D} u \tag{2.4}$$

where

$$\mathcal{D} = \frac{\partial^2}{\partial r^2} + \frac{1}{r}\frac{\partial}{\partial r} + \frac{1}{r^2}\frac{\partial^2}{\partial \theta^2} + \frac{\partial^2}{\partial x^2}$$

The Coriolis term ($2\mathbf{\Omega} \times \mathbf{u}$) is zero in an inertial (laboratory fixed) coordinate system. We now proceed with the Reynolds' decomposition typically used for turbulent flows

$$\begin{aligned} w &= W + w' \\ v &= V + v' \\ u &= U + u' \\ p &= P + p' \end{aligned}$$

where capital letters denote mean quantities and primed variables are fluctuating variables with zero mean. Putting the decomposition into eqs. (2.1)–(2.4) and assuming that the mean flow is steady and axisymmetric, i.e.

$$\frac{\partial}{\partial t} = 0, \qquad \frac{\partial}{\partial \theta} = 0. \tag{2.5}$$

we obtain for the Reynolds averaged continuity equation

$$\frac{\partial W}{\partial r} + \frac{W}{r} + \frac{\partial U}{\partial x} = 0 \tag{2.6}$$

The Reynolds averaged Navier-Stokes equations in the inertial coordinate system become (in the following we are skipping the prime on fluctuating components and averaging is denoted by an overbar)[1]

$$W\frac{\partial W}{\partial r} + U\frac{\partial W}{\partial x} + \frac{\partial}{\partial r}\overline{w^2} + \frac{\partial \overline{uw}}{\partial x} - \frac{1}{r}\left(V^2 + \overline{v^2} - \overline{w^2}\right) = -\frac{1}{\rho}\frac{\partial P}{\partial r} + \frac{1}{r^2}\frac{\partial}{\partial r}\left[\nu r^3 \frac{\partial}{\partial r}\left(\frac{W}{r}\right)\right] \tag{2.7}$$

$$U\frac{\partial V}{\partial x} + W\frac{\partial V}{\partial r} + \frac{VW}{r} + \frac{\partial \overline{uv}}{\partial x} + \frac{1}{r^2}\frac{\partial}{\partial r}\left(r^2\overline{vw}\right) = \frac{1}{r^2}\frac{\partial}{\partial r}\left[\nu r^3 \frac{\partial}{\partial r}\left(\frac{V}{r}\right)\right] \tag{2.8}$$

$$U\frac{\partial U}{\partial x} + W\frac{\partial U}{\partial r} + \frac{1}{r}\frac{\partial}{\partial r}\left(r\overline{uw}\right) + \frac{\partial}{\partial x}\overline{u^2} = -\frac{1}{\rho}\frac{\partial P}{\partial x} + \frac{1}{r}\frac{\partial}{\partial r}\left[\nu r \frac{\partial U}{\partial r}\right] \tag{2.9}$$

Equations (2.7)–(2.9) can be further simplified depending on the flow situation studied. In a boundary layer approximation, i.e. derivatives in the x-direction are small as compared to derivatives in the r-direction, and $U >> W$, several of the convective terms may be neglected. In the case of a x-independent pipe flow there is no streamwise variation of mean quantities so x-derivatives are identically zero. For high Reynolds number flows the viscous term may also be neglected except if there is a boundary at a solid surface. We will in the following specialize first to an axially rotating pipe flow and secondly to a swirling jet, which makes it possible to derive some analytical results for these cases.

[1] The equations for the Reynolds stresses in a rotating frame are reported in Appendix A.

2.1.1. *Specializing to rotating pipe flow*

For the fully developed pipe flow there is no streamwise variation of the mean quantities (except for the pressure although $\partial P/\partial x=$ constant) which immediately gives from the continuity equation (2.6) that $W = 0$ for all r. The boundary conditions on the pipe wall are in the laboratory fixed coordinate system:

$$W(R) = 0, \quad V(R) = V_w, \quad U(R) = 0, \tag{2.10}$$

where $V_w = \Omega R$ is the velocity of the pipe wall. Due to symmetry the following conditions have to apply on the pipe axis

$$W(0) = 0, \quad V(0) = 0, \quad \frac{\partial U}{\partial r}(0) = 0 \tag{2.11}$$

Equation (2.8) can now be rewritten as

$$\nu\left(\frac{d^2V}{dr^2} + \frac{1}{r}\frac{dV}{dr} - \frac{V}{r^2}\right) = \frac{d}{dr}(\overline{vw}) + 2\frac{\overline{vw}}{r} \tag{2.12}$$

Equation (2.12) can be integrated twice, first from 0 to r, and thereafter from r to R (using the boundary conditions) to give (Wallin & Johansson 2000)

$$V(r) = V_w\frac{r}{R} - \frac{r}{\nu}\int_r^R \overline{vw}\frac{dr}{r} \tag{2.13}$$

The first term on the right hand side represents the solid body rotation whereas the second term gives the contribution from the Reynolds stress term $\overline{vw}$. This implies that if $\overline{vw} \neq 0$ the turbulence gives rise to a deviation from the solid body rotation. Furthermore, eq. (2.9) can be substantially simplified giving

$$0 = u_\tau^2\frac{r}{R} - \overline{uw} + \nu\frac{dU}{dr} \tag{2.14}$$

where u_τ is the friction velocity determined from the streamwise velocity gradient at the pipe wall $\tau_w{=}\mu\frac{du}{dy}|_{y=0}{=}\rho u_\tau^2$ (or equivalently the pressure drop along the pipe $u_\tau = \sqrt{\left|\frac{\partial P}{\partial x}\right|/2}$).

So far we have discussed the equations of motion in their dimensional form. However they can all be written in non-dimensional form by using only two non-dimensional numbers, namely the Reynolds number

$$Re = \frac{U_b D}{\nu} \tag{2.15}$$

and the swirl number

$$S = \frac{V_w}{U_b} \tag{2.16}$$

where U_b is the bulk velocity in the pipe, i.e. the mean velocity over the pipe area. Eq. (2.13) then becomes

$$\frac{V(r)}{V_w} = \frac{r}{R}\left(1 - \frac{Re}{2S}\int_r^R \frac{\overline{vw}}{U_b^2}\frac{dr}{r}\right) \tag{2.17}$$

2.1.2. *Specializing to swirling jet flow*

The turbulent axisymmetric jet flow is more complicated than the pipe flow since it is developing in the streamwise direction. This also means that $W \neq 0$. However it is possible to use a boundary layer type of analysis such that some terms can be safely assumed to be small. In this way we can simplify eq. (2.7) to become

$$\frac{1}{\rho}\frac{\partial P}{\partial r} = -\frac{\partial}{\partial r}\overline{w^2} + \frac{1}{r}\left(V^2 + \overline{v^2} - \overline{w^2}\right) \tag{2.18}$$

For the turbulent axisymmetric jet flow we preserve the condition of symmetry at the centreline (r=0) and add the boundary conditions at infinity (r=∞):

$$U = 0, \quad V = 0, \quad W = 0, \quad \frac{\partial}{\partial r} = 0 \tag{2.19}$$

From the Reynolds averaged Navier-Stokes equations, multiplying the axial component (eq. 2.9) and the radial component (eq. 2.18) respectively by r and by r^2, then integrating between $r = 0$ and $r = \infty$ and applying the boundary conditions (2.19), we obtain (Chigier & Chervinsky 1967):

$$\frac{d}{dx}\int_0^\infty r[(P - P_\infty) + \rho(U^2 + \overline{u^2})]dr = 0 \tag{2.20}$$

$$\int_0^\infty r(P - P_\infty)dr = -\frac{1}{2}\rho\int_0^\infty r(V^2 + \overline{v^2} + \overline{w^2})dr \tag{2.21}$$

From the above equations, assuming that the squared fluctuating velocity components are negligible with respect to the squared mean components, we get the conservation of the flux of the axial momentum

$$\frac{d}{dx}\left[2\pi\rho\int_0^\infty r\left(U^2 - \frac{1}{2}V^2\right)dr\right] = \frac{d}{dx}G_x = 0 \tag{2.22}$$

In the same way, starting from the azimuthal component (eq. 2.8) of the Reynolds averaged Navier-Stokes equations, neglecting $\partial\overline{uv}/\partial x$ and assuming that the Reynolds number is large ($\nu \to 0$), multiplying by r^2 and integrating, we get an expression for the conservation of the angular momentum

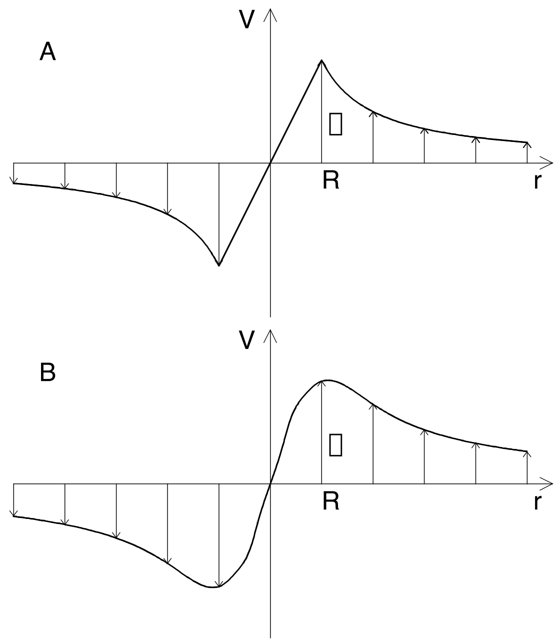

FIGURE 2.2. a) Rankine vortex, b) Batchelor vortex.

$$\frac{d}{dx}\left(2\pi\rho\int_0^\infty r^2 UV dr\right) = \frac{d}{dx}G_\theta = 0 \tag{2.23}$$

By using the above quantities it is possible to characterize the swirling flow with an integral swirl number:

$$S_{\theta x} = \frac{G_\theta}{G_x R}. \tag{2.24}$$

2.1.3. *Vortex Models*

The distribution of the azimuthal velocity in a real jet is mainly due to the method used to generate the swirl. From a mathematical point of view, it is possible to create models to properly approximate the behaviour of the flow field.

A Rankine vortex represents a simply model for rotating flow (figure 2.1.3a). It displays a solid body rotation core followed by a r^{-1} decay in the radial direction. In application to a swirling jet, it is worth noting that the model does not take into account the finite thickness of the shear layer region at $r = R$ where the curve has a singularity.

$$V = \Lambda r, \quad 0 \leqslant r \leqslant R \tag{2.25}$$

$$V = \frac{\Lambda R^2}{r} \tag{2.26}$$

A more suitable model for developed swirling flows is the Batchelor vortex (figure 2.1.3b). The azimuthal velocity field is described via a similarity solution applied to wakes and jets in the far field. In a non-dimensional formulation the velocity has a maximum ($V = \Lambda$) for $r = 1.121$.

$$V = \frac{\Lambda}{0.638} \frac{1 - e^{-r^2}}{r} \tag{2.27}$$

CHAPTER 3

Review of rotating pipe flow studies

The physics of rotating pipe flow is a challenge for experimental, theoretical, modelling and simulation studies despite its conceptual simplicity. A few experimental studies have been undertaken and there are also some direct numerical simulation studies available. However a large number of studies using rotating turbulent pipe flow as a test case for modelling can be found in the literature.

First, it should be clearly stated that the effect of rotation on pipe flow is quite different depending on whether the flow is laminar or turbulent. In the laminar case rotation has a destabilizing effect and the critical Reynolds number is as low as 83 for linearized disturbances. Turbulent pipe flow on the other hand, is stabilized by rotation and for instance the pressure drop along the pipe decreases with increasing rotation rate. It should also be mentioned that in the laminar case the fluid approaches solid body rotation at some distance downstream the inlet, whereas for turbulent flow this is not the case. We will first give a brief review regarding the present state of results for rotating laminar pipe flow and then discuss the turbulent case, describing first the experimental work as well as DNS work, and finally discuss some of the modelling attempts.

3.1. Stability of laminar rotating pipe flow

There have been several studies regarding the stability of rotating pipe flow. For instance Howard & Gupta (1962) gave an inviscid stability criterion for rotating pipe flow which is valid for axisymmetric disturbances. More thorough studies were made by Pedley (1968, 1969) who investigated the linear stability of rotating pipe flow both through an inviscid as well as a viscous analysis. He showed that in the limit of high rotation rates the critical Reynolds number became as low as 83 and remarked that this may be surprising since both a fluid undergoing solid body rotation as well as the pipe flow itself are stable, but gave no physical interpretation of the results.

Toplosky & Akylas (1988) expanded on the previous results into the non-linear regime and showed that the instability was supercritical and that it would take the form of helical waves. Recently, Barnes & Kerswell (2000) confirmed these results and found that the helical waves may become unstable to three dimensional travelling waves. These studies also concluded that the disturbances could not be traced back to the non-rotating case, thereby they are not the source for transition in non-rotating pipe flow.

Experimental work for this case has been limited to a few studies. There are of course experimental problems to set up this flow since both the parabolic Poisueille profile as well as the solid body rotation will take some downstream distance from the inlet to become fully established. In the experiments by Nagib *et al.* (1971) a fairly short pipe was used ($L/D \approx 23$ so the parabolic profile was not fully developed), however the rotation was obtained by letting the fluid (water) pass through a porous material inside the rotating pipe, thereby efficiently bringing the fluid into rotation. They observed, from flow visualization and hot-film measurements, that the transitional Reynolds number decreased from 2500 to 900 when S increased from 0 to 3. A more recent study by Imao *et al.* (1992) shows details of the instabilities through both LDV-measurements and flow visualizations. They also demonstrate that the instability takes the form of spiral waves.

There are a few attempts to pinpoint the physical mechanism behind the instability in terms of a Rayleigh criterion or centrifugal instability, but as pointed out by Maslowe (1974) the theoretical analysis has so far not been able to shed light on this mechanism. To this end we will only point out a similarity of the basic flow field as seen in a non-rotating inertial frame with that giving rise to cross flow instabilities on a rotating disc or a swept wing.

3.2. Turbulent rotating pipe flow

3.2.1. *Experimental results*

The first experimental study of axially rotating pipe flow is probably that of White (1964) who showed that the pressure drop in the turbulent regime decreased with increasing rotation. He also did some flow visualization both illustrating the destabilization in the laminar case and the stabilization in the turbulent one.

Murakami & Kikuyama (1980) did their experiments in a water flow facility where the pipe diameter was 32 mm. They measured both the pressure drop as well as mean velocity profiles. For the pressure drop measurements they presented data for Reynolds numbers in the range $10^4 - 10^5$ and for rotation rates up to $S = 3$. The pressure tappings were placed in the stationary pipes upstream and downstream of the rotating section and the length of the rotating section could be varied by using interchangeable pipes of various lengths. The mean velocity in the streamwise and azimuthal directions were measured with a three-hole Pitot tube which was inserted through a stationary part of 5 mm length which could be placed at different positions from the inlet of the rotating pipe.

They found that when the pipe length is larger than 100 diameters, the ratio between the pressure loss coefficient for a rotating pipe and a non-rotating smooth pipe is governed only by the rate of rotation S. Beyond $S = 1.2$ the observed suppression of turbulence is saturated and the ratio of the loss coefficients remains unaltered. In the Reynolds range considered during the experiment ($10^4 < Re < 2 \cdot 10^5$), the axial velocity profiles gradually change in the downstream direction to become less full, i.e. the centreline velocity increases and the velocity gradient at the wall decreases. For $x/D > 120$ the velocity profile results were found to be approximately independent of the axial distance from the inlet. The change of the velocity profile is more accentuated with increasing S and tends towards the parabolic shape of a laminar flow. However the azimuthal velocity profiles at this position does not show solid body rotation, instead it has a shape which is nearly parabolic, $V/V_w = (r/R)^2$.

LDV-measurements were made by Kikuyama *et al.* (1983) who expanded the measurements by Murakami & Kikuyama (1980) to other pipe diameters (5 and 20 mm) and also presented velocity measurements taken by an LDV system. These results confirm the previous results that the mean flow tends to a parbolic profile when rotation is increased and that the azimuthal flow also becomes parabolic. Unfortunately no data on the turbulence fluctuations were presented. Similarily the experiments by Reich & Beer (1989) in the range $5000 < Re < 50000$ and S up to 5, showed mean profiles of both the streamwise and azimuthal directions obtained with a three-hole pressure probe which are in accordance with the earlier results. Also in this case only mean velocity data were obtained.

The LDV measurements by Imao *et al.* (1996) on the other hand supplied the first measurements of turbulence fluctuations and presented measured distributions on five of the Reynolds stresses as well as the mean profiles at $Re = 20000$. The measurements were made in water in a 30 mm diameter pipe at $120D$ dowstream the inlet. They also presented pressure drop measurements showing the decrease of the friction factor with increasing S. Their measurements confirmed the previously observed change in the streamwise velocity as well as the parabolic shape of the azimuthal velocity. If the normal Reynolds stresses ($\overline{uu}$, $\overline{vv}$, $\overline{ww}$) were normalised with the bulk velocity there was only a slight decrease with increasing rotation. The change in $\overline{uw}$ was on the other hand much more dramatic if normalized with the bulk velocity, but would more or less collapse if normalized with the friction velocity. $\overline{uv}$ is for the non-rotating case equal to zero due to symmetry, but was seen to become negative with rotation. A plausible explanation for this behaviour is that the normal velocity increases with r whereas the opposite is true for the streamwise velocity. A fluctuation that gives a radial displacement of a fluid element which keeps its momentum would hence give $u > 0$ and $v < 0$ (or vice versa) which would mean that the fluctuations would become negatively correlated.

3.2.2. *Numerical simulations*

Although experimental studies of rotating pipe flow have been performed since long, direct numerical simulations (DNS) and large eddy simulations (LES) of turbulent pipe flow have been reported only during the last decade. The first results from large eddy simulations seem those reported in the doctoral thesis of Eggels (1994). He did a simulation at Re=59500 and S=0.71. He found that the streamwise mean velocity increased in the centre of the pipe and a subsequent decrease at the wall, and hence a smaller friction coefficient. The azimuthal velocity showed the expected near-parabolic shape and the turbulent decreased, especially close to the pipe walls. The largest decrease was seen in the streamwise component.

Orlandi & Fatica (1997) on the other hand performed a DNS at $Re = 5000$ for four values of S, namely 0, 0.5, 1.0 and 2.0. They presented data for both the mean flow velocity and all six Reynolds stresses as well as some instantaneous flow field data. Orlandi (1997) used this data base to further evaluate various turbulent quantities. Later Orlandi & Ebstein (2000) made simulations at approximately the same Reynolds number but extended the rotation rates up to $N = 10$. In that case they especially focussed on presenting the turbulent budgets for different S.

The data of Orlandi & Fatica (1997) and Orlandi & Ebstein (2000) show that the friction factor decreases with about 15% when S is increased from 0 to 2. However for $S = 5$ the friction factor increase again and at $S = 10$ it is actually higher than for the non-rotating case. The streamwise velocity profiles show a similar behaviour as in the experiments described in section 3.2.1, the centreline velocity increases with S and the profile becomes less full. When scaling these profiles with the bulk velocity it has been noted that, keeping the Reynolds number constant and varying S, all the profiles collapse almost at the same value $U/U_b = 1.14$ at $r/R \approx 0.6$ presenting a good agreement with experimental data (the difference is referred to the effect of the entrance conditions). The azimuthal profile also shows the expected parabolic behaviour, except close to the wall, although there is a slight variation with S.

The results for the normal Reynolds stress components show that rotation gives a reduction of the near wall maximum in the streamwise component and a slight increase in the other two, especially in the central region of the pipe.

In a non-rotating pipe the only resulting shear stress is $\overline{uw}$. The simulation data show that when a rotation is introduced it is slightly reduced and there is an increase in $\overline{uv}$ and $\overline{vw}$ instead. The distribution of $\overline{vw}$ can be shown (see eq. 2.17) to be directly coupled to the azimuthal mean flow distribution and scales with S/Re and the calculated distributions show the expected shape. However the $\overline{uv}$ distribution has a strange behaviour for $S \geq 1$, with oscillations along the pipe radius. Orlandi & Fatica (1997) explain this with the large scale structures in the central region of the pipe for high S which means that the averaging time has to be increased to obtain stable distributions.

A recent DNS study was performed by Satake & Kunugi (2002) at a similar Reynolds number and values of S of 0.5, 1.0, 2.0 and 3.0. In that study a uniform heat flux was introduced at the wall and temperature distributions were also calculated. Their data show a monotonous decrease of the friction factor with increasing S. In addition to mean flow distributions and Reynolds stresses they present detailed turbulent budgets which are similar to those of Orlandi & Ebstein (2000), as well as similar profiles for the temperature fluctuations. It can be noted that their $\overline{uv}$-data also show oscillations in the same way as the data of Orlandi & Fatica (1997) for high S.

Finally two recent LES studies have also been published (Yang 2000; Feiz *et al.* 2003) which for suitable subgrid scale models to a large extent show good agreement with the DNS results.

3.2.3. *Theoretical and numerical modelling*

In a rotating pipe flow the rotation affects both the mean flow as well as the turbulent stresses. To some extent the stabilizing effect of the rotation can be taken into account in the models by introducing a correction in terms of a Richardson number. For instance Kikuyama *et al.* (1983) modelled the turbulence using Prandtls mixing length theory where the mixing length was modified, such that the stabilizing influence of rotation was taken into account through a Richardson number which involves the azimuthal velocity. Such an approach was first suggested by Bradshaw (1969), however in order to use this Kikuyama *et al.* had to assume that the azimuthal velocity had the experimentally observed parabolic shape. In their calculations they were able to obtain the observed change in the streamwise velocity distribution as well as the friction factor although with this approach the azimuthal velocity distribution is an input to the model and the modelling is therefore of somewhat limited value. Also the work by Weigand & Beer (1994) follows similar lines.

On the other hand it has been shown that the standard K-ϵ model cannot model even the streamwise mean flow correctly. For instance the results of Hirai, Takagi & Matsumoto (1988) show that it does not predict the changes in the streamwise velocity profile when $S \neq 0$ and the resulting azimuthal velocity becomes linear, i.e. the model predicts a solid body rotation of the flow. This is also true when the model is modified using a Richardson number to take into account the stabilizing effect of rotation. This issue has been thoroughly discussed by Speziale, Younis & Berger (2000).

Hirai *et al.* (1988) employed a Reynolds stress transport equation model which was shown to be able to give the correct tendency of the experimentally measured axial velocity profile as well as the tendency of the friction factor to decrease with increasing swirl. The laminarisation phenomenon is explained by the reduction of the turbulent momentum flux $\rho\overline{uw}$ due to the swirl, mainly caused by the negative production term $\overline{uv}V/r$ in the transport equation of $\overline{uw}$. Other attempts giving similar results using Reynolds stress transport models to calculate rotating turbulent pipe flow have been made by Malin & Younis (1997), Rinck & Beer (1998) and Kurbatskii & Poroseva (1999).

Both Speziale *et al.* (2000) and Wallin & Johansson (2000) developed algebraic Reynolds stress models which were applied to rotating pipe flow. They used different approaches to the modelling, for instance Speziale *et al.* worked in the rotating system, taking the rotation into account through the Coriolis force, whereas Wallin & Johansson used the inertial system (laboratory fixed). In that case the rotation effects come in through the rotating pipe wall (i.e.

through the boundary conditions). In both cases their models were able to qualitatively show the main features of rotation, namely the change in the streamwise velocity with S and the deviation from the solid body rotation of the azimuthal velocity distribution.

Finally the theoretical modelling of turbulent flows by Oberlack (1999, 2001) should be mentioned. He has, through a Lie group appoach to the Reynolds averaged Navier-Stokes equations, been able to derive new scaling laws for various turbulent flows, among them rotating pipe flow. Of particular interest for the present work is that Oberlack (1999) proposes certain scaling laws that can be checked against experiments. For instance the theory gives that the azimuthal mean velocity can be written as

$$\frac{V}{V_w} = \zeta \left(\frac{r}{R}\right)^{\psi} \tag{3.1}$$

which with $\zeta = 1$ and $\psi = 2$ corresponds to the parabolic velocity distribution. Furthermore the theory suggests a scaling law for the axial mean velocity which is

$$\frac{U_c - U}{u_\tau} = \chi\left(s\right)\left(\frac{r}{R}\right)^{\psi} \tag{3.2}$$

where χ is a function of the velocity ratio between the rotational speed of the pipe and the friction velocity s=V_w/u_τ. Note that the value of the exponent ψ in eqs. (3.1) and (3.2) is the same. A logarithmic law in the radial coordinate is also suggested from the theory, such that

$$\frac{U}{V_w} = \lambda \log\left(\frac{r}{R}\right) + \omega \tag{3.3}$$

This scaling law was checked against the data of Orlandi & Fatica (1997). Only data for one swirl number was shown (S=2), but a logarithmic region was found for $0.5 \leq r/R \leq 0.8$ with λ=–1.0. A final proposition from the theory is that there is one point where the mean axial velocity is independent of the Reynolds number. The data suggest that this fixed point is $r_{fix} = 0.75R$ and that the velocity is $U(r_{fix}) = U_b$. In the present study we will compare our experimental data with the predictions of Oberlack (1999).

CHAPTER 4

Review of axisymmetric jet flow studies

Jet flows with different geometries and boundary conditions have been widely investigated both experimentally and theoretically. The importance of this type of shear flow is related to numerous industrial applications (e.g. combustion, jet propulsion and cooling systems). This chapter contains an overview of work on swirling jet flows. In order to assess the main features and effects due to the presence of the rotational motion of the flow, a brief review concerning the main characteristics of axisymmetric non-swirling jets is also included.

4.1. The axisymmetric jet

An axisymmetric jet (see figure 4.1) is produced when fluid is ejected from a circular orifice into an external ambient fluid, which can be either at rest or co-flowing. Here we assume that the jet fluid and the ambient fluid are the same. At the nozzle exit, the high velocity jet generates a thin axisymmetric circular shear layer. The shear layer is rapidly subjected to a Kelvin-Helmoltz instability process (due to the presence of an inflectional point in the mean streamwise velocity distribution) and vortical structures are formed. Moving downstream the shear layer spreads in the radial direction both outwards and towards the centreline. The shear layer reaches the jet axis at a distance of approximately 4–5 diameters from the exit. The region inside the axisymmetric shear layer, characterized by an unchanged axial velocity, is called the jet "potential" core. The process described above is similar both for laminar and turbulent jet flows.

Further downstream, in the intermediate region of the jet, the different eddy structures interact in a non-linear behaviour engulfing fluid from the external environment and eventually collapse leaving the jet fully turbulent.

In the fully turbulent region, i.e. after approximately 20 diameters downstream the jet exit, the mean velocity profiles exhibit a self-preservation behaviour where the mean axial centreline velocity decays with the inverse of the distance. However, the turbulence intensity profiles require a much longer distance before reaching the self-preservation state, especially for the radial and tangential fluctuations. This is due to the fact that the energy is directly transferred from the mean flow to the streamwise fluctuations whereas energy to the other two components is transferred from the streamwise turbulence through the pressure-strain terms. Only after about 50–70 diameters the axisymmetric jet can be considered as truly self-preserving. For a review of turbulent jets

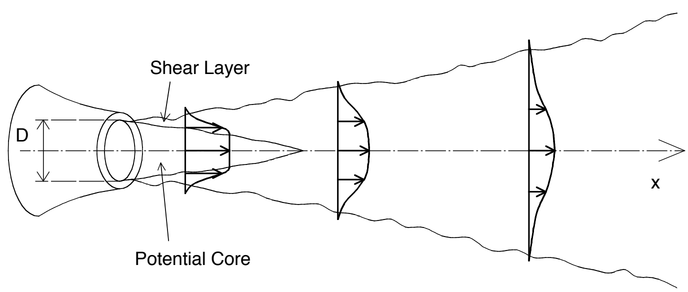

FIGURE 4.1. Schematic of the development of an axisymmetric jet.

the reader is referred to the monograph of Abramovich (1963) or to the more recent review article by Thomas (1991). Also a number of papers by George and co-workers (see for instance Jung, Gamard & George 2004) give interesting information on the development and flow structures of turbulent jets.

4.1.1. *The initial region*

The near field of an axisymmetric jet is dominated by the inviscid inflectional instability mechanism that amplifies upstream disturbances and generates large-scale vortical structures in the shear layer. The shape and characteristics of the structures depend on the type of the disturbances. In the initial region of naturally evolving jets it appears that axisymmetric disturbances are mostly amplified, giving rise to quasi-periodically spaced axisymmetric rings of concentrated vorticity.

Amplification factors and phase velocities depend on the main characteristics of the shear layer, such as the mean velocity profile and the thickness of the boundary layer at the jet exit. In particular, the frequency of the most amplified disturbances scales with the shear layer thickness and with the local velocity profile, but does not depend on the jet diameter (shear layer mode). Indeed Michalke (1984) in his review, shows that the instability at the exit of an axisymmetric jet can be treated as a planar shear layer instability if the ratio between the radius and the shear layer thickness is larger than 50. In such a case the instability mode behaves as if it is two-dimensional. Further downstream, the shear layer thickness of course increases and when it becomes of the same order as the jet radius, the curvature cannot be neglected anymore.

Moving downstream the structures start to merge and to interact creating even larger structures. This mechanism is the one by which the memory of the initial stability is gradually lost. At the end of the potential core the appropriate length scale of the instability becomes the jet diameter. The passage frequency of the large-scale structures in this region is referred as the preferred mode or jet column mode. This mode can be described by means of a non-dimensional frequency, $St = fD/U$ (Strouhal number), where f is the frequency, D the jet diameter and U the jet exit velocity. In the different experiments in the literature a quite broad range ($0.25 < St < 0.85$) of the jet column mode has been found. This disagreement between different experiments may be explained with the strong sensitivity of the jet instability to the upstream noise coming from the experimental set-up. Indeed, with this type of instability a wide range of frequencies is highly amplified.

Finally, it must be stated that the shear layer mode and the jet column mode may not be perfectly decoupled. In fact, both hydrodynamics and acoustic feedback effects can be present (see e.g. Hussain 1986). The time signal and eddy formation at the jet exit and in the intermediate region may be triggered by the feedback from the structures which evolve downstream. This feedback may also play an interesting role in sustaining self-excited excitation.

4.1.2. *The developed region*

In the intermediate region of the axisymmetric jet the large-scale coherent structures interact with each other. Merging, tearing or secondary instability phenomena are present. In this region, the structures are responsible for the bulk of the engulfment of ambient fluid with the consequent increasing of the entrainment activity (Komori & Ueda 1985; Liepmann & Gharib 1992). The helical instability has a growing importance as the flow approaches the end of the potential core and becomes dominant in the fully developed region. Increasing the axial distance, the helical structures, with right handed and left handed modes of equal probability, move radially outwards (Komori & Ueda 1985) giving, together with local ejection of turbulent fluid and bulk entrainment of ambient fluid, a great contribution to the jet spreading. At large distances from the jet exit (more than 20 diameters) the jet shows self similar profiles. Experimentally it has been found that the width increases linearly with the streamwise coordinate and, since the product $U_{CL}(x)R(x)$ has to be constant to conserve the axial momentum, the centreline velocity decays as x^{-1}. In this region the external periodic excitation useful to describe the large-scale structure behaviour in the near exit region is of little use. Moreover, flow visualization cannot help in studying this region since the marker is highly dispersed due to the small-scale diffusivity. However, some researchers still try to study the coherent structures even far away from the jet exit. In this case only a sort of statistical coherent structure is depicted and characterized.

4.2. The axisymmetric swirling jet

The near field of a non-swirling jet is mainly driven by instabilities or turbulent mixing and the pressure plays a minor role. However, when a tangential velocity component is superimposed on the axial one in a circular jet, both radial and axial pressure gradients are generated. These gradients may significantly influence the flow changing the geometry, the evolution and the interactions between the vortical structures.

For swirling jets different flow regimes may be identified depending on the degree of swirl present in the jet. For low swirl numbers (i.e. when the maximum tangential velocity is of the order of 50% or less of the axial centreline velocity) the jet behaves in a similar way as for the non-swirling case, even though some modification in the mean and fluctuating velocity distributions, jet width or spreading are present. Some changes in the dynamics of the large vortical structures are also present. However, when the swirl becomes strong (i.e. when the tangential velocity becomes larger than the axial velocity), the adverse axial pressure may be sufficiently large to establish a reversed flow on the jet axis and a complete different scenario is present. This is usually called the vortex breakdown regime. In between these two regimes an intermediate regime is established. The behaviour of the jet in this case is the results of complicated interactions between modes, which are typical of axisymmetric jets and rotating flows.

4.2.1. *Definition of the swirl number*

In general, the Reynolds number for an axisymmetric jet is based on the diameter of the nozzle and on the axial velocity at the centreline or the bulk velocity. On the other hand the definition of the swirl number varies between different studies. A common way is to express the swirl number as the ratio between the fluxes of the tangential and axial momentum ($S_{\theta x}$, see eq. 2.24). However, such a measure means that the velocity profiles of both the streamwise and azimuthal velocities need to be measured accurately to allow the integration across the jet orifice. This is in some cases not possible nor practical and other measures have been suggested by various researchers.

Chigier & Chervinsky (1967) proposed that $S_{\theta x}$ could be determined as the ratio between the azimuthal velocity maximum and the axial velocity maximum at the orifice, whereas Billant *et al.* (1998) used a swirl number based on the ratio between the azimuthal velocity measured at half the radius of the nozzle and the centreline axial velocity at about one diameter downstream the jet outlet. It has also been shown (Farokhi *et al.* 1988) that for some cases the measure $S_{\theta x}$ is inappropriate to characterize the vortex breakdown since two jets with different velocity profiles can still have the same swirl number but different development of the flow field. In the present work, however, there exist natural outer parameters that can be used to determine a swirl number, namely as the ratio between the azimuthal velocity at the pipe wall (maximum azimuthal velocity) and the mean bulk axial velocity (see eq. 2.16).

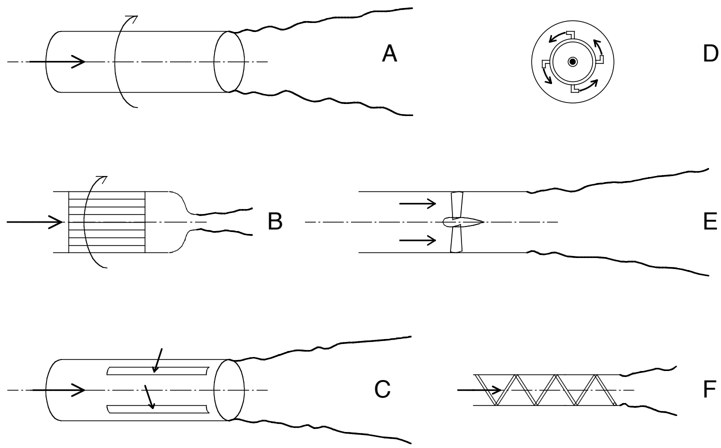

FIGURE 4.2. Schematic of six different methods to genearte a swirling jet. A) Rotating pipe, B) Rotating honeycomb, C) Tangential slots, D) Tangential nozzles, E) Deflecting vanes, F) Coil insert.

4.2.2. *Swirl generation techniques*

There are many reported experiments on swirling jets, however the methods to generate the swirl differ, which also means that the outlet velocity distribution will vary between different experiments. In the following we will describe some of these methods which also are sketched in figure 4.2.

4.2.2.1. *Rotating methods*

In the present work we use a long, axially rotating pipe to estabish the swirling flow, which is the same principle as that used by Rose (1962) and Pratte & Keffer (1972). Rose (1962) used a pipe with an L/D =100 and assumed that the flow was in solid body rotation at the outlet, whereas Pratte & Keffer (1972) used a somewhat shorter pipe in their experiment. In that case they used a flow divider at the inlet which brought an azimuthal component to the flow. From the foregoing section we are now aware that only a laminar pipe flow will have a solid body rotation, whereas a turbulent rotating pipe flow will not, even if the pipe was infinitely long. However, if the pipe is sufficiently long, this is probably the method for which the resulting flow is most independent on the individual set-up.

Komori & Ueda (1985) adopted a similar technique adding a convergent nozzle to the rotating pipe. However in this case the azimuthal and axial velocity components will be affected differently by the contraction. From an inviscid analysis one obtains that the axial velocity will increase in proportion to the contraction ratio (CR) whereas the azimuthal only as the square root of CR. In reality also the detailed geometry of the contraction will play a role and therefore different set-ups will give different outlet profiles.

Billant *et al.* (1998) and Loiseleux & Chomaz (2003) used a motor driven, rotating honeycomb before a contraction nozzle. In their case the Reynolds number is low and the honeycomb ensures a laminar flow with solid body rotation. However when the flow goes through the contraction it is distorted and the axial velocity becomes pointed at the centre and the flow does not seem to be in solid body rotation.

4.2.2.2. *Secondary flow injection*

A different technique is to inject fluid tangetially in the pipe section. Chigier & Chervinsky (1967) utilized tangential slots in a mixing chamber set before the nozzle where a tangential flow was supplied to the main axial flow. The regulation of the flow field was made by varying the relative quantities of axial and tangential air.

A similar principle was used by Farokhi *et al.* (1988) who instead introduced the flow inside the pipe through concentric manifold rings and elbow nozzles upstream a bell-mouth section driving the air to the nozzle exit. Also here the swirl rate can be set by controlling the proportion of axial to tangential air.

4.2.2.3. *Passive methods*

A passive method to introduce swirl is through a swirl generator with annular vanes that deflect the flow before the nozzle exit (see e.g. Sislian & Cusworth 1986; Panda & McLaughlin 1994; Lilley 1999). In this case the ratio between the axial and the swirl components depends mainly on the tilting angle of the blades.

Another possibility is to use a coil insert mounted at the wall to impose the swirl component (see for instance Rahai & Wong 2001). Also in this case the flow depends on the geometrical parameters of the coil.

4.2.3. *Swirling jet instability*

The spatial and temporal instability of a swirling jet has been investigated both experimentally and theoretically. Several analytical investigations have been performed in order to find the linear stability of different combination of axial velocity profiles and a rotational motion. In this type of flow the Kelvin–Helmoltz and the centrifugal instabilities may be present simultaneously since, in addition to the velocity gradient, the shear layer experiences a radial pressure gradient due to the azimuthal component of velocity.

Similarly to the Kelvin-Helmoltz (inviscid) instability criterion due the shear layer, a criterion for the centrifugal instability can be introduced. The following relation (Rayleigh 1916; Synge 1933) gives necessary and sufficient condition for the onset of the axisymmetric mode:

$$\frac{d}{dr}(rV)^2 < 0 \tag{4.1}$$

This means that the circulation must decrease with increasing radial distance. Other criteria taking into account an axial flow both for axisymmetric and helical modes have also been proposed (see e.g. Leibovich & Stewartson 1983; Loiseleux & Chomaz 2003).

Lessen *et al.* (1974) studied the temporal instability of a Batchelor vortex (see section 2.1.3) for different values of a swirl parameter related to the relative intensity of the axial and azimuthal velocities. Viscosity was also added in a following study (Lessen & Paillet 1974; Khorrami 1995; Mayer & Powell 1992). However this model was not adequate to describe the instability of a swirling jet since the axisymmetric mode was found to be always stable.

A more realistic flow model was studied by Martin & Meiburg (1994), for which there is a jump both in the azimuthal and streamwsie velocity at the jet periphery. They concluded that a centrifugally stable jet may be destabilzed by Kelvin-Helmholtz waves which in their model originate from the jump in the azimuthal velocity. In another study Loiseleux *et al.* (1998) investigated the stability of a Rankine vortex (see section 2.1.3) with an added plug flow. In contrast to the Batchelor vortex this type of flow is unstable to axisymmetric disturbances. Moreover, the swirl breaks the symmetry between negative and positive helical modes, which is a typical characteristic of a non-swirling jet. In their work they also studied the absolute/convective nature of the instability.

Absolute instability in swirling flows has been analyzed by Lim & Redekopp (1998) and Michalke (1999). They showed that the tendency towards absolute instability is increased when the shear layer is centrifugally unstable.

An experimental study of the Kelvin-Helmoltz instability in a swirling jet was performed by Panda & McLaughlin (1994). Their analysis is concentrated to high swirl numbers (close to the breakdown) and they conclude that swirl tends to reduce the amplification of the unstable modes.

Loiseleux & Chomaz (2003) made a well-detailed experimental analysis on the instability of swirling jet and found three different flow regimes for swirl numbers below that for which vortex breakdown occurs. They used the same experimental set-up as that of Billant *et al.* (1998). For small swirl numbers the rotation does not affect the jet column mode and that case behaves similarly to the non-swirling case. As the swirl number increases the amplitude of this mode decreases and instead a helical mode grows. Moreover, a different secondary instability mechanism is set. Co-rotating streamwise vortices are formed in the braids, which connects the rings. In the intermediate swirl range these two instability mechanisms compete against each other. This scenario becomes more and more complicated when the swirl number is increased. Just before the breakdown strong interactions between azimuthal waves and ring vortices are observed.

Numerical studies concerning the analysis of non-linear axisymmetric and three-dimensional vorticity dynamics in a swirling jet model have been performed by Martin & Meiburg (1998). They used a vortex filament technique to perform a numerical simulation of the non-linear evolution of the flow, whereas Hu *et al.* (2001) used DNS to study a temporally evolving swirling jet near the exit under axisymmetric and azimuthal disturbances.

4.2.4. *Studies of turbulent jets at moderate swirl numbers*

Most of the early analysis of swirling jets are based on experimental works, mainly focused on measuring mean profiles or turbulent transport properties, even though some theoretical works concerning laminar swirling jets are also reported in the literature. In one of these first investigations, Rose (1962) showed that even a weak swirl could radically change the character of the radial motion in the jet.

An early work by Chigier & Chervinsky (1967) shows that approximately at 10 diameters from the jet exit the influence of the rotation becomes small. An attempt to theoretically describe the flow based on the integration of the Reynolds equations is also shown. Good agreement is found giving the possibility to formulate semi-empirical equations, which, when calibrated with the experimental results, give the complete description of the mean velocity and pressure fields. However, the role of the initial conditions is not clear, viz. exit velocity profile, turbulence level, and status of the boundary layers before the jet exit.

In this period most of the experimental works (like for instance Pratte & Keffer 1972) were devoted to the study of specific configuration of swirled jets. Nevertheless, some general conclusions could be assessed. For instance it was shown that the entrainment and the spreading was increasing with respect to the non-swirling jet.

Park & Shin (1993) showed experimentally that for swirl number less than 0.6 the entrainment is independent of the Reynolds number increasing non-linearly with the downstream region. For S >0.6 the entrainment increases and becomes higher with Re probably due to a precessing vortex core phenomenon.

In order to find similarity in both the mean and the fluctuating components, Farokhi *et al.* (1988) showed that in the near field the mean velocity profiles strictly depend on the initial conditions. The sizes of the vortex core and the tangential velocity distribution seem to be the main controlling parameters. In a later study, Farokhi *et al.* (1992) considered the excitability of a swirling jet in the subsonic region. They found that periodic coherent vortices could be generated by plane-wave acoustic excitation. In contrast to non-swirling jets they found that vortex pairing is not an important mechanism for the spreading of a swirling jet.

In the presence of strong swirl, the decrease of the static pressure generated by the centrifugal forces may induce a reverse flow and the rapid entrainment in the region immediately after the jet exit (x/D <1). Strong differences appear also in the fluctuating components. Komori & Ueda (1985) showed that the turbulent kinetic energy attains a maximum in this region, due to the rapid mixing. Conversely, in a weak swirling or non-swirling jet the turbulent mixing is weak in the potential core region and the turbulent kinetic energy attains its maximum further downstream. Beyond the recirculating region the turbulence decays rapidly and becomes rather isotropic due to the strong mixing. More extensive measurements of highly swirling flows are made by Sislian & Cusworth (1986) and by Metha *et al.* (1991). They also show that the maximum turbulence is produced in the shear layer at the edge immediately after the exit.

More recently McIlwain & Pollard (2002) studied the interaction between coherent structures in a mildly swirling jet. Time-dependent evolution and the interaction of the structures are well documented.

4.2.5. *The vortex breakdown*

The vortex breakdown phenomenon has attracted considerable interest and Billant *et al.* (1998) give an up to date review of the literature on vortex breakdown in swirling jets. The vortex breakdown appears as an abrupt deceleration of the flow near the axis with the settling of a stagnation point generated by the axial increase of the pressure that is able to bring the axial velocity to zero. In experiments four different breakdown configurations have been observed: bubble, cone, asymmetric bubble and asymmetric cone. Here we will not go into any more detail since for the part of the the present work which deals with swirling jets ther swirl rate are below that for which vortex breakdown occurs.

CHAPTER 5

Experimental facility and setup

For the present work a new experimental facility has been designed and taken into operation at the Fluid Physics Laboratory of KTH Mechanics. The design philosophy has been to obtain a swirling jet flow with well defined characteristics which are independent of the specific geometry, i.e. the flow characteristics should not depend on the specific geomtry of swirl generators etc. To achieve this goal it was decided to use a long rotating pipe in order to obtain a fully developed turbulent pipe flow both with and without swirl, such that it would be independent of the inlet conditions. The Reynolds number of the study was decided to be of the order of $20 \cdot 10^3$ with possible variations of $\pm 50\%$. This means that the Reynolds number is high enough not to be influenced by transitional, intermittent structures. At the onset of the study, the swirl number of interest was decided to vary from zero (no rotation) up to 0.5 but it was later extended up to a swirl number of 1.5 for the pipe flow studies.

The length (L) of the pipe in terms of pipe diameters (L/D) is one of the crucial design parameters in order to obtain a fully developed flow. The relation between the Reynolds number (Re) and the swirl number (S) can be expressed as

$$S \cdot Re = \frac{\omega D^2}{2\nu}$$

Since we have decided to use air as the flow medium, and hence the value of ν is fixed, the desirable Reynolds and swirl number ranges then set certain limits on the pipe diameter and pipe angular velocity. Owing to lab space restrictions and the possibility to obtain pipes in one piece of good quality (in terms of roundness and surface quality) it was decided to use a pipe of six meter length with a diameter of 60 mm. This gives an L/D-ratio of 100 which was deemed sufficiently long to give a fully developed flow both with and without rotation. A rotational speed of about 13 revolutions per second is needed in order to obtain a swirl number of 0.5 at $Re = 20 \cdot 10^3$.

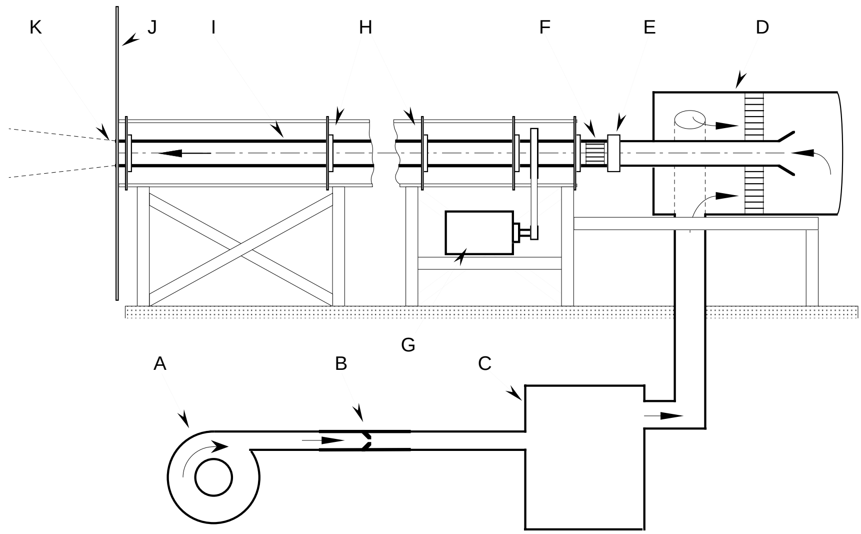

FIGURE 5.1. Schematic of the experimental setup. A) Fan, B) Flow meter, C) Settling chamber, D) Stagnation chamber, E) Coupling-box between rotating and stationary pipe, F) Honeycomb fixed to the pipe, G) DC-motor, H) Ball bearings, I) Rotating pipe with a length of 6 m and inner diameter of 60 mm, J) Aluminum plate, K) Pipe outlet.

5.1. Experimental apparatus

Figure 5.1 shows a schematic of the apparatus. The air comes from a centrifugal fan with a throttle at the inlet to allow flow adjustment, passes a flow orifice meter and is conveyed into a settling chamber to reduce fluctuations from the upstream flow system. From the settling chamber three pipes run radially into a cylindrical stagnation chamber distributing the air evenly. The flow passes an annular honeycomb to reduce lateral velocity components and, to further reduce remaining pressure fluctuations, one end of the cylindric settling chamber is covered with an elastic membrane. Finally, the air leaves the chamber through an axially aligned stationary pipe at the centre of the chamber. To achieve a symmetric smooth inflow the pipe is provided with an inlet funnel. The length of this pipe is 1 m and it is directly connected by a sealed coupling box to which on the other side the 6 m long rotaing pipe is connected.

The rotating pipe is made of seamless steel, has a wall thickness of 5 mm and an inner diameter of 60 mm. The inner surface is honed and the surface roughness is less than 5 micron, according to manufacturer specifications. The pipe is mounted inside a rigid triangular shaped framework with five ball bearings supports. The rotation is obtained via a belt driven by an electric DC motor with a feedback circuit. This ensures a constant rotation rate up to the maximum rotational speed of 1800 rpm. The drive is located close to the upstream end of the pipe. The structure has been statically and dynamically balanced and a test for vibrations has been performed for the rotation rates used during the experiments.

In order to bring the incoming air into rotation, a twelve centimeter long honeycomb is placed inside the rotating pipe immediately downstream of the inlet. The honeycomb consists of 5 mm diameter drinking straws. Of course it is also located inside the pipe in the cases when the rotation speed is zero.

For most of the studies the outlet of the pipe is at the centre of a stationary rectangular (80 cm $\times$ 100 cm) flat aluminium plate of 5 mm thickness. For the two component LDV measurement the flat plate has been replaced by a smaller annular plate of 30 cm in diameter in order to have optical access close to the pipe outlet. The pipe end is edged and mounted in such a way that it is flush with the plate surface. The rotating surface at the pipe outlet is limited to a ring of 0.5 mm in thickness.

The flow emerges horizontally into the ambient still air 1.1 m above the floor and far away from any other physical boundaries in the laboratory.

The test pipe was originally designed for moderate rotation rates, however when the experiments were underway it was also decided to go to higher swirl rates. A complication is that for high rotation rates the outcoming jet undergoes vortex breakdown and this also affects the flow near the exit of the pipe. In order to be able to perform measurements of the pipe flow itself also at higher rotation rates a glass section was added to the end of the steel pipe. For this case the large end plate was removed and the glass pipe was mounted to the steel pipe via an aluminum coupling. The glass section was 0.2 m long, with an inner diameter of 60.3 mm and a wall thickness of 2.2 mm. The glass pipe hence has a slightly larger diameter than the steel pipe which gives a step of approximately 0.15 mm at the connection. These measurements were however done only for a Reynolds number of 12000 which gives a step height of less than two viscous length units.

As mentioned above an orifice flow meter is used to adjust and monitor the pipe flow rate. The orifice is located after 1.0 m of a 1.65 m long, 40 mm diameter pipe and the orifice has a diameter of 28 mm. The pressure difference across the orifice is measured by a calibrated pressure transducer (MPX10DP). The flow meter curve as shown in figure 5.2 directly shows the transducer voltage as function of the bulk velocity in the pipe and shows the expected near parabolic shape. The bulk velocity has been calculated via integration of the mean velocity profile at the pipe exit using data obtained from single hot-wire probe measurements in the non-swirling flow. The accuracy of such a calculation is hampered by the weightining by the radius, which makes it quite sensitive to measurement errors close to the pipe wall. However, this is of no

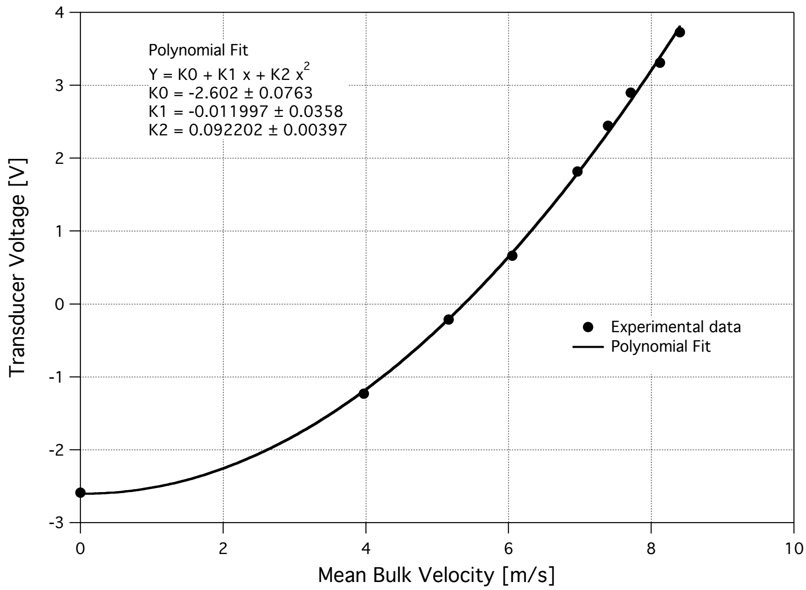

FIGURE 5.2. Pressure transducer calibration curve: the mean bulk velocity at the pipe exit is plotted versus the voltage from the pressure transducer. The pressure transducer has a linear response between pressure and voltage

major concern here since the main purpose of the flow meter is to monitor and ensure constant flow rates from day to day and to adjust the fan throttle to obtain a constant flow rate when varying the swirl rate.

A fully developed pipe flow in the non-rotating regime for the present Reynolds number range should be obtained for an L/D-ratio larger than typically 60. In the present study we investigated this in an indirect way by partially obstructing the honeycomb inserted at the inlet end of the rotating pipe with some plugs. No reminiscences of the plugs could be noticed in the flow which indicates that the flow has reached a fully developed turbulent state.

5.2. Measurement techniques

The velocity in the pipe and the jet was measured with Laser Doppler Velocimetry (LDV), hot-wire anemometry and stereoscopic Particle Image Velocimetry (PIV). In a first stage the LDV system was a one component system, whereas for the hot-wire anemometry both single and X-wires were used. The advantage with the hot wire is both that two components (the streamwise and either the azimuthal or the radial components, depending on the X-wire orientation) could be measured simultaneously as well as that continuous time signals are obtained. The main problems are the large velocity gradients near the pipe wall and the large flow angles (and even backflow) in the outer part of the

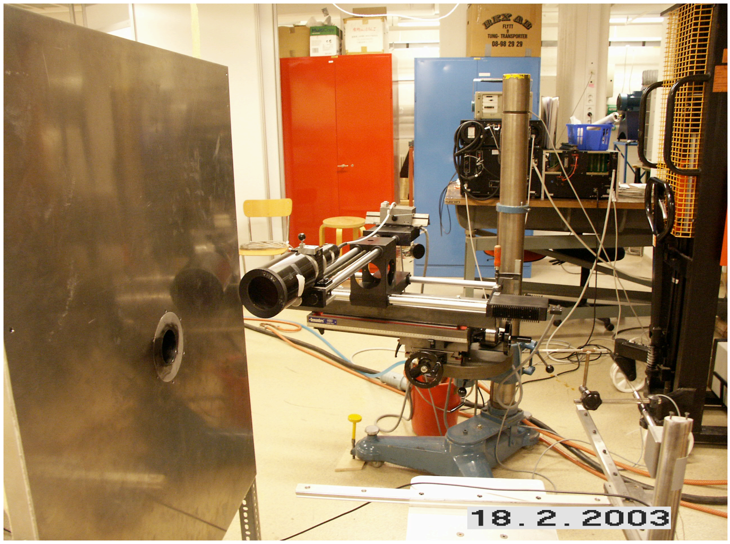

FIGURE 5.3. The LDV system in the inclined 12° configuration to measured at the jet exit.

jet which can reach values where the hot-wire calibration is invalid. The LDV measurements on the other hand can handle these situations, however the one-component system could not generate simultaneous signals of the two velocity components. A two-components LDV system has been used in a later set of experiments in order to provide simultaneous measurements of two velocity and their Reynolds stress. The measurements has been furthermore validated with the use of a stereoscopic PIV system able to catch, at the same time, all the three components of the velocity and to provide an instantaneous picture of the flow field.

In the following the present applications of the measurements techniques are described in details.

5.2.1. *Laser Doppler Velocimetry*

Laser Doppler Velocimetry (LDV) has been used to obtain mean and fluctuating velocity components in all three (streamwise, azimuthal and radial) directions. For the present experiment LDV has certain advantages as compared to hot-wire anemometry. For instance in the rotating flow the flow angles with respect to the streamwise direction can be fairly large which may make the use of hot wires unaccurate or even impossible and in the outer parts of the jet even backflow may occur. Rotating flows may also be sensitive to disturbances and therefore a nonintrusive measurement technique is preferable.

The LDV system is a single component FlowLite system from DANTEC comprising a single velocity component backscatter fibre optics probe with a beam expander, a 310 mm lens and a signal analyzer of correlation type. The source is a He-Ne laser of 10 mW emitting light with a wave length of 632.8 nm.

The system is equipped with a Bragg cell providing a 40 MHz frequency shift to be able to determine the flow direction. The LDV is calibrated by means of a rotating wheel with a well known angular velocity. The fibre probe head is mounted on a 2D traversing system driven by a DC-motor with encoder in each direction. The optics can be rotated 90° along its optical axis to measure the second velocity component. The measuring volume, an elipsoide, has the dimensions: $0.81\times0.09\times0.09$ mm^3 with its main axis along the optical axis. Most of the measurements were carried out with the optical axis perpendicular to the pipe axis. Therefore, axial and azimuthal velocities could be measured directly.

However, in the close vicinity of the pipe orifice, due to the presence of the large aluminum plate, the inclination angle was changed 12° in order to measure both velocity components at the outlet. The data at the pipe outlet do not cover the whole pipe diameter because, due to the inclination of the LDV system, scattered light saturated the photo detector when the laser beams approach the inner wall surface of the steel pipe. Figure 5.3 shows the set-up for LDV-measurements with the laser head on the traversing system. It also shows the pipe exit in the large rectangular end plate.

The data rate, which depends on the number of particles crossing the measurement volume, varied depending on the measurement position with the highest rate in the central region. The sampling was stopped either at 12000 samples or after 240 s. To acquire statistically independent samples the sampling rate was limited to 100 Hz (estimated as D/U_b).

The particles used for the LDV measurements are small droplets of condensed smoke of polyethylenglycol. They are injected into the air at the inlet of the centrifugal fan. No stratification of the particles in the outlet jet was observed, not even at the highest swirl rates.

In the second part of the experimental investigation a second LDV component, with the same geometrical characteristics as the above mentioned, has been added. The wave length used for the second laser beam was 514.5 nm. Both the LDV heads has been mounted on a 3D traversing system driven by DC-motor with encoder in each spatial direction. The geometrical axis of the LDV probes have been arranged in order to form a 90 degrees angle between them and to cross each other in the waste of the beams. The geometrical plane identified by the axis of the probes is set parallel to the flat plate standing at the outlet of the pipe. With such configuration it has been possible to measure simultaneously the radial and the azimuthal velocity component by traversing the jet along the radial direction. Data were only acquired when simultaneous signals were coming from both probes showing that the same particle is giving rise to both signals. Furthermore, in order to reduce the measurement volume and to assure a better quality of the signal, the photodetectors of the LDV probes have been switched so that the photodetector mounted on one probe was collecting the scattered light emitted by the other probe. For this set of measurement the sampling was stopped at 20000 samples or after 400 s. The

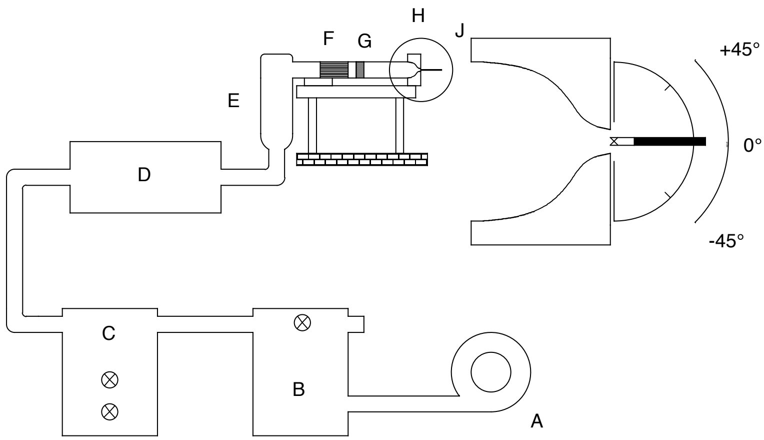

FIGURE 5.4. Schematic of the calibration jet setup. A) Fan, B) Settling chamber with seven valves, C) Settling chamber with two valves, D) Large stagnation chamber, E) Small stagnation chamber, F) Honeycomb, G) Sponge, H) Contraction, J) Holder for the X-wire to enable angular calibration.

acquisition of statistically independent samples was guaranteed by setting a dead-time of 10000 μs.

5.2.2. *Hot-Wire Anemometry*

Hot-wire measurements were mainly made with X-wire probes. These measurements complement the LDV measurements, in that it provide two velocity components simultaneously and time signals for spectral analysis. The X-wire probes are made in house. The wire diameter is 2.5 μm and it is 1.3 mm long and the distance between the wires is 1.5 mm giving a measurement volume of about 1.1 mm in side length. The probes are calibrated in the potential core of a small laminar top hat velocity profile air jet (the same device was used by Alfredsson & Johansson (1982), but with water) in a separate facility (figure 5.4) operating with air at the same temperature. Figure 5.5 shows a photograph of the calibration set-up with the hot-wire probe mounted on the device with which the angle of attack can be changed manually during the calibration.

The calibration procedure was similar to the one used by Österlund (1999) for which calibration points are obtained for a given set of velocities (typically 15 velocities) and probe inclinations (typical in intervals of 10 degrees, with larger angles at low velocities, up to ± 40 degrees). The calibration function is based on a 5th order polynomial approximation by least-squares fit of mean velocity and angle of attack of the probe (figure 5.6). For each point during the

FIGURE 5.5. Calibration jet device: the hot-wire is positioned in the potential core of the laminar jet. The angle of attack is regulated manually and the velocity of the jet air by a system of valves.

calibration the sampling rate has been fixed at 4000 Hz and the measurement performed for 30 seconds. The spectral analysis measurements in the swirling and non-swirling jet used a sampling rate of 10000 Hz and had a duration of 130 seconds. The velocity profile measurements used a sampling rate of 4000 Hz and a duration of 40 seconds close to the pipe exit (x/D$\leqslant$2) and a duration of 60 seconds further downstream.

The velocity data obtained by the hot-wire technique are similar to the LDV data (and also to the Pitot probe and the single-wire data used as test in the non swirling case). In the presence of a large velocity gradient across the X-probe (I.e. the two wires experience different mean velocities) the X-wire data need an "a posteriori" correction procedure similar to the one developed by Talamelli *et al.* (2000) and used to correct hot-wire measurements in the

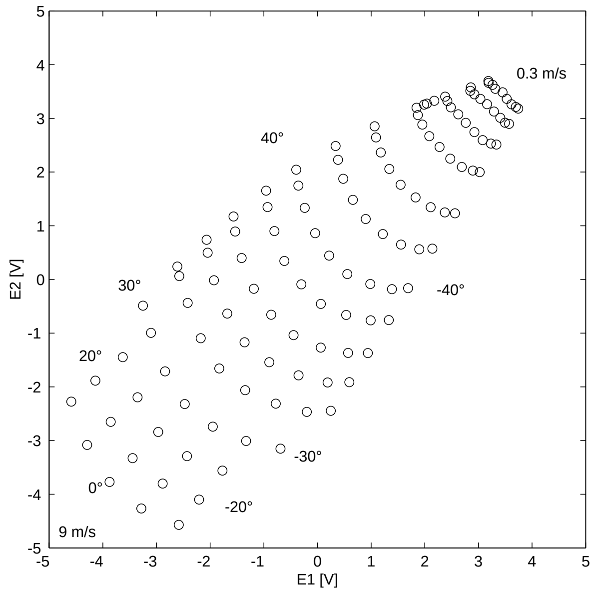

FIGURE 5.6. Example of calibration plot for the X-wire probe. The voltages from the two hot-wires identify the angle of attack of the probe and the velocity.

near wall region of a boundary layer. To measure simultaneously the axial and the azimuthal velocity components the X-wire probe is positioned with the two wires perpendicular to the traversed diameter. This configuration, due to the distance between the planes of the hot-wires, is particular sensitive to the strong velocity gradient of the investigated flow. The correction procedure make it possible to find out the mean velocity component from the measured ones ($\overline{U_m}$ and $\overline{V_m}$) in an iterative way according to equations 5.1 and 5.2. Δ represents the distance between the centres of the two wire but in this term it is possible to include all the geometrical uncertainties of the probe position.

$$\overline{U_m} = \overline{U} + \frac{\Delta}{2}\frac{\partial \overline{V}}{\partial r} + \frac{1}{2}\left(\frac{\Delta}{2}\right)^2 \frac{\partial^2 \overline{U}}{\partial r^2} + \cdots \tag{5.1}$$

$$\overline{V_m} = \overline{V} + \frac{\Delta}{2}\frac{\partial \overline{U}}{\partial r} + \frac{1}{2}\left(\frac{\Delta}{2}\right)^2 \frac{\partial^2 \overline{V}}{\partial r^2} + \cdots \tag{5.2}$$

Starting from a measurement with single hot-wire in a non swirling flow is possible to calculate $\partial\overline{U}/\partial r$ and, in the same flow $\overline{V_m}$ is measured with the X-wire. Then, since in such a flow there is no mean azimuthal velocity component ($\overline{V}$=0), neglecting in a first approximation the second order terms in 5.2, it is possible to estimate Δ that shows an almost constant value along the diameter of the pipe. Knowing Δ the correction is applied and the axial U and the azimuthal V velocity component are calculated including also the second order terms as shown in the equations.

5.2.3. *Stereoscopic Particle Image Velocimetry*

A stereoscopic PIV system has been adopted to investigate the 3D flow field. A commercial software from La Vision (Davis 7.0) has been used for the stereoscopic calibration, the pre-processing, the processing and the post-processing of the images. The setup consists of two high speed digital cameras Photron Fastcam APX RS, CMOS sensor, which can catch images up to 250 kHz with an internal memory module of 8 GB each, and a dual-head, high-repetition-rate, diode-pumped Nd:YLF laser Pegasus PIV by New Wave with a maximum frequency of 10 kHz featuring 10 mJ of 527 nm light output per cavity at 1kHz. During the experiments the images are captured at a frequency of 3 kHz with a resolution of 1024×1024 pixels at 10 bit using Nikon Nikkor 105 mm lenses. In this way the flow field is temporally and spatially resolved. A Scheimpflug system between lens and camera is needed to put on focus a plane not perpendicular to the lens axis.

The particles used for the PIV are the same used during the LDV measurements with the difference that, this time, the droplets of polyethylenglycol are generated by an atomisator and not by a smoke generator so that they are big enough to avoid peak locking problems in the images. Peak locking occurs when the measured particle displacement is biased to integer pixel values so that the velocity is underestimated or overestimated. Typically the particles on the display should be two pixels size and clearly distinguishable. Particular care has been dedicated to the choice of the thickness of the laser sheet in the area of interest and the delay time between the two images forming the pair taken from each camera: the movement of the particle has to be detected distinctly to prevent peak locking effects in the velocity components.

The 3D calibration procedure is done with the help of a calibration plate with a known geometry that has to be aligned with the laser sheet. In addition a self calibration procedure included in the software and based on dewarped images of the jet is used to correct the disarrangement between the calibration plate and the laser sheet itself. In the specific case 100 pair of dewarped PIV images have been taken in consideration. The stereoscopic PIV has been used in two configurations as shown in figure 5.7: one to visualise the flow in a cross section of the jet at 6 diameters downstream from the pipe outlet and a second one to inspect the axial section in a region approximately between 5 and 7 diameters downstream. In both the cases the cameras are positioned mirrored respect to the laser sheet and in order to see a forward-forward scattered light. The averaged data presented in this work are calculated over 3072 images distributed equally in time to cover 122.88 seconds.

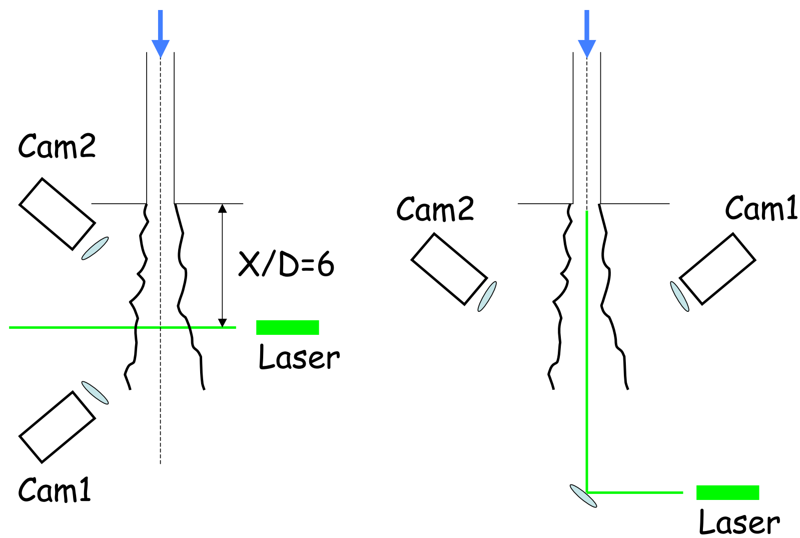

FIGURE 5.7. The configurations of the stereoscopic PIV.

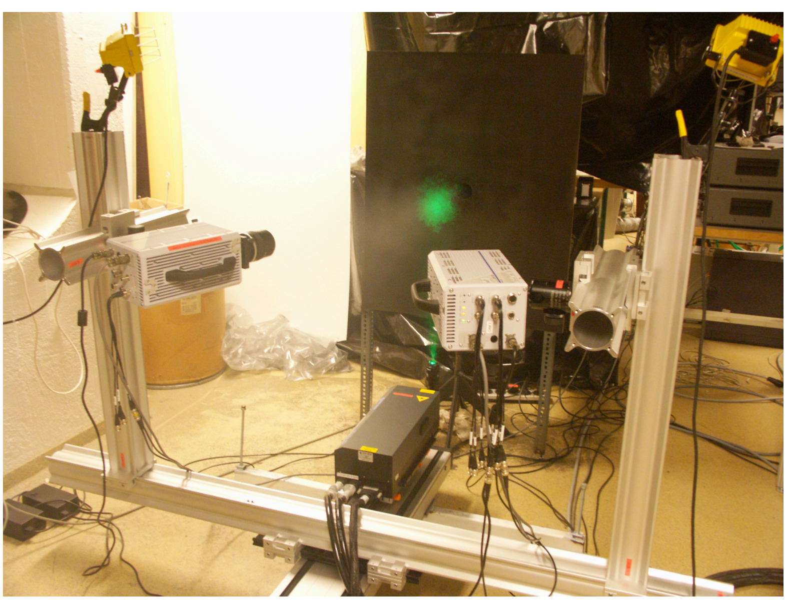

FIGURE 5.8. The stereoscopic PIV setup. Seen in the foreground are the two cameras and, on the floor, the pulsed laser is seen. The light spot in the centre of the dark plate is the smoke filled jet enlightened by the laser sheet.

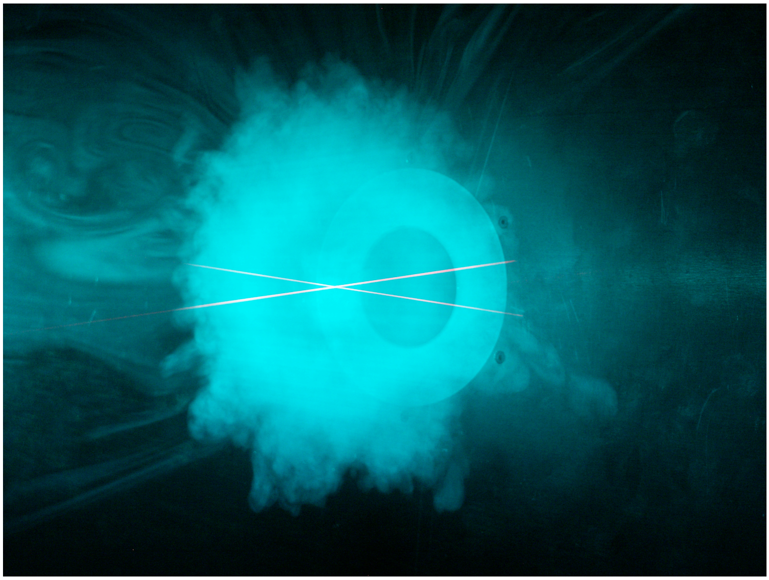

FIGURE 5.9. Flow visualization: the laser sheet cuts the swirling jet normally to the pipe axis at one diameter from the exit, seen as the dark hole in the centre. The two light beams are the LDV lasers that identify the centre of the jet one diameter downstream.

5.2.4. *Flow visualization*

A few flow visualization photographs were taken of the jet development. The smoke used for the visualization is the same as applied for LDV measurements (polyethylenglycol). The flow was illuminated with a laser sheet from a 2 W Argon-Ion laser source and the photographs were taken by a digital camera (Minolta DiMage 7i).

CHAPTER 6

Numerical method and procedure

A direct numerical simulation code developed and described by Verzicco & Orlandi (1996a) has been used both to supplement the rotating pipe flow data and to obtain comparative results for the swirling jet. Orlandi & Fatica (1997) has previously used the code to simulate rotating pipe flow at Re =5000 and various swirl numbers.

The code is written to solve the Navier-Stokes equations in a cylindrical coordinate system with the help of a staggered grid. The equations are discretized in order to apply a finite difference method and the time advancement is based on a fractional step scheme. it is written in such a form that the mass flow is conserved.

This chapter gives an overview of the numerical method used in the code.

6.1. Equations in cylindrical coordinate system

As already stated, the physics of the specific flow suggests the coordinate system to be adopted. The investigated pipe flow imposes the use of a cylindrical grid and, as a consequence, also the governing equations have to be expressed in this formulation. The problem in solving the differential partial equations ruling the velocity and pressure field in cylindrical coordinates is due to the singularity at the axis $r = 0$. The philosophy of the method developed by Verzicco & Orlandi (1996a) is to maintain a formulation as close as possible to the Cartesian coordinate system. The singularity is treated with the introduction of a staggered grid for the velocity components and the variable $q_r = rw$ (where w is the radial velocity component as already defined). Although not necessary Orlandi & Fatica (1997) made a similar transformation of the azimuthal component since it was found to give better accuracy.

The following new variables are hence used in the formulation of the equations

$$
\begin{aligned}
q_\theta &= rv \\
q_r &= rw \\
q_x &= u
\end{aligned}
\tag{6.1}
$$

In a cylindrical coordinate system with a reference frame rotating with the pipe wall, the governing equations using these variables become:

Continuity equation:

$$\frac{\partial q_r}{\partial r} + \frac{1}{r}\frac{\partial q_\theta}{\partial \theta} + r\frac{\partial q_x}{\partial x} = 0 \tag{6.2}$$

Navier-Stokes equations:

$$\frac{\partial q_\theta}{\partial t} + \frac{\partial}{\partial r}(\frac{q_\theta q_r}{r}) + \frac{1}{r^2}\frac{\partial q_\theta^2}{\partial \theta} + \frac{\partial q_\theta q_x}{\partial x} + \frac{q_\theta q_r}{r^2} + Sq_r =$$
$$-\frac{\partial p}{\partial \theta} + \frac{1}{Re}\Big[\frac{\partial}{\partial r}(r\frac{\partial}{\partial r}\frac{q_\theta}{r}) - \frac{q_\theta}{r^2} + \frac{1}{r^2}\frac{\partial^2 q_\theta}{\partial \theta^2} + \frac{\partial^2 q_\theta}{\partial x^2} + \frac{2}{r^2}\frac{\partial q_r}{\partial \theta}\Big] \tag{6.3}$$

$$\frac{\partial q_r}{\partial t} + \frac{\partial}{\partial r}\frac{{q_r}^2}{r} + \frac{\partial}{\partial \theta}\frac{q_\theta q_r}{r^2} + \frac{\partial q_r q_x}{\partial x} - \frac{{q_\theta}^2}{r^2} - Sq_\theta =$$
$$-r\frac{\partial p}{\partial r} + \frac{1}{Re}\Big[\frac{\partial}{\partial r}(r\frac{\partial}{\partial r}\frac{q_r}{r}) - \frac{q_r}{r^2} + \frac{1}{r^2}\frac{\partial^2 q_r}{\partial \theta^2} + \frac{\partial^2 q_r}{\partial x^2} - \frac{2}{r^2}\frac{\partial q_\theta}{\partial \theta}\Big] \tag{6.4}$$

$$\frac{\partial q_x}{\partial t} + \frac{1}{r}\frac{\partial q_r q_x}{\partial r} + \frac{1}{r^2}\frac{\partial q_\theta q_x}{\partial \theta} + \frac{\partial {q_x}^2}{\partial x} =$$
$$-\frac{\partial p}{\partial x} - \frac{\overline{\partial P}}{\partial x} + \frac{1}{Re}\Big[\frac{1}{r}\frac{\partial}{\partial r}(r\frac{\partial q_x}{\partial r}) + \frac{1}{r^2}\frac{\partial^2 q_x}{\partial \theta^2} + \frac{\partial^2 q_x}{\partial x^2}\Big] \tag{6.5}$$

The simulation is run at a constant mass flow, that means at a constant bulk velocity U_b.

6.2. Numerical method

6.2.1. *The grid*

An important part in the numerical solution of the partial differential eqs. (6.2) – (6.5) is the determination of a suitable grid. The geometry and physics of the specific problem usually suggests a suitable shape of the grid itself: through experimental or theoretical works it is known or estimated that certain regions of the investigated field suffer high gradients of the variables. Such regions usually have the biggest demands regarding the resolution. Therefore an uneven grid is usually preferred in such directions.

For the pipe flow simulations the mean flow is homogeneous in the streamwise and azimuthal direction therefore the spacing of the grid points in these directions are uniform. The homogeneity also suggest the use of periodic boundary conditions in these two directions. The length of the computational domain should be large enough to allow the growth of the structures present in the investigated application, i.e. correlations in the streamwise direction should go to zero within the domain itself. In the radial directions we know from the physics of the problem that large gradients are expected near the pipe wall and therefore a fine grid resolution near the wall is important.

A coordinate transformation permit to pass from a physical grid coordinate x_i to a computational grid coordinate ξ_i through the transfomation

$$x_i = f(\xi_i). \tag{6.6}$$

The first and second derivatives can hence be calculated as (no summation over the indices)

$$\frac{\partial q}{\partial x_i} = \frac{d\xi_i}{dx_i}\frac{\partial q}{\partial \xi_i} \tag{6.7}$$

$$\frac{\partial^2 q}{\partial x_i^2} = \frac{d}{d\xi_i}\left(\frac{d\xi_i}{dx_i}\frac{\partial q}{\partial \xi_i}\right)\frac{d\xi_i}{dx_i} \tag{6.8}$$

Particularly useful in the finite difference method is a coordinate transformation based on *tanh* that allows to stretch or to cluster the grid in the interested regions according to the physics of the flow. The computational grid ξ has the range $0 \leqslant \xi \leqslant 1$ while the physical grid x is related to the geometry of the problem. In the case of the investigated pipe flow the 3D grid is distributed in a cylindrical coordinate system. The physics of the flow field suggests to use a uniform grid in the axial and in the azimuthal directions $x_i = \Delta x_i \xi_i$ (where $\Delta x = L_{pipe}/N_{points}$ in the axial direction and $\Delta x = 2\pi/N_{points}$ in the azimuthal direction). In the radial direction instead the strong shear flow due to the presence of the pipe wall imposes a refinement of the radial grid in this region. The chosen coordinate transformation (6.9) allows to have a clustering of the grid points close to the wall and a stretching at the centre of the pipe.

$$r = \frac{\tanh 2\xi}{\tanh 2} \tag{6.9}$$

Figure 6.1 shows as the 50% of the computational grid points ξ are used to cover the last 20% of the physical coordinate r close to the wall. In the figure the physical coordinate has been normalised with the radius of the pipe so that $0 \leqslant r \leqslant 1$.

6.2.2. *Grid resolution*

Table 6.1 shows the grid resolution and pipe length used in the pipe flow simulations.

The simulations were done at the Department of Mechanics and Aeronautics at "La Sapienza" in Rome (2004) and typical computational times to reach a fully developed rotating pipe flow was 25 hours.

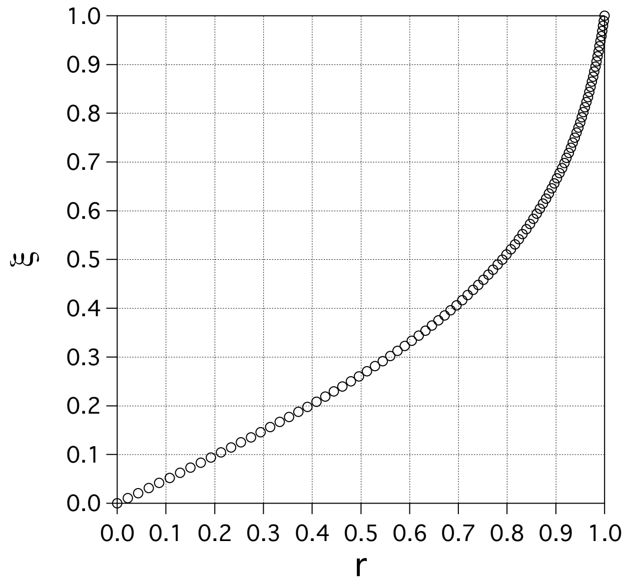

FIGURE 6.1. Coordinate transformation: computational grid versus physical grid. The centreline of the pipe is at r, ξ=0

Re	S	L/R	N_x	N_θ	N_r
5000	0 0.1 0.5	2.55π	96	96	96

TABLE 6.1. Grid resolutions used for the pipe flow simulations.

6.2.3. *Treatment of the pipe axis (r=0)*

In order to solve the problem of the singularity at the axis ($r = 0$) a staggered grid has been introduced. The three velocity components and the pressure are defined and evaluated at different positions of the computational cell. Only the radial component q_r is defined at the axis where it is known ($q_r|_{r=0} = 0$) while the azimuthal, the axial velocity and the pressure are defined respectively at the side face, at the lower face and at the centre of each cell. For a detailed description the reader is referred to Verzicco & Orlandi (1996a).

6.2.4. *Time-stepping*

The initial profile for the simulation is a parabolic profile, laminar flow, with a superimposed noise. The solution of the system of equations is performed with the fractional step method meaning that the advancement in time is divided into two sub-steps with the introduction of an intermediate velocity field $\widehat{u}$. Starting from the time $t = n$ where all is known the solution at the time $t = n + 1$ is derived passing through the intermediate step at the time $t = k$.

In our case a third-order low-storage Runge-Kutta/Crank-Nicolson scheme is used. With this scheme the stability limit given by the CFL-condition is CFL= $\frac{u\Delta t}{\Delta x} \leqslant \sqrt{3}$. Here u is the bulk velocity and Δx the streamwise coordinate spacing. All the presented simulations have been run at a constant CFL equal to 1.7.

For the pipe flow simulation the pressure drop is monitored and when it becomes constant in time the flow is considered fully developed.

6.3. The jet simulation

The same code used to study the rotating pipe flow has been modified to investigate the temporal evolution of a swirling jet. The initial conditions are obtained from a fully developed pipe flow simulation with the desired swirl number. The jet development is simulated by enlarging (in the radial direction) the computational domain, extending it out to $r = 4$. The initial conditions are set by the pipe velocity field in the region $0 \leqslant r \leqslant 1$ and by imposing zero to all the velocity components in the rest of the computational region. Furthermore the free-slip condition has been chosen at $r = 4$. It is worthy to note that the code preserves the two periodic directions, the azimuthal and the axial one, and, due to this fact, is not able to predict a non-zero mean radial component of velocity. Moreover the code requires that the mass be conserved so the jet does not present any sort of entrainment. The jet is therefore able to expand only due to diffusion. However, for a free jet the mass flow increases in order to conserve the streamwise as well as the angular momentum (which are the quantities that are conserved: see eqs. (2.22) and (2.23) In the simulation instead, the axial momentum and the angular momentum are not conserved but they decrease as the jet moves downstream. The results must be then read with this limitations in mind. The simulation is able to give qualitative results but not qualitative ones.

It should be mentioned that for the jet simulations the mean flow is changing with time so only spatial averaging for each time step can be done, i.e. averages can be made in the azimuthal direction along constant radii and in the streamwise direction. This means that averages are less accurate for this case than for the pipe flow where averages both in space and time could be taken. A possible solution for the jet flow would be to do several simulations with different initial fields and thereafter making ensemble averages. However only one simulation for each case where performed here.

The grid for the jet has been clustered in the neighborhood of the pipe radius $r \approx 1$ since in this part the flow present high velocity gradients in the axial and azimuthal direction while it has been stretched elsewhere. The

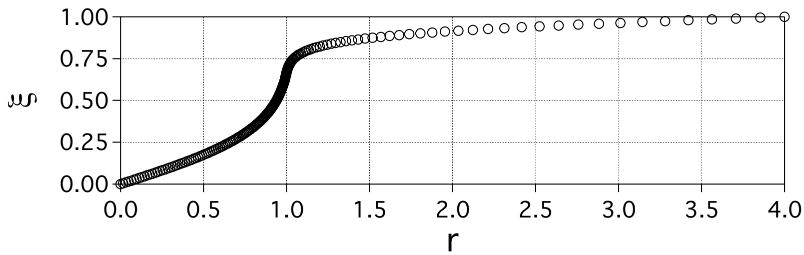

FIGURE 6.2. Coordinate transformation: physical grid versus computational grid.

coordinate transformation used for this purpose is described by the following expression:

$$x(\xi) = x_1(\xi)x_2(\xi) \tag{6.10}$$

where

$$x_1(\xi) = \frac{R_{med}}{R_{ext}}\frac{\tanh 3\xi}{\tanh 3\xi_R} \tag{6.11}$$

$$\tag{6.12}$$

$$x_2(\xi) = \frac{1}{x_1(1)} + \left(1 - \frac{1}{x_1(1)}\right)\frac{\tanh 9.5(\xi - 1)}{\tanh 9.5(\xi_R - 1)}. \tag{6.13}$$

R_{ext} is set equal to 4 and represents the radius of the computational domain, R_{med} indicates the region where to apply the clustering of the grid, in this case 1, while ξ_R represents the fraction of the computational points to be used in the inner region. In the simulation $\xi_R = \frac{2}{3}$ has been used that means $\frac{2}{3}$ of the computational points are used in the region $0 \leqslant r \leqslant 1$ and $\frac{1}{3}$ in the region $1 < r \leqslant 4$ as it is shown in figure 6.2.

Table 6.2 gives the resolution for the various jet flow simulations.

Re	S	L/R	N_x	N_θ	N_r
10000	0 0.2 0.5	2.55π	128	128	192

TABLE 6.2. Grid resolutions used for the jet flow simulations.

CHAPTER 7

Results for rotating pipe flow

In this chapter the results obtained for the axially rotating pipe flow are presented. The measurements in the rotating pipe complement and extend previous measurements of rotating pipe flow and the data are compared with other measurements and simulations. They are also used in the context of some recent scaling ideas. An important part of this investigation is to provide accurate exit conditions for the jet flow.

The experiments were carried out at three Reynolds number, Re= 12000, 24000, 33500 for the swirl numbers, S= 0, 0.2, 0.5, 1.0, 1.5 (the two highest S values were only measured for Re=12000). Measurements were taken both with hot-wire anemometry and LDV. For the two highest swirl numbers the measurements were made inside the glass extension of the pipe, whereas for all other measurements both the hot-wire and the LDV measurement volume were located at the pipe exit. However in the following mainly the LDV-data will be shown, although most measurements were also taken with the X-wire. In general one may say that the agreement between the two metods is good, however the hot-wire measurements was slightly affected by temperature drift and therefore not as accurate in absolute terms as the LDV data.

In the figures a radial traverse of the measurement position corresponds to a horizontal traverse in the laboratory frame of reference. Although the radius r by definition is always positive we consider negative the values of r on the left-hand side of the jet (looking from upstream).

In addition to the experimental results also DNS data are provided for Reynolds numbers Re= 5000 and 10000 at swirl numbers S=0, 0.1 and 0.5. Due to time limitations during the simulations only the case for Re=5000 has been carefully investigated.

7.1. The flow field

7.1.1. *Mean flow data*

We start by showing the mean streamwise velocity profiles for all three Reynolds numbers at S=0 and 0.5 in figure 7.1. All data have been normalized with the bulk velocity (U_b), which is taken from the flow meter measurements. No data could be obtained close to the wall at the right hand side (r/R >0.9) of the set up since reflections of the laser light in the pipe wall disturbed the measurements. As can be seen there is not a very large difference between

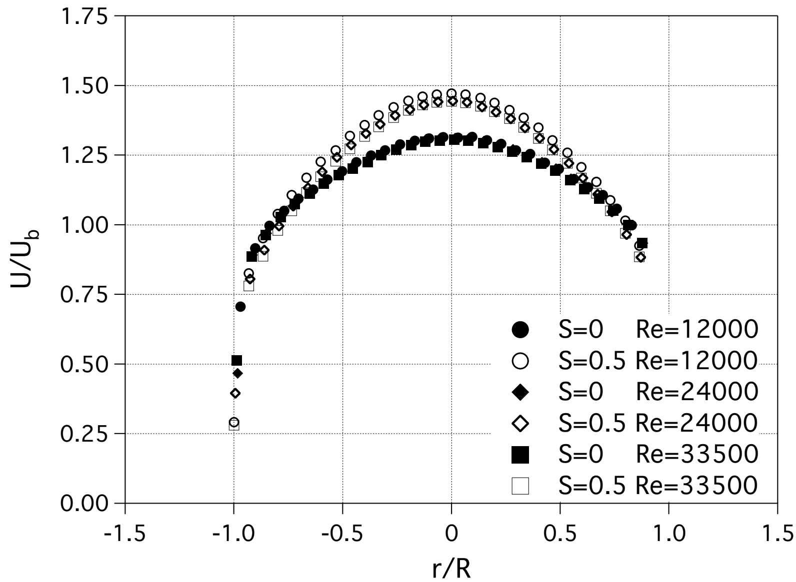

FIGURE 7.1. Streamwise mean velocity measured at the pipe outlet for three Reynolds numbers (Re =12000, 24000, 35000) and two swirl numbers S=0, 0.5.

the three Reynolds numbers, the non-rotating cases fall on top of each other and also the ones for S=0.5 are close, however they show a slight systematic variation. The most obvious result in the figure is however that the rotation cases show a more peaked velocity profile, i.e. the centreline velocity is higher, showing the tendency previously observed that the profile tends towards a parabolic shape. One would expect a slightly larger effect of the swirl for low Reynolds numbers, which is the trend observed here. The increase of the velocity at the centreline with rotation gives a corresponding decrease of the velocity close to the wall. This causes a decrease of the wall friction hence decreasing the overall pressure losses of the set-up. During the experiments the upstream valves were adjusted to keep the flow rate and hence Reynolds number constant when the swirl was increased.

Figure 7.2 demonstrates the good agreement between DNS and LDV data. Here only the negative side of the radius has been plotted due to the symmetry of the profile. The axial velocity is normalised with the bulk velocity. The Reynolds number used in the experiment is slightly higher compared to the simulation and, according to the experimental observations, a higher Re results, at a fixed swirl number, in a lower normalised velocity at the centreline and higher close to the pipe wall as shown in the picture. In figure 7.3 the same data set is normalised with the axial velocity at the centreline velocity showing the higher Reynolds number used in the experiments.

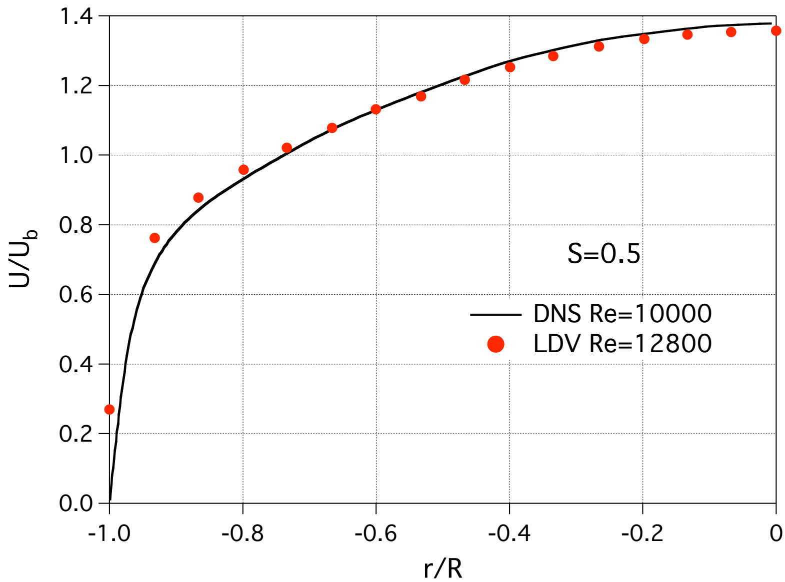

FIGURE 7.2. Streamwise mean velocity from DNS compared with LDV data.

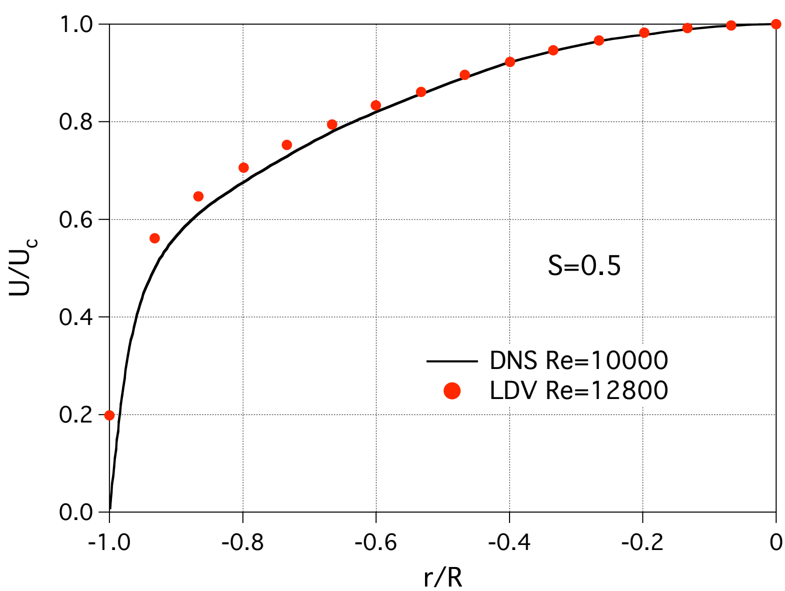

FIGURE 7.3. Streamwise mean velocity from DNS normalised with U_c compared with LDV data.

The same scenario displayed before in figure 7.2 for the LDV data is now shown in figure 7.4 for the simulations. The Reynolds number has been fixed at Re=5000 while the swirl number has been changed from S=0, no rotation, to S=0.1 and S=0.5. As previously established by the experiments, the increment of the swirl number produces more peaked axial velocity profiles. The effect of the low swirl number S=0.1 is very small on the axial velocity compared to the non rotating case but the change is consistent with that at higher S. In the same picture the LDV data for Re=12800 and S=0.5 are added for comparison with the corresponding swirl number in the DNS.

When running the simulation a first check is done on the pressure drop $\frac{\partial P}{\partial x}$ to make sure that it has reached a constant value before starting to use the data. In order to prove that the simulations have reached a statistically convergent solution not only for the mean values but also for the higher moments a check on the Reynolds stresses has been done.

Figure 7.5 displays the verification applied to the axial-radial Reynolds stress at S=0 and S=0.5 extracted directly from the u and w obtained from the DNS as well as calculated with eq. (2.14). The very good agreement implies the convergence of the DNS calculation even for the Reynolds stress and obviously also for the friction velocity u_τ. The case for S=0.1 is not presented in the plot for sake of readability reasons but of course the data collapse between the drawn ones. Furthermore, from the physical point of view, it has to be noted that the rotation causes a decrement of the axial-radial Reynolds stress in most of the pipe which is coupled to the increased velocity gradient (more peaked profile).

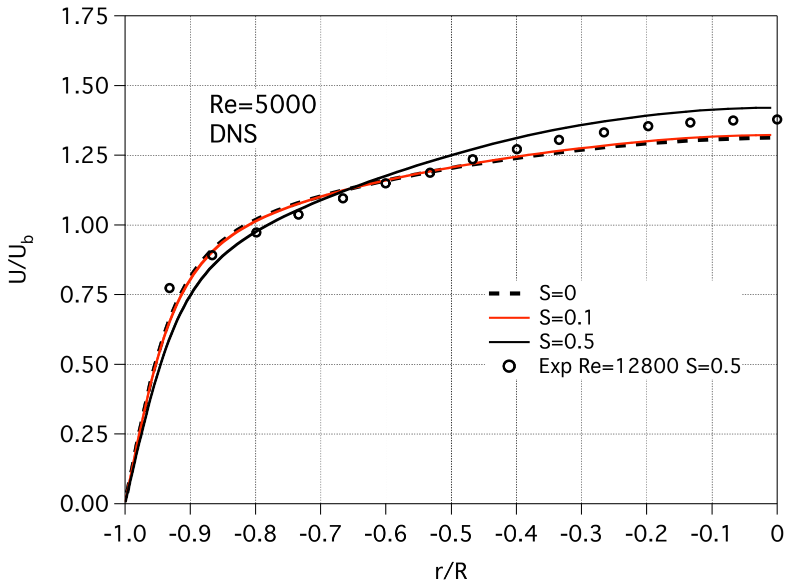

FIGURE 7.4. Streamwise mean velocity from DNS at different swirl number compared with LDV data.

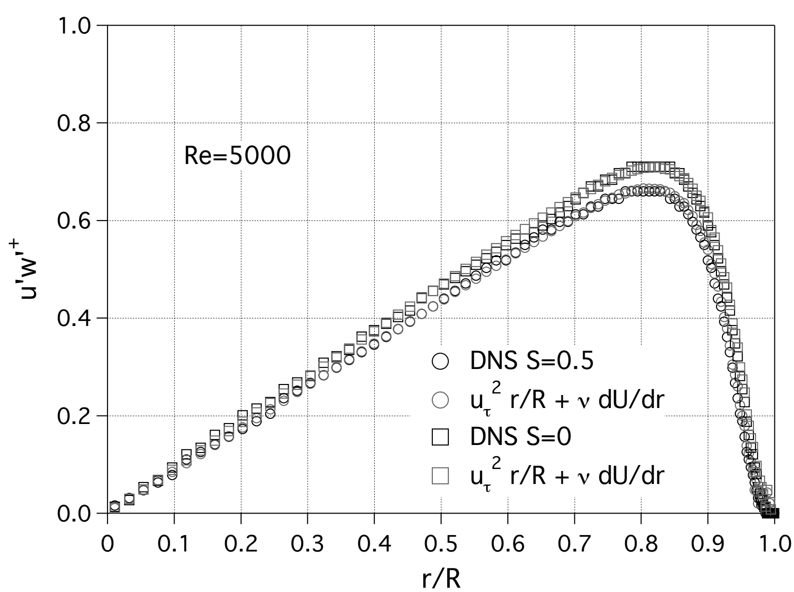

FIGURE 7.5. Axial radial Reynolds stress from DNS and calculated with the gradient of the mean axial profile.

The mean azimuthal velocity is shown in figure 7.6 across a full diameter of the pipe at S=0.5. As can be seen all three Reynolds numbers show a similar distribution and seem to follow the parabolic curve very close. The same trend is pictured by the DNS calculation in figure 7.7. Surprisingly the azimuthal velocity, in contrast to the axial velocity, exhibits the same profile independently of the swirl number and the Reynolds number adopted. Moreover the DNS is able to catch the behaviour of the azimuthal component close to the pipe wall where the experimental measurement techniques lack data. At a first sight, it may be surprising that the mean flow field of a rotating pipe flow deviates from solid body rotation, but as previously described, the difference as compared to the non-rotating case is that the Reynolds stress $\overline{vw} \neq 0$, which, as shown by eq. (2.12), make the azimuthal profile deviate from the linear one. We can use eq. (2.12) to determine the distribution of $\overline{vw}$ if the mean profile of V is known. In particular, by assuming a parabolic velocity distribution

$$\frac{V(r)}{V(R)} = \left(\frac{r}{R}\right)^2$$

it is possible to integrate eq. (2.12) analytically to obtain

$$\frac{\overline{vw}}{U_b^2} = \frac{2S}{Re}\frac{r}{R} \tag{7.1}$$

Equation (7.1) shows that the distribution of $\overline{vw}$ varies linearly with r if V is parabolic. However, this expression is of course not valid near the wall, since at the wall itself ($r = R$) both v and w have to be zero, and hence $\overline{vw}$ =0. The DNS calculation shows that, close to the pipe wall, the azimuthal velocity departs from the parabolic profile to approach the solid body rotation. That a parabolic profile in V would lead to a linear distribution of $\overline{vw}$ was first pointed out by Facciolo *et al.* (2003). Figure 7.8 shows, together with the linear relationship, the scaled azimuthal-radial Reynolds stress from the computation and from the experiments. As can be seen the overall agreement is good although the scatter in the experimental data is fairly high. This will be further discussed in chapter 9. Also the data of Speziale *et al.* (2000) shows a near linear relation between $\overline{vw}$ and r. The behaviour of the Reynolds stress explains the reason why, for a turbulent rotating pipe flow, the mean azimuthal velocity always lags behind the solid body rotation as pointed in eq. (2.17).

Again, to certify the quality of the DNS calculation, an indirect check on the Reynolds stress has been performed. The mean azimuthal velocity component has been calculate through eq. (2.17) with the use of the azimuthal-radial Reynolds stress obtained from the DNS. The resultant velocity has been plotted in figure 7.9 that shows a very good agreement between the direct and the calculated data confirming the statistics convergence of the simulation.

In the other part of this study swirling jets are investigated and for that case it is interesting to define a swirl number based on the velocity profiles according to eq. (2.24). From the measured velocity profiles at the pipe outlet

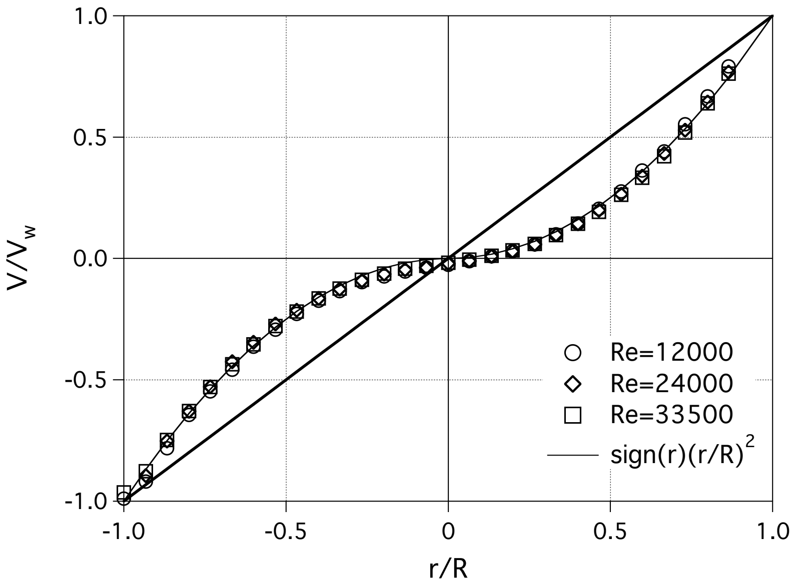

FIGURE 7.6. Mean azimuthal velocity. x/D=0, S=0.5 . The straight line represent the solid body rotation.

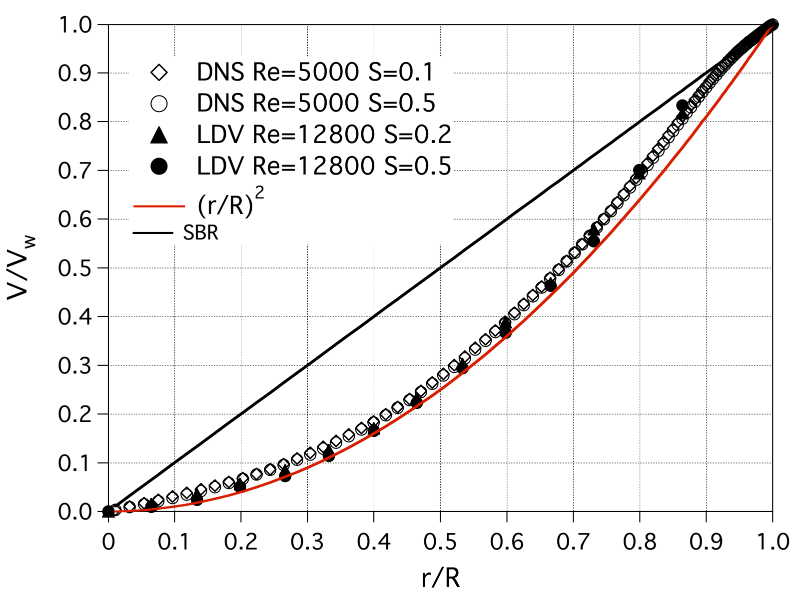

FIGURE 7.7. Mean azimuthal velocity from DNS and LDV .

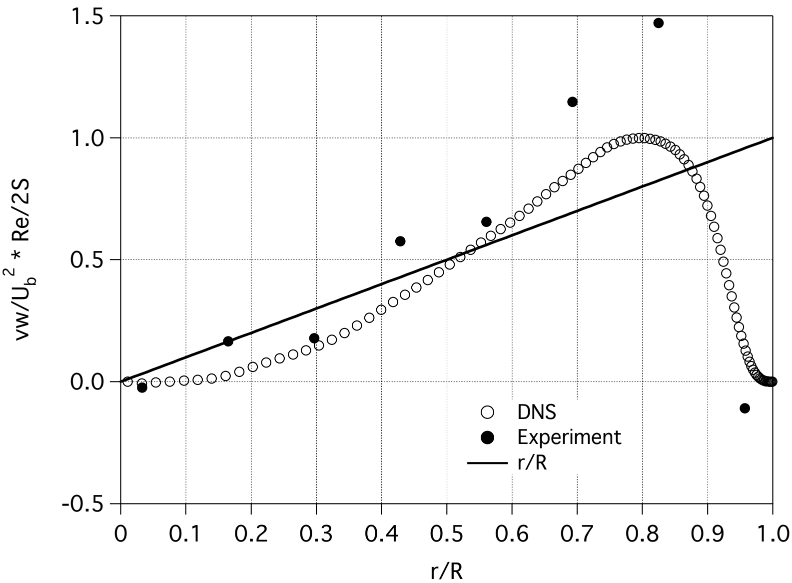

FIGURE 7.8. The theoretical distribution of $\overline{vw}$ (eq. 7.1) compared with DNS and experimental LDV data. The Reynolds number used in the simulation is Re=4900, in the experiment Re=24000.

it has been possible to make accurate calculations of this value which are shown in Table 7.1. The table indicates only small change in the values of the swirl number for all the Reynolds number investigated, which indeed is a measure on the similarity of the profiles. It can also be seen that the integrated swirl number has a numerical value of about one third compared to the swirl number S.

S	V_w/U_b	$G_\theta/(G_x R)$
Re=12000	0.2	0.064
	0.5	0.151
Re=24000	0.2	0.064
	0.5	0.152
Re=33500	0.2	0.064
	0.5	0.156

TABLE 7.1. The swirl number calculated at the pipe exit.

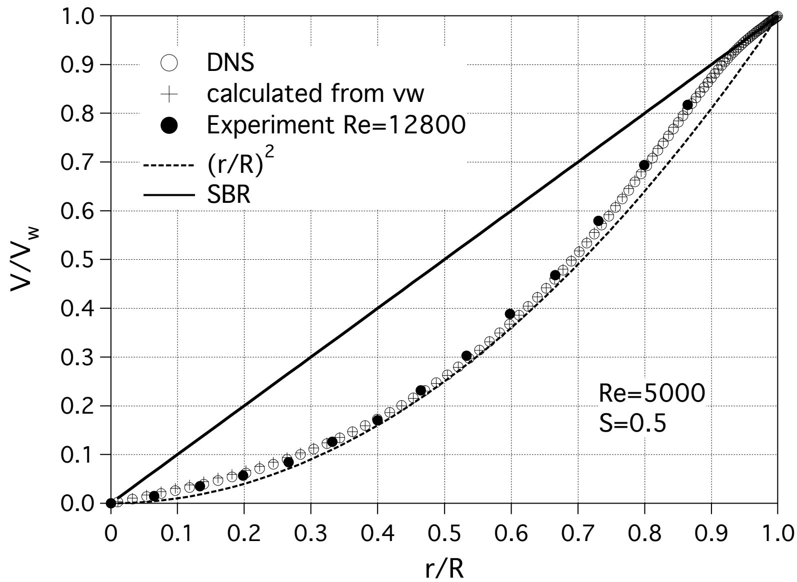

FIGURE 7.9. Mean azimuthal velocity from DNS and LDV compared with the azimuthal velocity calculated from the azimuthal-radial Reynolds stress.

7.1.2. *Turbulence distributions*

In this section we present some measurements of turbulence data taken mainly with the LDV equipment. First we present a comparison between u_{rms}-profiles (u'/U_b) in the non-rotating and rotating cases (S=0 and 0.5). The data show clearly that the rotating cases have lower values as compared to the non-rotating ones at the same Reynolds number, although the difference is not large. The difference is most evident at the centreline. With the present scaling the data are presented in "absolute" terms and if the data instead had been normalized with the centreline velocity the differences had become larger.

In figure 7.11 the v_{rms}–profiles (v'/U_b) are plotted. Unfortunately there are no available data for S=0, however the two swirl numbers seem to overlap nicely in the central part of the pipe whereas closer to the wall the level is lower for the high swirl number. The present trends both for u_{rms} and v_{rms} are in accordance with the measurements by Imao *et al.* (1996) who also observed a decrease with increasing rotation, however in the numerical simulations by Orlandi (1997) and Satake & Kunugi (2002) the trend is the opposite (as also shown by the DNS simulation in figure 7.12).

We also show a plot with the data of all three velocity components in order to demonstrate their relative magnitudes in the pipe in figure 7.13. For the present swirl rates this figure is qualitatively similar to what one would expect

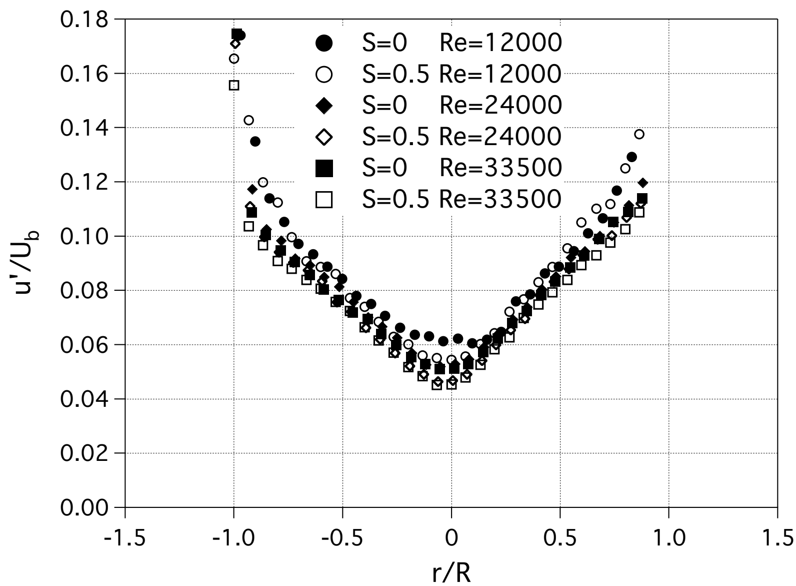

FIGURE 7.10. Streamwise turbulence intensity at x/D=0, S=0, 0.5 for the three Reynolds numbers in the legend. Same data as in figure 7.1

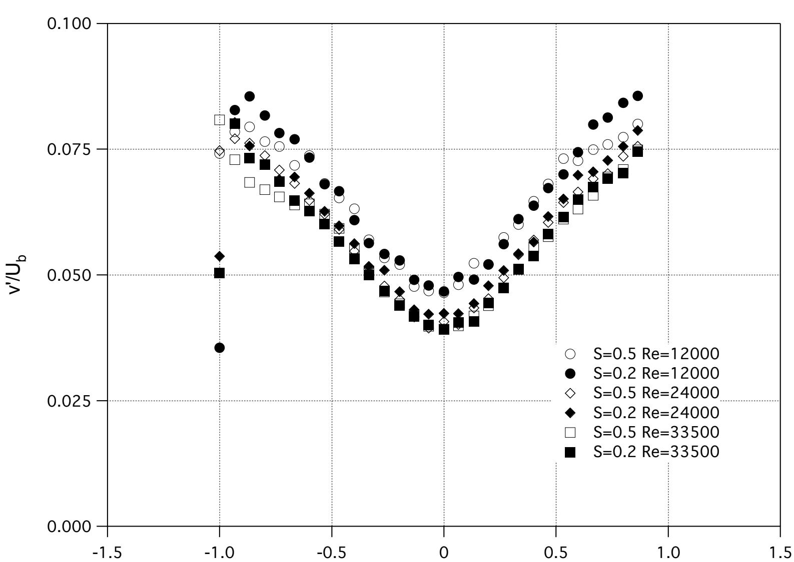

FIGURE 7.11. Azimuthal turbulence intensity at x/D=0, S=0.2, 0.5 for the three Reynolds numbers. The S=0.5 results are evaluated from the same data as in figure 7.6

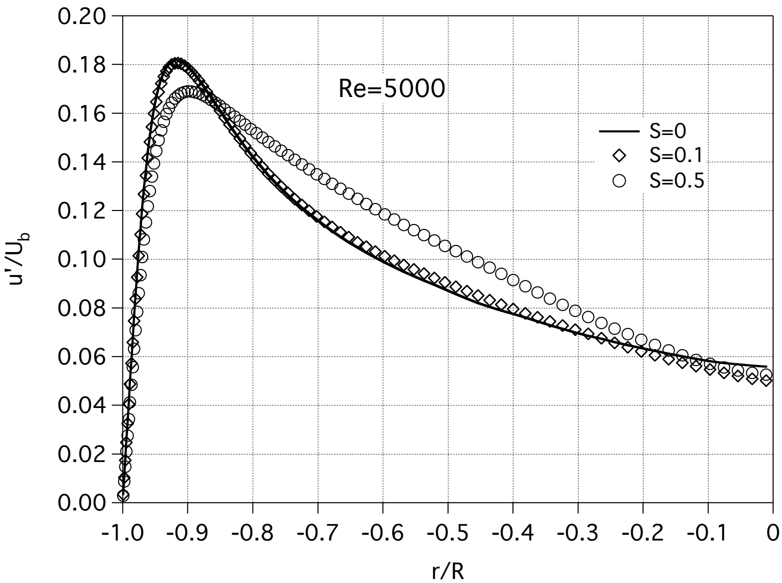

FIGURE 7.12. Streamwise turbulence intensity for S=0, 0.1, 0.5 from DNS.

for the non-rotating case. The streamwise turbulence intensity is the largest one, then there is the azimuthal while the radial is the smallest one. At the centreline the azimuthal and the radial turbulence intensity should have the same value which is also obtained in the measurements. It is not possible to do a direct comparison with the DNS (figure 7.14) because of the difference in the Reynolds number. The DNS turbulence intensity shows higher values and, since the simulation has been performed at a lower Reynolds number, the peak of the turbulence intensity for each velocity component is shifted slightly from the pipe wall as compared to the higher Re in the experiments. However, the trend of the three curves is similar to the experiments.

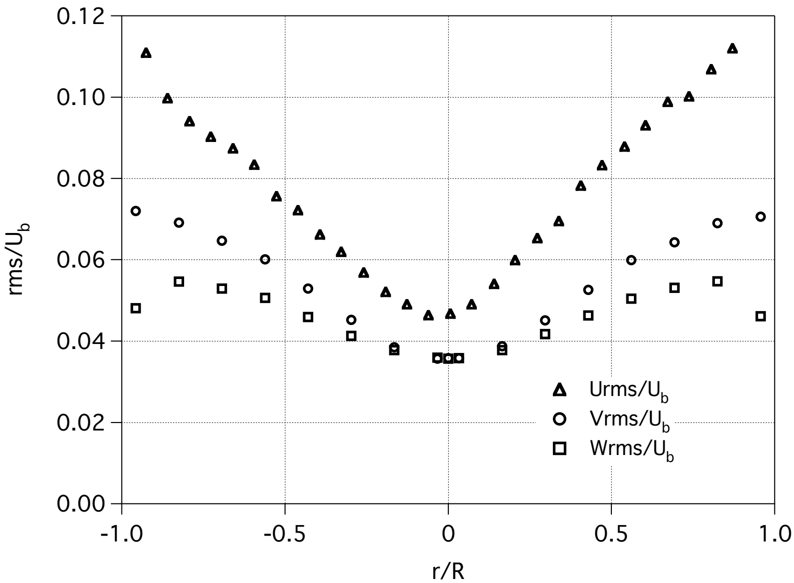

FIGURE 7.13. Comparison between the axial, azimuthal and radial turbulence intensity at the pipe outlet for S=0.5 Re=24000.

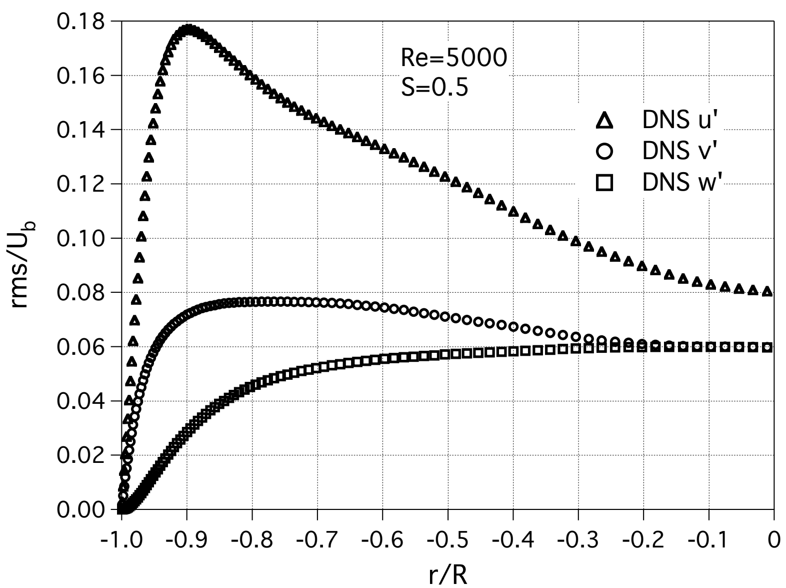

FIGURE 7.14. Comparison between the axial, azimuthal and radial turbulence intensity at the pipe outlet for S=0.5 Re=5000 from DNS.

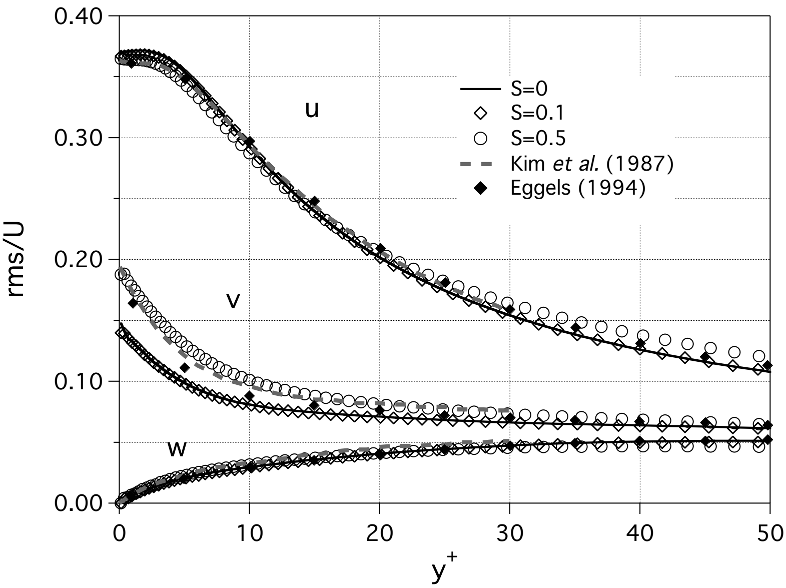

FIGURE 7.15. Turbulence intensity from DNS at Re=5000 and S=0, 0.1, 0.5.

Beside the bulk velocity, the local mean velocity (either the streamwise or the azimuthal) could be used to normalise the fluctuating parts of the velocity components. Such a scaling is summarised in the following figures. The axial fluctuating component, when normalised with the local axial velocity, tends to a common value, around, 0.37, at the pipe wall for all the three swirl number shown in figure 7.15. It is worth noting that the same value has been found by Kim *et al.* (1987) and by Moser *et al.* (1999) in their simulation of a turbulent channel flow at a similar Re and as also experimentally by Alfredsson *et al.* (1988). Furthermore also Eggels (1994) found the same result in the numerical simulation of a turbulent pipe flow. The three curves for different swirl number in the figure are actually very close to each other along all the pipe radius.

For our low S, i.e. 0 and 0.1, the azimuthal turbulence intensity is smaller than shown by the data from Kim *et al.* (1987) and Eggels (1994), however the simulation for S=0.5 show good agreement. The data from the radial component instead are in good agreement between all the simulations.

A completely different behaviour is shown by the azimuthal component in figure 7.16. The two swirl number considered (the case for S=0 does not allow the present normalisation) give two distinct curves that tend to two different values at the pipe wall as at the centreline. Anyhow, introducing the swirl number S in the normalisation it is possible to make the curve collapse for a large part of the radius. The difference between them still persists close to the pipe wall (figure 7.17).

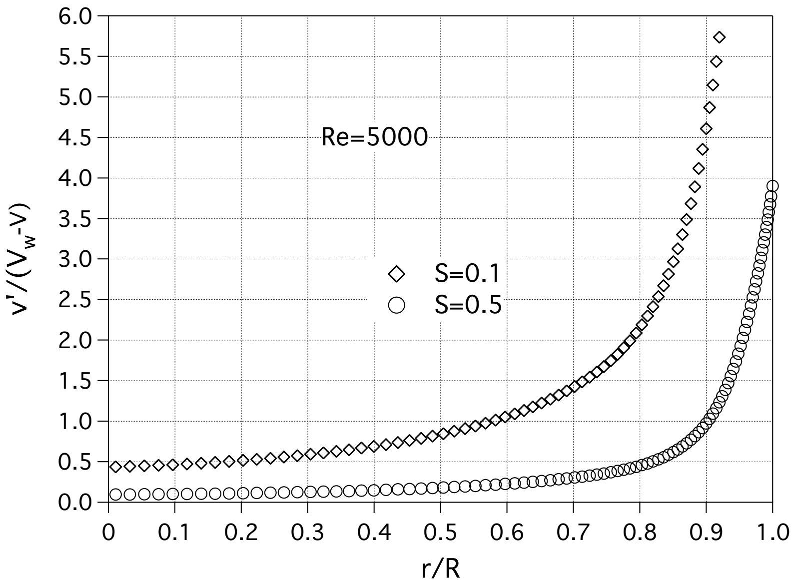

FIGURE 7.16. Azimuthal turbulence intensity from DNS at Re=5000 and S=0.1, 0.5.

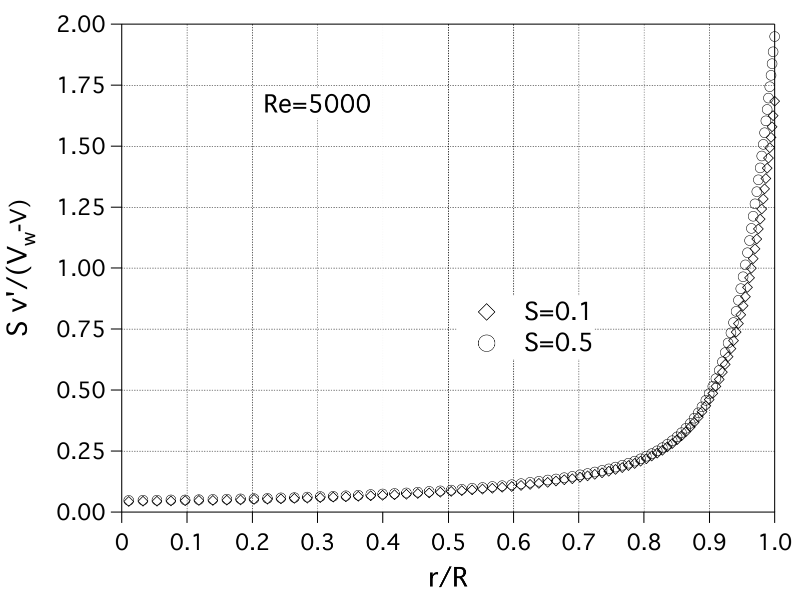

FIGURE 7.17. Azimuthal turbulence intensity from DNS at Re=5000 and scaled with the swirl number S=0.1, 0.5. Same data as in figure 7.16.

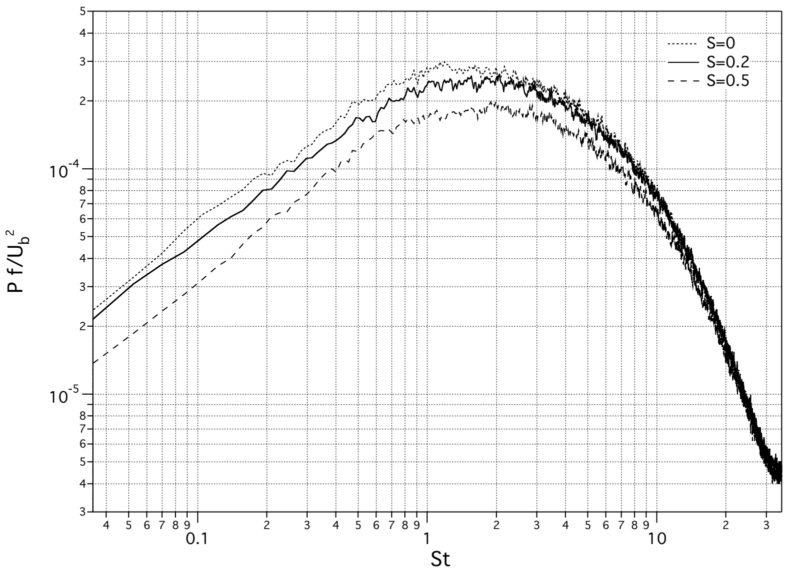

FIGURE 7.18. Spectra of u' at the outlet centreline measured with the X-probe. Re=33500.

Finally we show typical spectra of the streamwise velocity measured at the jet exit (figure 7.18) on the centreline. The spectra are plotted as the frequency times the spectral density $(f \cdot P)$ and thereby the region of maximum energy content is directly shown. They are also normalized by the bulk velocity so a comparison between them directly gives for which frequencies the turbulence has been affected. The frequency axis is normalized to show the Strouhal number ($St = fD/U_b$). As can be seen the energy density decreases with increasing rotation which is consistent with the data in figure 7.10. For the present data there is about a 10 % decrease in the values of u_{rms}/U_b when the swirl numbers increase from S =0 to 0.2 and a further decrease of 10 % when S =0.5.

7.2. Scaling of the mean flow field

In the following we will describe the streamwise mean velocity field in some different scalings. Typically a turbulent velocity profile is described in terms of the viscous sublayer, a buffer region, a logarithmic region and then finally a wake region. The logarithmic region is usually written as

$$\frac{U}{u_\tau} = \frac{1}{\kappa}\log\frac{yu_\tau}{\nu} + B \tag{7.2}$$

where u_τ is the friction velocity and $y = R - r$. The present measurements do not allow us to determine the friction velocity by extrapolating the mean velocity profiles to the wall and we will instead use the centreline velocity (U_c) as the velocity scale. In figure 7.19 the streamwise mean velocity data have been plotted in a semilogarithmic diagram. As can be seen in the figure the non-rotating case shows a typical logarithmic region up to $y/R \approx 0.3$. The full drawn line corresponds to

$$\frac{U}{U_c} = \frac{1}{K}\log\frac{y}{R} + C \tag{7.3}$$

with K=8.2 and C=0.97. The relation between the Karman constant κ and the constant K in eq. 7.3 is

$$K = \frac{U_c}{u_\tau}\kappa \tag{7.4}$$

and the additive constant

$$C = \frac{u_\tau}{U_c}\left(\frac{1}{\kappa}\log\frac{Ru_\tau}{\nu} + B\right) \tag{7.5}$$

If one wants to convert the data for the S=0 case to standard values one has to find the ratio of U_c/u_τ from friction factor data. At Re=12000 a good approximation of this ratio is 20.5 which would give us corresponding values of κ= 0.40 and B=4.0. Also the mean velocity distributions for low swirl numbers (S=0.2 and 0.5) seem to exhibit a logarithmic region albeit with a different slope as compared to the non-rotating case. It is also clear that the extent of the logarithmic region becomes smaller when S increases. For the high rotation rates (S=1.0 and 1.5) only two points on each set of measurements lie on a line with that slope so it is not possible to draw any conclusions.

Table 7.2 also include data points taken from the simulation of Satake & Kunugi (2002) (S&K in the table). The data are derived from their figure 3 with a logarithmic line fitted by eye. However these data seem to consistently show a lower value of K. This may be a Reynolds number effect since their Re was only 5300.

The DNS simulation allows an accurate determination of the slope of the curve in the logarithmic region. To present a comparison with the LDV data the same scaling has been used in figure 7.20 for Re=5000, S=0.5. The Reynolds number seems to rule on the values of K that, in this last case is equal to 4.5 corresponding to κ=0.205. An increasing Reynolds number produces and higher value for K as shown in table 7.2 where Re is increasing from the DNS to the LDV.

From the DNS calculation it is also possible to evaluate accurately the friction velocity u_τ and so to provide the scaling in plus units $u^+ = U/u_\tau$ and $y^+ = yu_\tau/\nu$. Following Österlund *et al.* (2000), to provide a correct value for the constants κ and B in equation 7.2 it is useful to consider the function Ξ plotted in figure 7.21

$$\Xi = \left(y^+ \frac{dU}{dy^+} \right)^{-1} \tag{7.6}$$

and, just replacing it in the logarithmic law, the value of B can be obtained from

$$\Psi = u^+ - \frac{1}{\kappa} \log y^+ \tag{7.7}$$

as shown in figure 7.22. Both the function Ξ and Ψ have to be constant in the logarithmic region which is, in the presented case, around $y^+ \approx 40$. From the chosen value of κ and B we draw the line in figure 7.23. Following the same procedure the plot in figure 7.24 has been produced. As can be noted, the three curves at different swirl numbers do not differ in the inner region where u^+=y^+ but they diverge just after as pointed out from the slope in the logarithmic region. The swirl number affects the value of u_τ (different values of u^+ at the centreline of the pipe) and, consequently the value of κ so that, for an increasing S, u_τ and κ decrease.

	DNS	*S&K*			LDV
S	κ	κ	u_c/u_τ	K	K
0	0.345	0.40	19.5	7.8	8.2
0.5	0.205	0.22	22.3	4.9	7.2
1.0	No Data	0.22	24.0	5.2	*(7.2)*
1.5	No Data	No Data			*(7.2)*
2.0	No Data	0.18	26.7	4.9	No Data

TABLE 7.2. Determination of the slope of the logarithmic region for the data in figure 7.19 as well as for the data of Satake & Kunugi (2002) and DNS simulation.

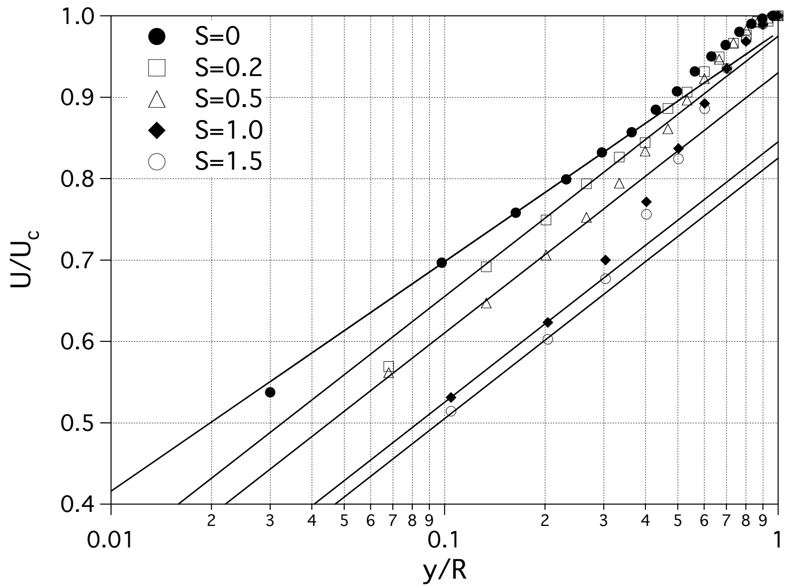

FIGURE 7.19. Streamwise mean velocity data at $Re = 12000$ for various values of S. The straight line for S =0 corresponds to K=8.2 whereas all other lines have K=7.2.

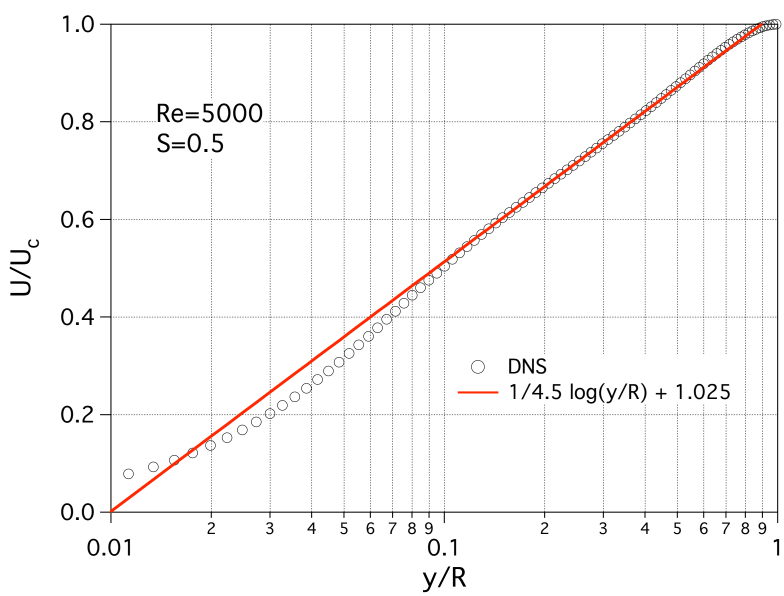

FIGURE 7.20. Streamwise mean velocity DNS data at Re=5000 for S=0.5.

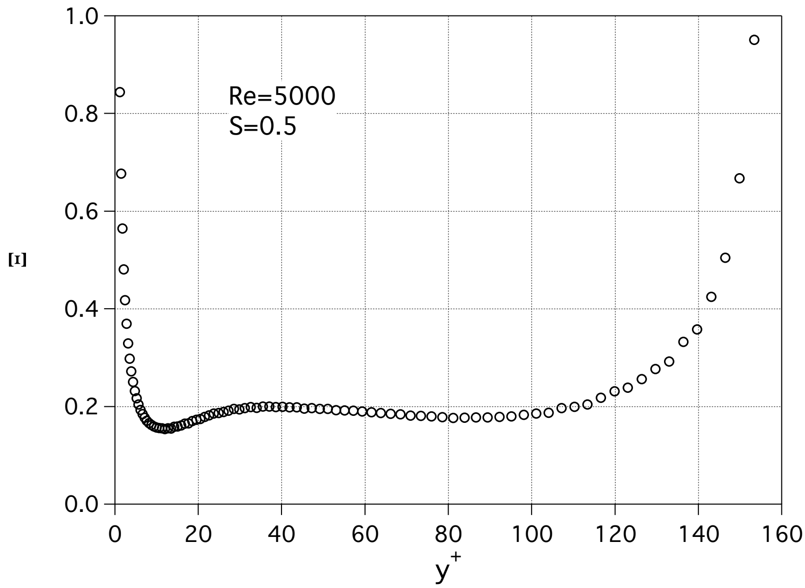

FIGURE 7.21. Plot to determine κ for DNS data at Re=5000 for S=0.5.

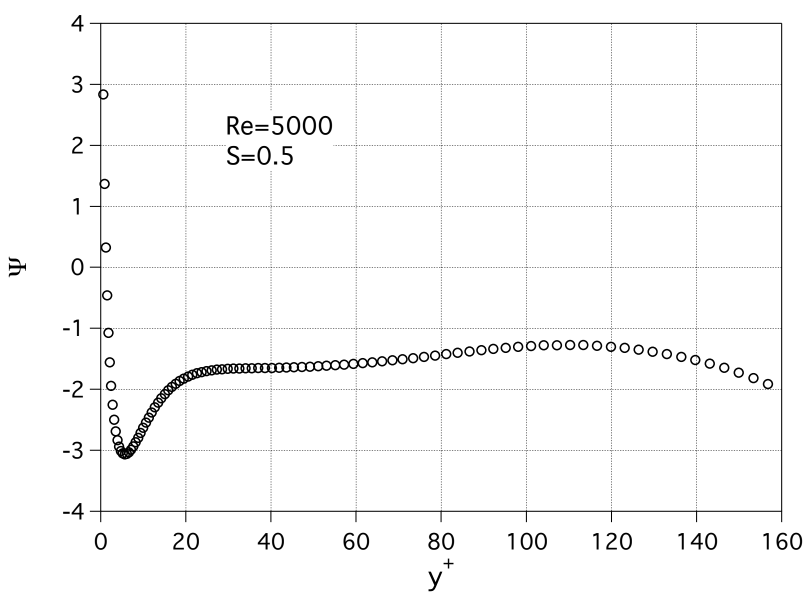

FIGURE 7.22. Plot to determine B for DNS data at Re=5000 for S=0.5. Same data as in figure 7.21

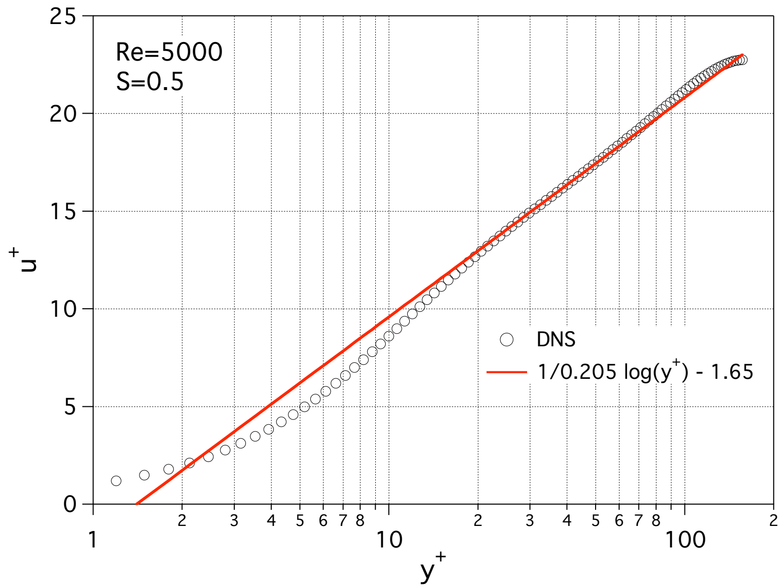

FIGURE 7.23. Streamwise mean velocity in plus units, DNS data at Re=5000 for S=0.5.

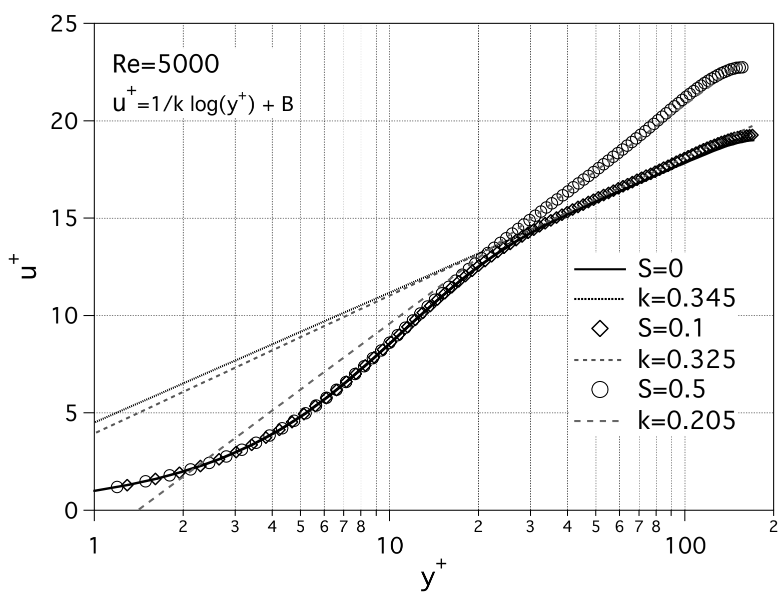

FIGURE 7.24. The streamwise velocity in plus units from DNS data at Re=5000 for S=0, 0.1, 0.5.

7.2.1. *Scalings by Oberlack (1999)*

In the analysis by Oberlack (1999) on stationary and rotating turbulent pipe flows, several scaling laws were suggested. In the following we will show some comparisons of our data at the lowest Re=12000 with the suggested scalings. The data used are first plotted in standard form in figure 7.25.

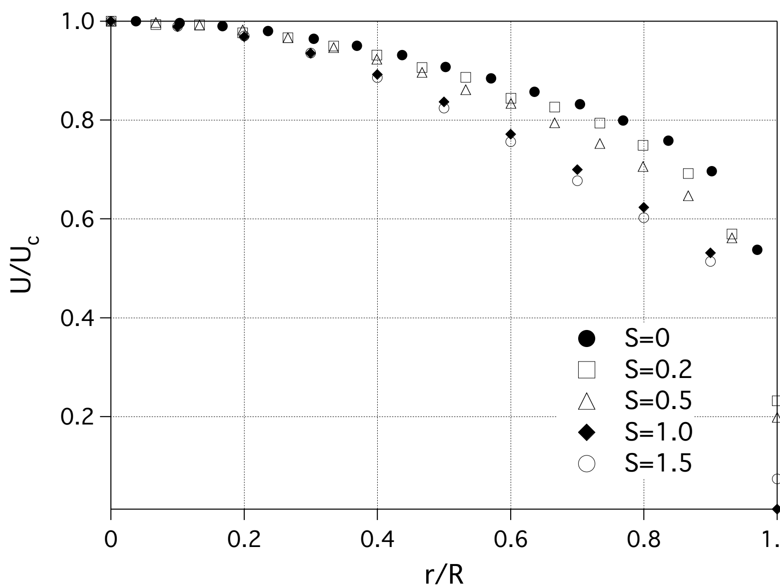

FIGURE 7.25. Mean streamwise velocity data for Re=12000 at five values of S.

One of the scaling laws suggested by Oberlack (1999) is that the mean streamwise velocity profile should have a logarithmic behaviour in the outer part of the flow. In his paper he plotted the data of Orlandi & Fatica (1997) and found such a behaviour in the region $0.5 < r/R < 0.8$ for Re=4900, S=2. In figure 7.26 the present data are plotted in the same way, however a logarithmic region is not as evident as in the data of Orlandi & Fatica (1997). In this figure we have three different values of S and we have fitted lines both with the slope suggested by Oberlack (1999), λ=–1, which gives different regions of fit for the different S. We have also fitted a line in the same region as suggested by Oberlack ($0.5 < r/R < 0.8$) but then the lines will have different slopes, for S=0.5, 1.0 and 1.5 the values are $\lambda = -2.6$, -1.5 and -1.1, respectively.

Again the DNS data help us in clarifying the experiments. Figure 7.27 display the same scenario presented by the LDV data for S=0.5 which infers that the rotation of the pipe has a relevant role in the suggested scaling and the logarithmic behaviour in the outer part of the flow appears only for higher swirl number.

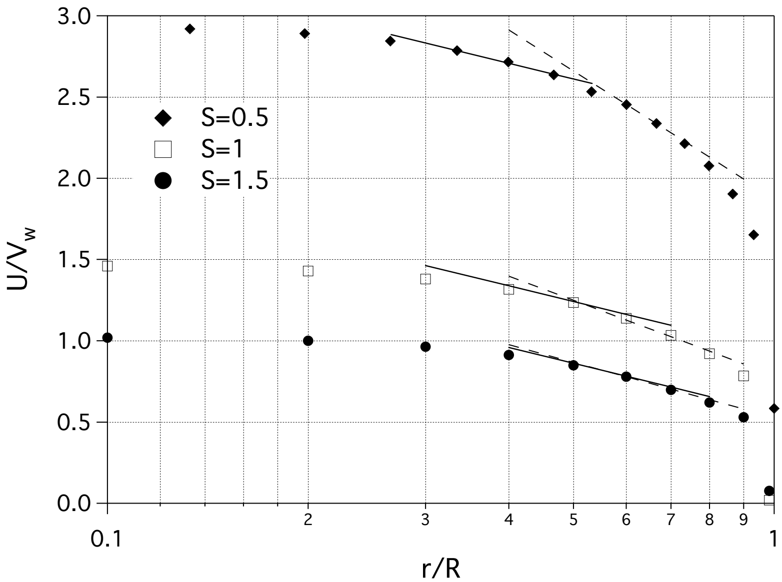

FIGURE 7.26. Mean streamwise velocity U normalised with the wall velocity (V_w) as function of r/R for three different swirl numbers at Re=12000. Full drawn lines: slope –1; dashed lines: slope –2.6, –1.5 and –1.1, respectively.

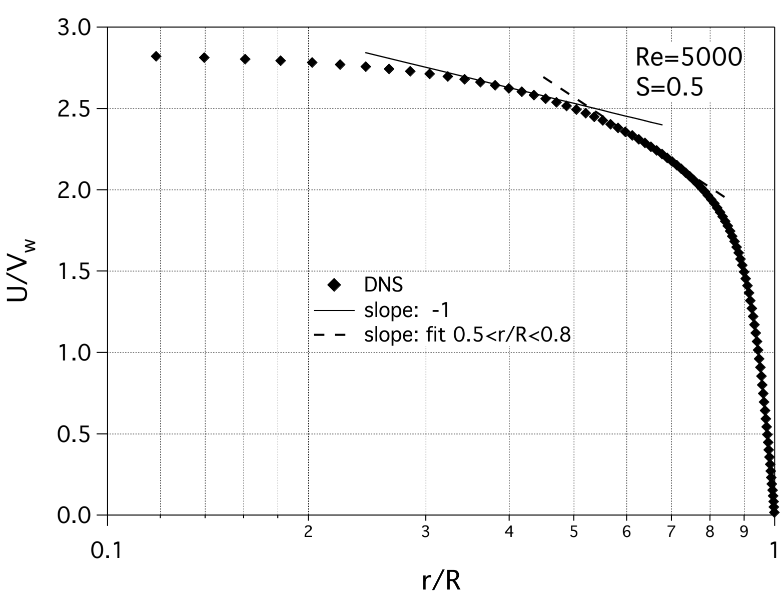

FIGURE 7.27. Mean streamwise velocity U normalised with the wall velocity (V_w) as function of r/R for DNS data at Re=5000, S=0.5. The slope of the dashed line is –2.7.

Figure 7.28 shows the mean velocity data plotted as the velocity defect $(U_c - U)$ normalised with the wall velocity (V_w) as function of r/R. In the figure we have also plotted lines with a slope assuming a quadratic relationship between the velocity defect and the radius. According to the theory of Oberlack, the exponent should be the same as for the azimuthal velocity (see eqs. 3.1 and 3.2) and since we have observed a parabolic velocity distribution for the azimuthal velocity (see figure 7.6) this exponent should then be equal to 2. As can be seen the measurement data show the expected linear (in the log-log-plot) behaviour over a large part of the pipe. As can also be seen the data are displaced downwards with increasing S. This is to be expected since at the wall itself U=0 and there the value would hence be U_c/V_w which can be written $U_c/(U_bS)$, i.e. it is inversely proportional to S. There is of course also a slight variation (increase) of U_c/U_b with S which will tend in the other direction.[1] The slope of the lines corresponds to a quadratic behaviour and as can be seen the data seem to follow this slope closely except near the centreline. All in all figure 7.28 seems to be in accordance with the scaling suggested by Oberlack (1999). And also the DNS data in figure 7.29 are in good agreement with the quadratic behaviour except near the centre of the pipe.

[1]The ratio U_c/U_b for the three swirl numbers in figure 7.28 are 1.47, 1.48 and 1.55 for S=0.5, 1.0 and 1.5, respectively.

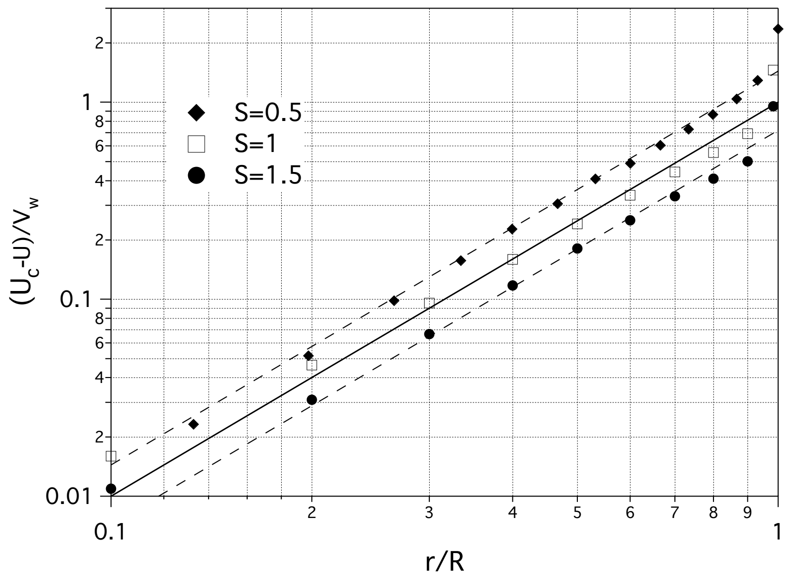

FIGURE 7.28. The velocity defect $(U_c - U)$ normalised with the wall velocity (V_w) as function of r/R for three different swirl numbers at Re=12000.

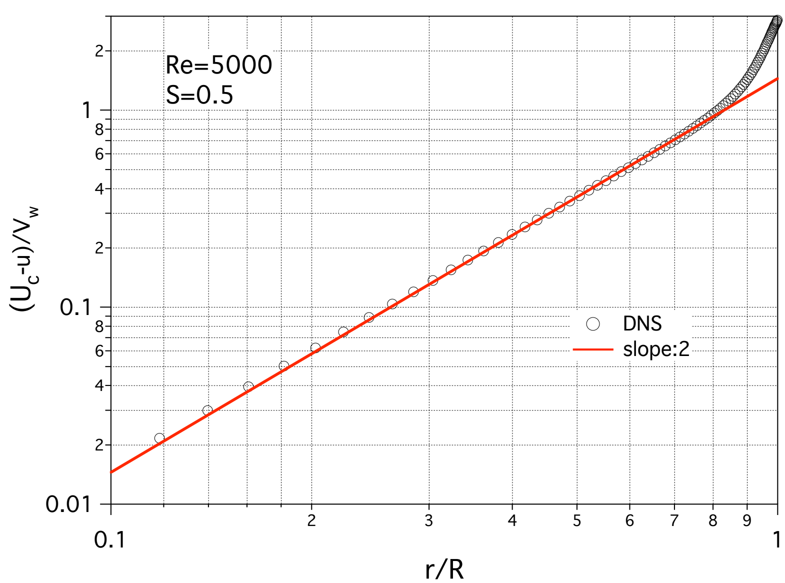

FIGURE 7.29. The velocity defect $(U_c - U)$ normalised with the wall velocity (V_w) as function of r/R for DNS data at Re=5000, S=0.5.

CHAPTER 8

Results for swirling jet flow

This chapter deals with measurements in the near-exit region of the jet, up to $10D$ downstream of the jet exit plane. Section 8.1 deals with the mean flow development, whereas section 8.2 shows the behaviour of all three fluctuating velocity components. Section 8.3 discusses the instantaneous flow angles and the limitations of hot-wire versus LDV-measurements in the jet. Finally section 8.4 investigates the central region of the swirling jet where an interesting phenomenon has been observed, namely that the central part becomes counter rotating at some distance downstream the outlet. This result is verified through both LDV and stereo PIV measurements and is also indicated by the simulations.

8.1. Mean flow development

The evolution of the mean axial velocity profile at three downstream positions with and without swirl is shown in figure 8.1. Here we have chosen to present the data for Re=24000 at S=0 and S=0.5, but similar measurements were also made for the other values of the flow parameters (Re and S). The graphs clearly show how the intial profile at the pipe outlet is more peaked for the swirling flow case. At short distances downstream of the pipe outlet, $x/D \leq 2$, the axial velocity in the central region of the jet is fairly unaffected, whereas further downstream at $x/D = 6$, i.e. downstream of the potential core region, the velocity in the central region becomes significantly smaller for the rotating case. It is interesting to note that the figure shows that the different profiles have a common crossing point at about $\mid r/R \mid= 1$ and U/U_b=0.6, a characteristic that is also found in the other measurements at Reynolds number Re=12000 and Re=33500 and at S=0.2.

Figure 8.2 shows the averaged (in azimuthal direction) axial velocity profiles obtained from the DNS calculations in the suddenly expanded pipe for Re=10000 at S=0.5. The temporal evolution of the jet is transfered into the spatial evolution using x=tU_b. Although in the simulation the radial expansion is ruled only by the diffusivity since the mean radial component is equal to zero, the flow field behaves like a jet without any entrainment (the code enforces mass flow conservation). Still it is possible to observe a common crossing point close to $r/R \approx$1 until $x/D \approx$5 even though the velocity is lower as compared to the experiments.

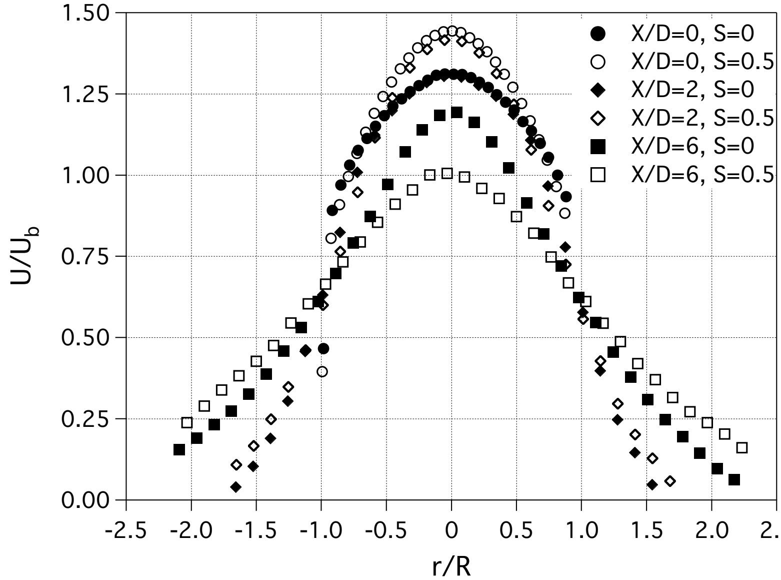

FIGURE 8.1. Mean axial velocity: Re=24000, S=0, 0.5.

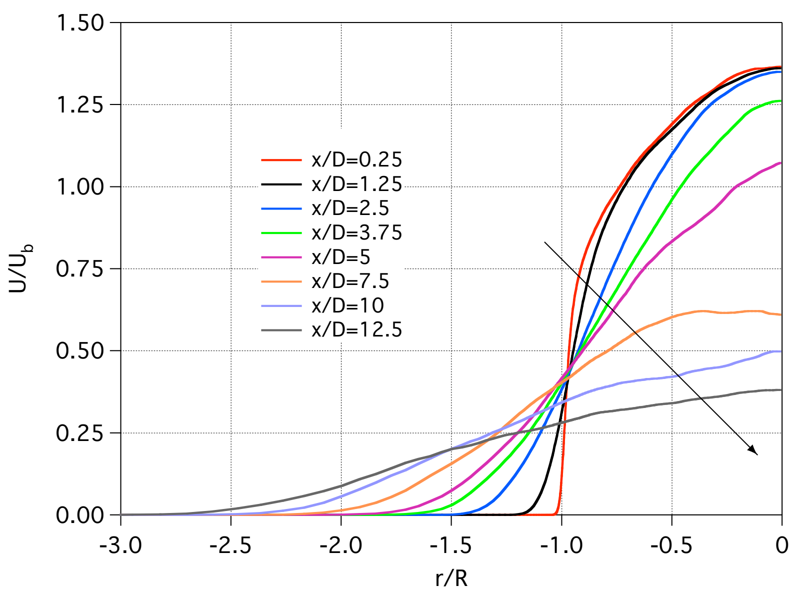

FIGURE 8.2. Instantaneous axial velocity from DNS. Re=10000, S=0.5. The arrow shows the direction of increasing x/D.

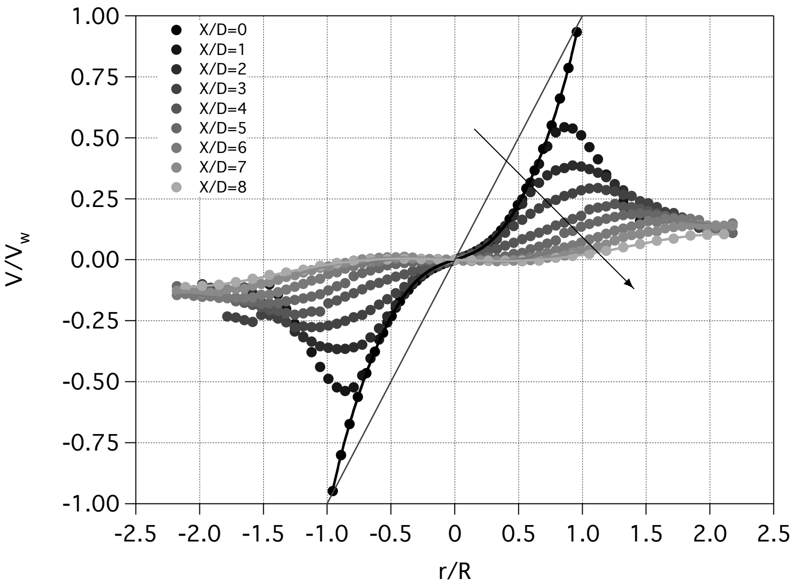

FIGURE 8.3. Mean azimuthal velocity. Re=24000, S=0.5. The arrow shows the direction of increasing x/D.

Figure 8.3 shows the downstream evolution of the normalised mean azimuthal velocity (V/V_w) profiles. As presented in chapter 7, the velocity profile at the pipe outlet closely follows a profile proportional to $(r/R)^2$ (the lines in the plot are polynomial fits for visual aid). The figure indicates that further downstream the radius of the potential core decreases but the "parabolic" nature of the azimuthal velocity seems to persist in the central region at least until three diameters downstream the pipe outlet. From the figure it is possible to deduce how fast the azimuthal velocity decays in the jet: the maximum velocity decreases to almost 50% of the pipe wall velocity in only one diameter. This is due to the entrainment of the fluid surrounding the flow issued by the pipe. At x/D=8 the maximum azimuthal velocity is reduced to about 10% of V_w and moved to $r/R \approx 2$.

The radial component of the mean velocity field was only measured for one swirl number i.e. S=0.5. The mean radial component normalised with the bulk velocity is shown in figure 8.4. As can be noticed, the measurement denoted as being at x/D=0, the closest to the pipe outlet position reachable with the LDV system, i.e. just a few tenths of a millimeter from the end of the pipe wall, already shows a non-zero mean component. At x/D=1 the core of the jet presents the same behaviour as seen at the pipe outlet but suddenly, at $r/R \gtrsim 0.5$ the radial velocity increases, reaching a maximum at about r/R=1.

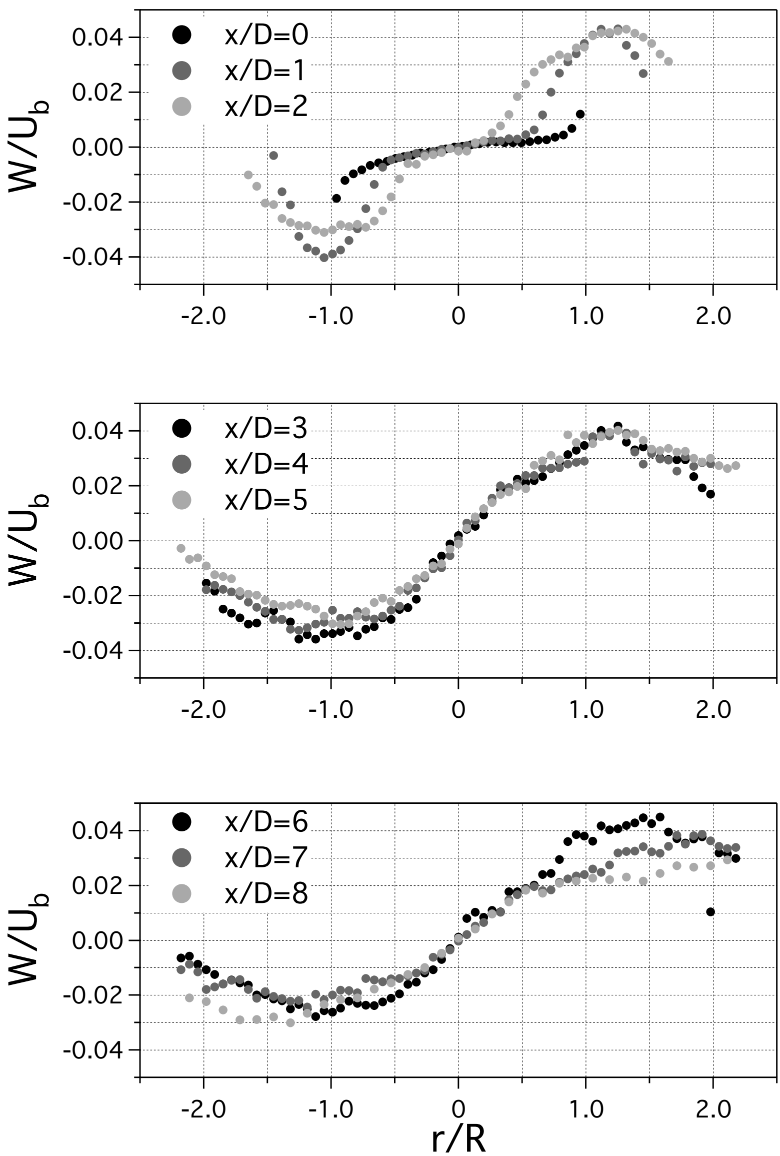

FIGURE 8.4. Mean radial component at Re=24000 S=0.5.

Following the downstream development it seems that the curvature of the profiles changes sign in the central part of the jet: comparing the region for $|r/R| \leqslant 0.5$ of the profiles at x/D=2 and 3 or at a larger downstream distance the change of the curvature becomes clear.

Furthermore it is worth to note that the radial component represents only a few percent compared with the bulk velocity of the jet but is comparable with the azimuthal velocity especially for $x/D \gtrsim 5$. In general the data look a bit scattered but the velocity profiles do not change drastically moving downstream: the slope, the radial position of the maximum and the value itself are fairly similar for $3 \leqslant x/D \leqslant 6$. It is seen to have a maximum around $|r/R|$=1 at all x-positions. The behaviour of the radial component can be understood from the time-averaged continuity equation, which for the axisymmetric case becomes (see also eq. 6.2)

$$\frac{\partial W}{\partial r} + \frac{W}{r} + \frac{\partial U}{\partial x} = 0$$

Since the streamwise mean velocity U increases with x in the outer part (for $r > R$) of the jet, $\frac{\partial U}{\partial x}$ is positive there and hence negative for $r < R$. W is directed outwards and is therefore positive. This means that $\frac{\partial W}{\partial r}$ needs to change sign, from positive to negative, when r increases, which is also observed in figure 8.4.

8.1.1. *Flow entrainment*

An interesting quantity of the jet is the entrainment of outer fluid into the jet. The entrainment may be obtained by integrating the streamwise velocity across the $r\theta$-plane which then will give the total axial flow rate. We will denote this quantity by Q and normalise it with Q_0, which is the axial flow rate coming from the pipe. This ratio is denoted the entrainment coefficient. However, the calculation may be affected by a significant uncertainty. Indeed, the flow in the outer part of the jet is measured with difficulty due to the low velocities and may give large error contributions due to the weighting with the radius. To reduce this problem a least square fitting procedure (using a Gaussian function to estimate the tails of the profiles) was used in order to extrapolate the mean velocity profiles in the external part of the jet. The flow rate values are reported in Table 8.1. The accuracy of the above measurement was assessed by checking that the overall amount of flow momentum remains constant moving downstream for S=0. These values are also given in the table and as can be seen they show a reasonable constancy between the two positions, giving confidence in the calculation of the entrainment coefficient.

Table 8.1 shows that an increase of the flow rate is observed by moving downstream for all the configurations analysed. This is due to the engulfment of ambient fluid by the vortical structures and by turbulent mixing. The swirl increases significantly both the entrainment and the jet spreading. This is also confirmed by the flow visualisations shown in figure 8.5. This enhancement of the entrainment due to the pipe rotation seems to be reduced by increasing

		Q/Q_0			G_x (N)
Re	x/D	S=0	S=0.2	S=0.5	S=0
12000	2	1.53	1.62	2.00	0.0373
	6	2.49	2.81	3.15	0.0404
24000	2	1.43	1.52	1.58	0.143
	6	2.36	2.47	2.92	0.145
33500	2	1.37	1.40	1.52	0.272
	6	2.20	2.33	2.72	0.260

TABLE 8.1. The entrainment coefficient (Q/Q_0) for three different swirl numbers. As a comparison the constancy of the axial momentum flux (G_x) for the S=0 case was also checked using the same data.

the Reynolds number. The reason for this Reynolds number dependence is not clear. By looking at the flow visualisations it may be suggested that it is an effect related to the more regular eddy structures formed in the mixing layer at low Re, which may enhance the entrainment of fluid from the environment.

The flow visualisation of the cross section at the pipe outlet point out the differences between the stationary and the swirling jet. As can be seen in figures 8.6 and 8.7 the non-rotating case presents small wavy disturbances at the border of the jet while the swirling jet exhibits bigger radial structures which run azimuthally. These instabilities, present already at the early stages of the jet, are may be one reason for the larger entrainment observed for the swirling jet.

a)

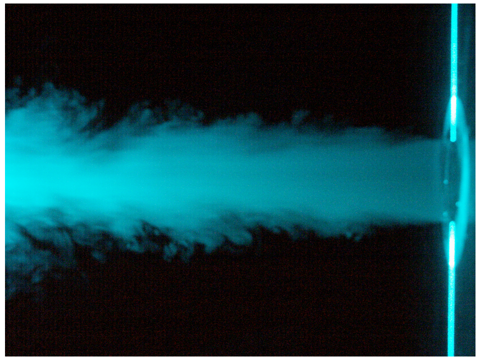

b)

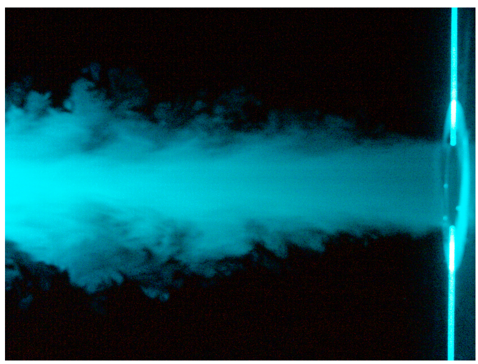

c)

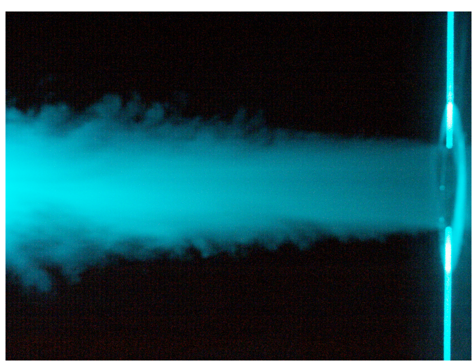

d)

FIGURE 8.5. Smoke flow visualization. a) Re=12000, S=0, b) Re=12000, S=0.5, c) Re=24000, S=0, d) Re=24000, S=0.5

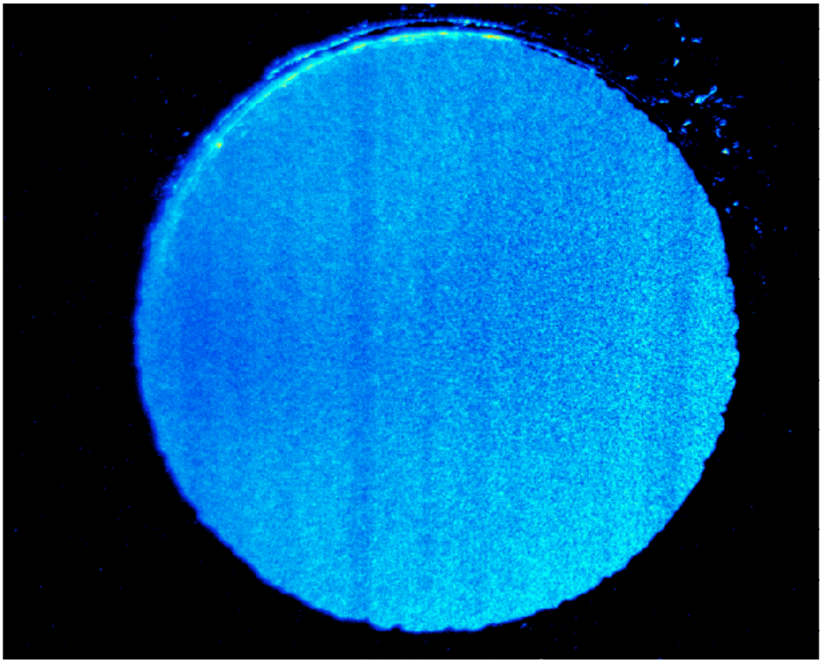

FIGURE 8.6. Smoke flow visualization at the pipe outlet: Re=24000, S=0.

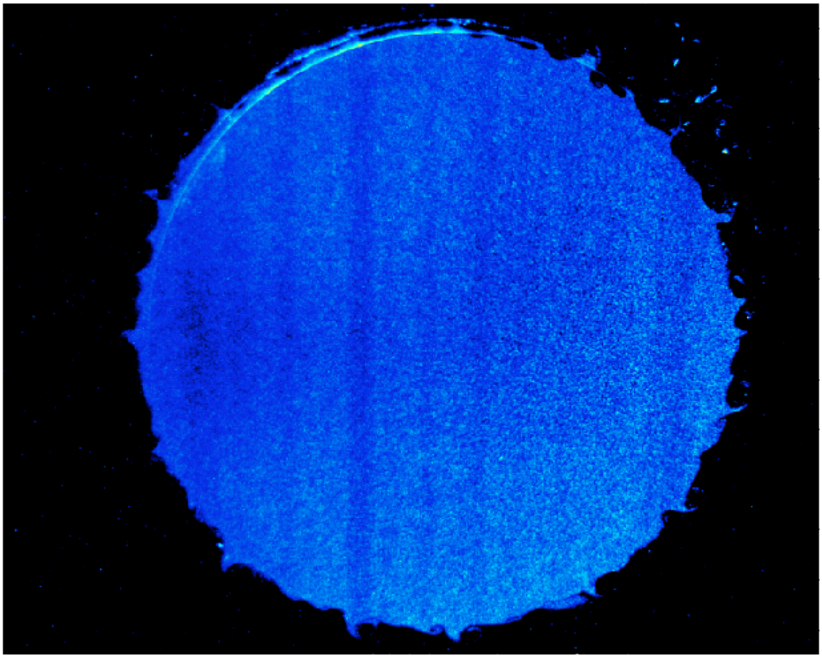

FIGURE 8.7. Smoke flow visualization at the pipe outlet: Re=24000, S=0.5. Rotation direction is clockwise.

8.1.2. *The axial decay*

The mean axial velocity along the centreline, U/U_b, its dependence on swirl rate and Reynolds number are shown in figures 8.8 and 8.9. The figures indicate that the axial development of the jet from the pipe outlet to x/D=10 could be separated into two regions, i.e. the mixing region and the transition region (see Beér & Chigier 1972). The first region extends from the pipe exit to 3–4 pipe diameters downstream, where the potential core ceases, while the second region covers the incipient part of the developing jet flow.

Close to the outlet the velocity decay along the axis is small, approximately linear and the axial velocity becomes higher with increasing swirl rate as has been observed at the pipe outlet (cf. figure 7.1). The small decrease of the axial velocity going downstream is explained by the flattening of the velocity profile in the central part of the core whereas the increase in centreline velocity is due to the development of a less blunt velocity profile at the outlet with increasing rotation (see figure 8.1).

In the region downstream of the potential core the velocity decrease is substantially larger than without rotation and increases with swirl rate whereas the variation in slope with Reynolds number is small. Another effect of the swirl seen in the figures is the influence on the form of the velocity decay curve. Without any swirl the decay is almost linear but for increasing swirl the straight line becomes gradually more curved.

Included in figure 8.9 are also data from the experiment by Rose (1962). That experiment is similar to the present in that the jet emerged from a stationary and rotating pipe with L/D = 100 at about the same Reynolds number. The data from the non-rotating cases fall on top of each others while in the rotating case the trend is the same but the fall off is still higher which may be partly explained by the somewhat higher swirl number (S=0.63).

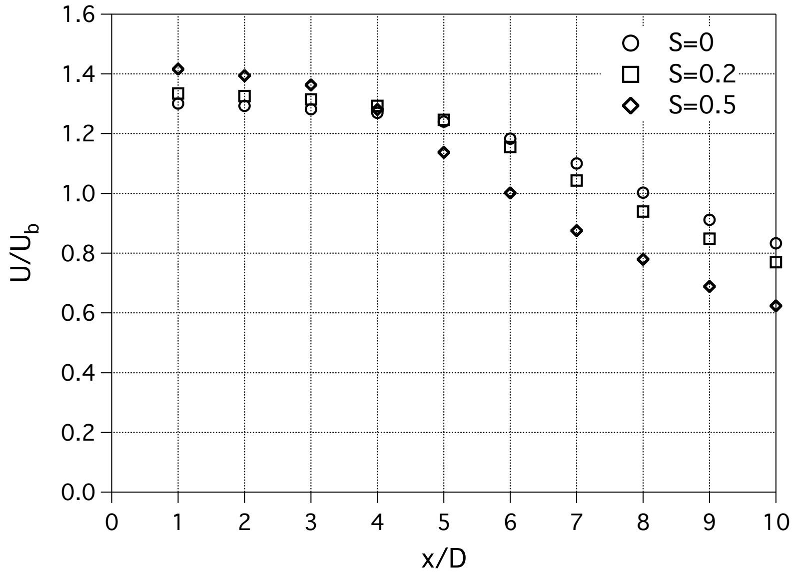

FIGURE 8.8. Axial velocity at the centreline Re=24000, S=0, 0.2, 0.5.

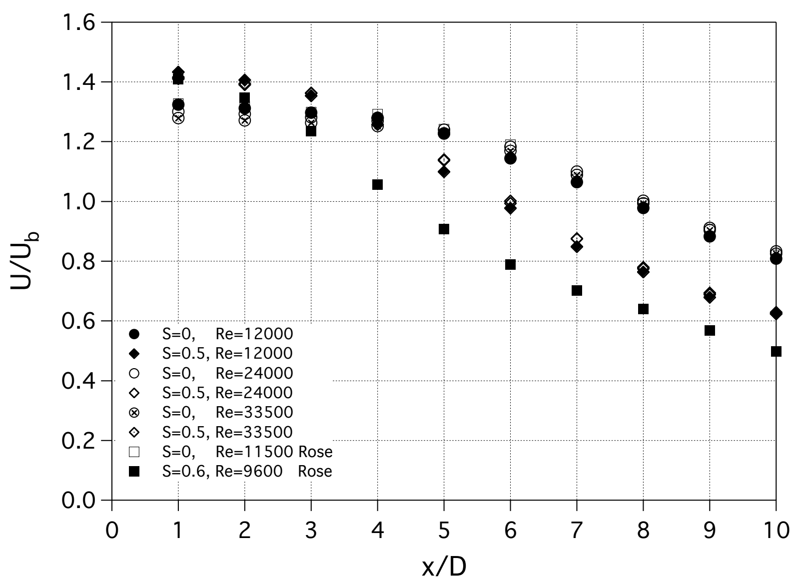

FIGURE 8.9. Axial velocity at the centreline. Re=12000, 24000, 33500; S=0, 0.5.

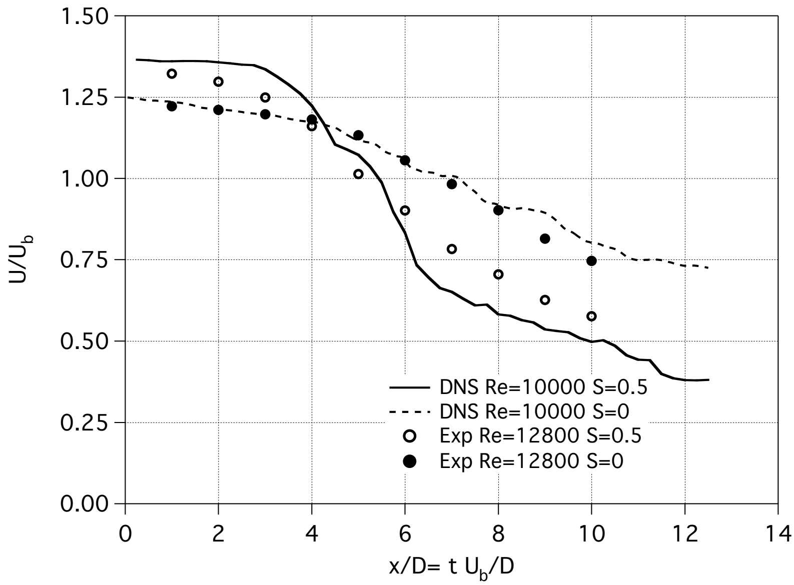

FIGURE 8.10. Axial velocity at the centreline: comparison between DNS calculation and LDV data for S=0.5.

From the DNS calculation it is possible to get the instantaneous axial velocity decay of the jet. In figure 8.10 the comparison between experiments and simulation is taken into consideration. The Reynolds numbers examined are quite close. Again there is the need to remember that in the DNS no entrainment is allowed and the jet expansion is given only by the diffusivity. Surprisingly, the case of the non-swirling jet shows a good agreement between LDV data (full circle) and the DNS (dashed line) at least until 8 diameters downstream. After this station the two curves start to diverge and this is probably because the jet total momentum is decreasing.

The presence of a swirling component instead changes quite drastically the behaviour of the jet in the simulation. Since the rotation greatly influences the entrainment as already discussed, the DNS is not able anymore to follow the correct trend of the jet. Clearly, although starting from very similar values at the pipe exit, the axial decay in the simulation is much slower compared to the real jet that means also the simulated profile does not expand as fast as in the real swirling jet so that the potential core, almost non-existent in the LDV data, is much longer. After 3 diameters this tendency change, and the axial decay in the calculation is much higher. The curves cross each other and, for $x/D \gtrsim 5$ the simulation shows lower axial velocities than the LDV swirling jet as can be noted also from the profiles presented in figure 8.2.

8.2. Turbulence development

This section deals with the development of the turbulence distributions across the jet. Axial profiles have been measured at the pipe outlet (x/D=0) and at two downstream positions (x/D=2 and 6) while azimuthal and radial profiles are investigated each diameter from the pipe outlet until x/D=9. We chose to show data for Re=24000, S=0 and 0.5 although profiles have been taken also for other flow parameters.

8.2.1. *Streamwise velocity fluctuations*

In figure 8.11 the streamwise turbulence intensity (u'/U_b), is compared for a jet with and without swirl at Re=24000 and three different downstream positions, x/D=0, 2 and 6. Only small differences close to the centreline are observed at the pipe outlet. Further downstream the turbulence intensity u'/U_b increases and at x/D=2 both profiles have a maximum around r/R=0.8. At x/D=6 the main difference between the swirling and non-swirling jet is found around the centreline where the turbulence level is almost doubled as the swirl number S is increased from 0 to 0.5.

The higher moments of the axial velocity at Re=24000 are shown in the figure 8.12 both with and without swirl. Also here we have plotted the data for the S=0 and S=0.5 cases in the same diagram. Data points were taken across the full width of the jet, but since higher moments need more data these points have more scatter. Since the jet is axisymmetric we decided to take the average of the points measured at equal r-positions at both sides of the centreline and in that way the scatter was decreased. In the figures the data for each x/D are shifted in the vertical direction but the thicker horizonal lines in each figure shows the zero-level for the skewness and the Gaussian level of three for the flatness.

At the pipe outlet both skewness and flatness are only marginally influenced by the swirl rate which is clearly shown in the figures and in line with the u' results. The skewness rises from -0.5 at the centre to around 0 close to the wall while the flatness decreases from 3.5 to 2.8 for the corresponding points. These data could be compared with results obtained by Eggels *et al.* (1994) in non swirling pipe flow at $Re \approx$7000. Data are not provided over the whole pipe radius, but at r/R=0.5 skewness and flatness are -0.5 and 3.2 respectively and at r/R=0.9 they are 0 and 2.2 respectively which is close to the present results. The strong influence of rotation is found around the centreline, $\mid r/R \mid \leq 0.5$, at x/D=6 and in the mixing layer at position x/D=2. In the central region downstream of the potential core (x/D=6) both skewness and flatness changes dramatically with the rotation rate whereas the influence is small at other radial positions. At the centreline, increasing the swirl number, the skewness increases and the flatness decreases from –1.2 to –0.3 and from 4.8 to 2.5 respectively.

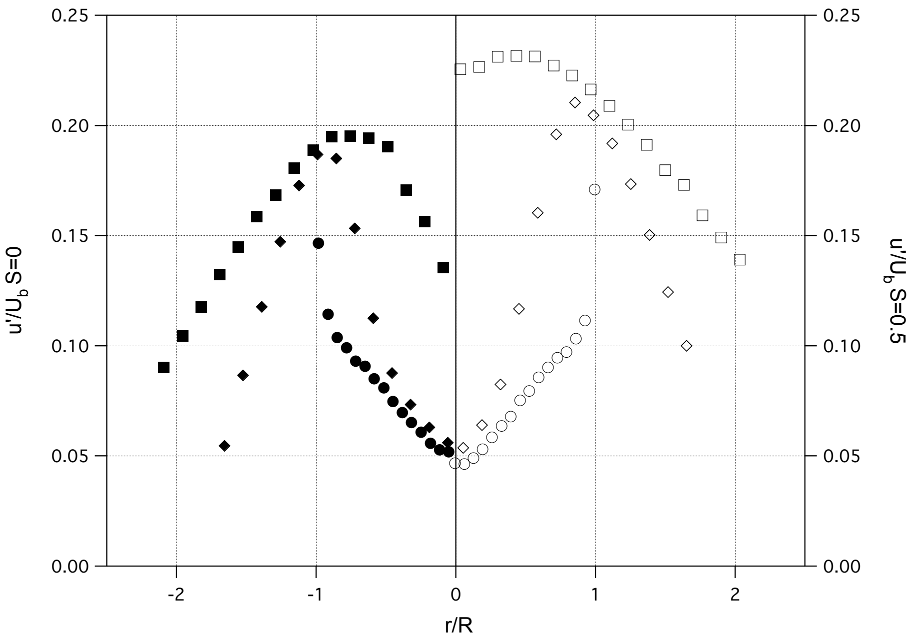

FIGURE 8.11. Axial turbulence intensity at Re=24000, S=0 (left side, filled symbols) and S=0.5 (rigth side, open symbols), for three axial positions: ○: x/D=0; ◇: x/D=2, □: x/D=6.

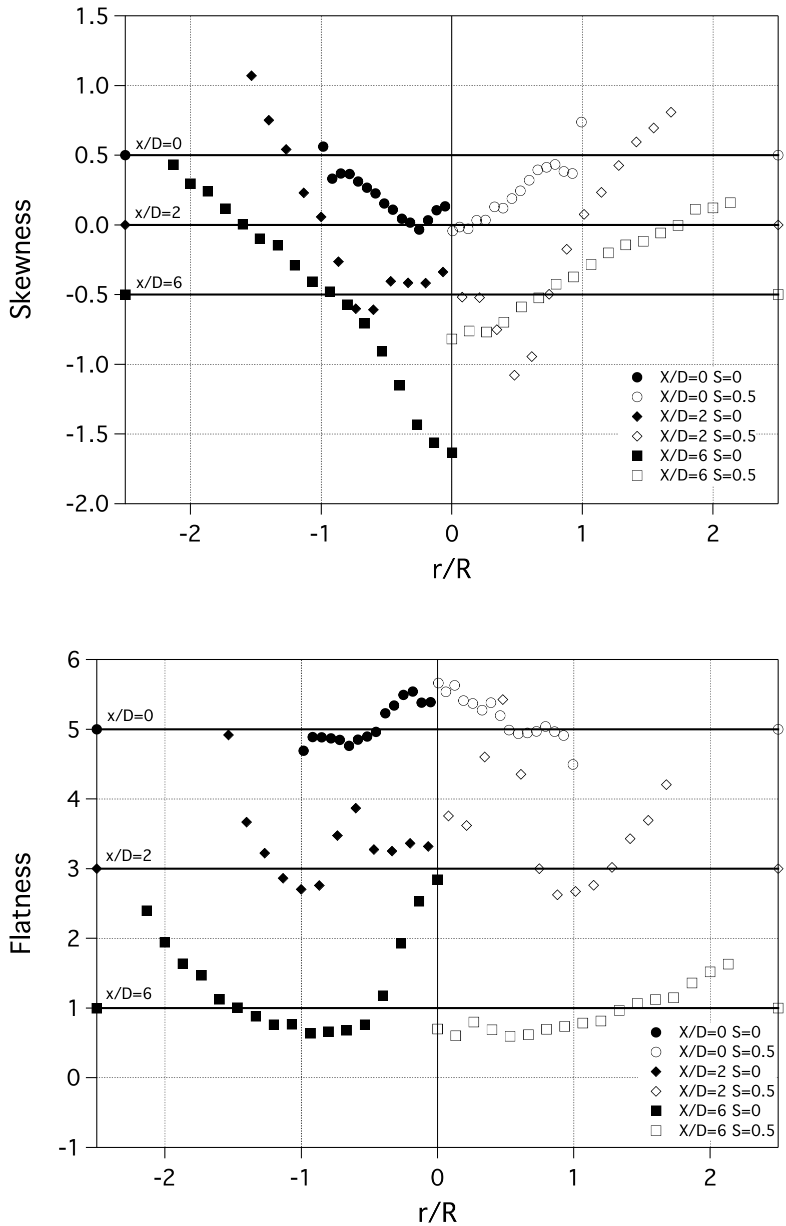

FIGURE 8.12. Skewness (a) and flatness (b) of the axial velocity at Re=24000 for three different x–positions and with S=0 and 0.5. Note that the profiles have been shifted in the vertical direction. The thick horizontal lines show the where the skewness and flatness are 0 and 3, respectively.

8.2.2. *Azimuthal and radial velocity fluctuations*

The development of turbulence level of the azimuthal and radial velocity components for Re=24000 and S=0.5 are shown on the top of figure 8.13 and in figure 8.14. The azimuthal component is represented with the circle and the radial component with the square. As expected the azimuthal and the radial turbulence intensities coincide at the centreline of the jet: only small differences can be noted moving further downstream. The biggest gap between the two turbulence intensities is at the pipe outlet, see figure 8.13. Then the experimental data lay almost on the same curve in the central and in the outer part of the jet while they differ in the region of the peak where the azimuthal turbulence intensity reaches higher values. The maximum is at about r/R=1 for x/D=1, then it moves gradually towards the centreline as the shear layer penetrates into the jet until, for $x/D \gtrsim 7$ both the profiles become pratically flat in the core of the jet. Note also that their values decrease. As anticipated from the pipe fluctuations, even in the jet the azimuthal and the radial turbulence intensities are lower than the axial one.

The skewness and flatness reveal some more details of the jet structure (see figures 8.13, 8.15 and 8.16). For both components the skewness is antisymmetric around the centre which is what one would expect for an axisymmetric flow. At x/D=1 the skewness for v and w shows a local maximum (minimum) at $|r/R| \approx 0.8$. This is most probably an effect of the instability affecting the potential core. It is interesting to note that this position does not correspond to the maximum in the rms, in fact the maximum in rms is approximately where the skewness is zero. Moving downstream the skewness for the azimuthal component becomes monotonic before (x/D=5) than in the radial component which, on the other hand, results to be stronger in all the investigated flow field. Only in the central part of the jet they become comparable for $x/D \gtrsim 6$ where the skewness for the azimuthal component becomes very small in all the radial position except at the outermost points. This seems to indicate an almost Gaussian distribution of the fluctuations which is also substantiated by the flatness which is close to 3. However the skewness for the radial component increases (decreases) almost linearly with r indicating regions of large fluctutations directed towards the external part of the jet.

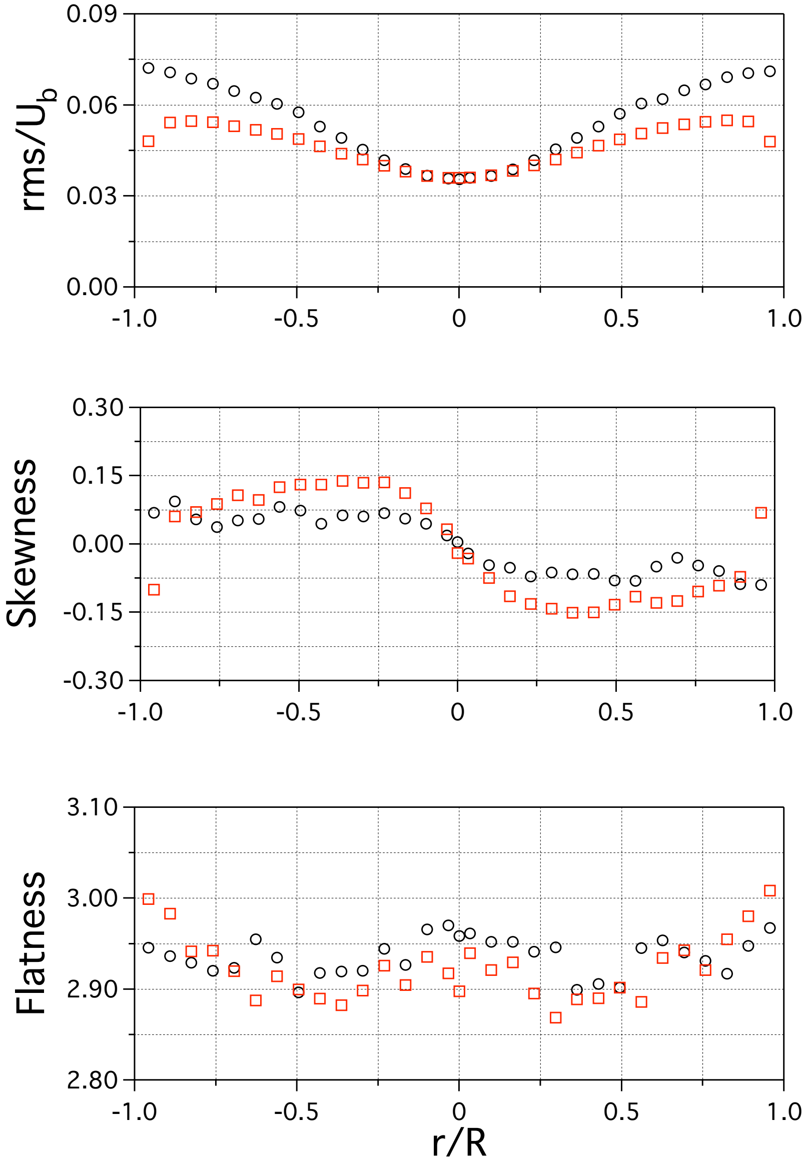

FIGURE 8.13. Turbulence intensity, skewness and flatness of azimuthal ○ and radial □ velocity at Re=24000, S=0.5 x/D=0.

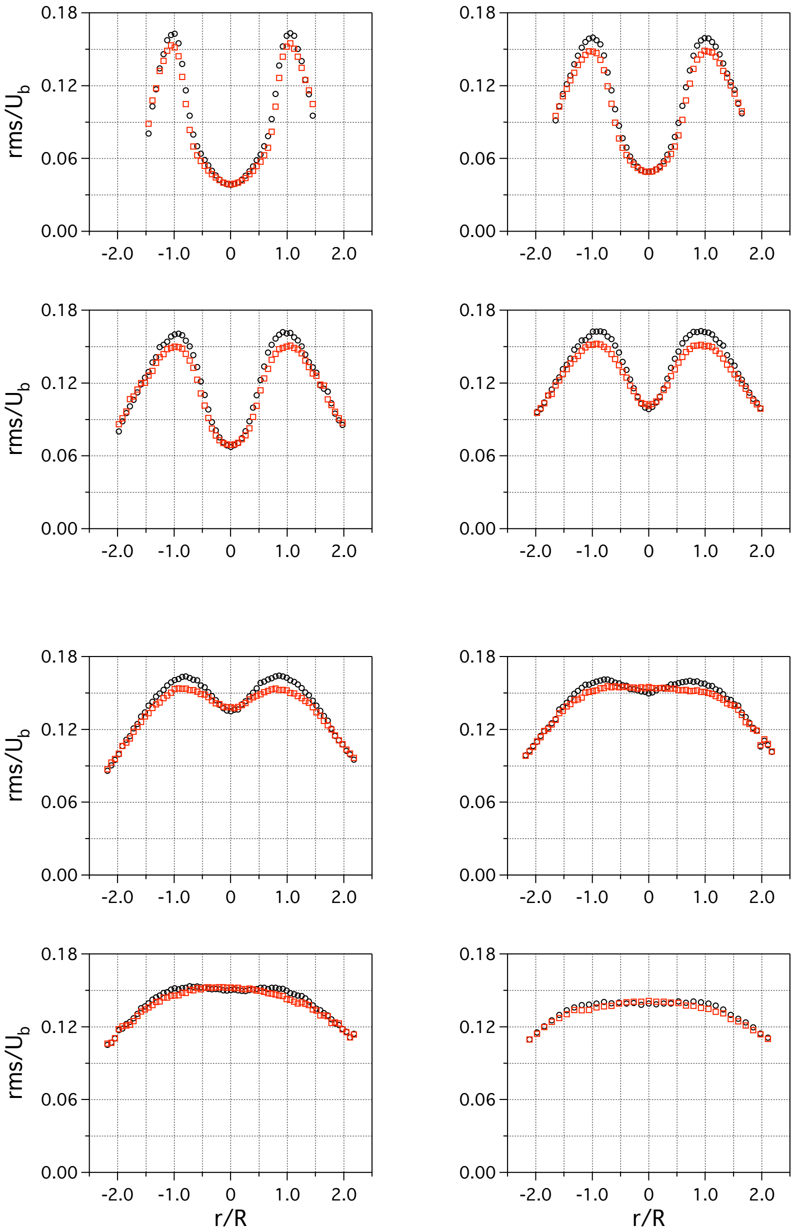

FIGURE 8.14. Azimuthal ○ and radial □ turbulence intensity at Re=24000, S=0.5 from x/D=1, top-left corner, to x/D=8, bottom-right corner.

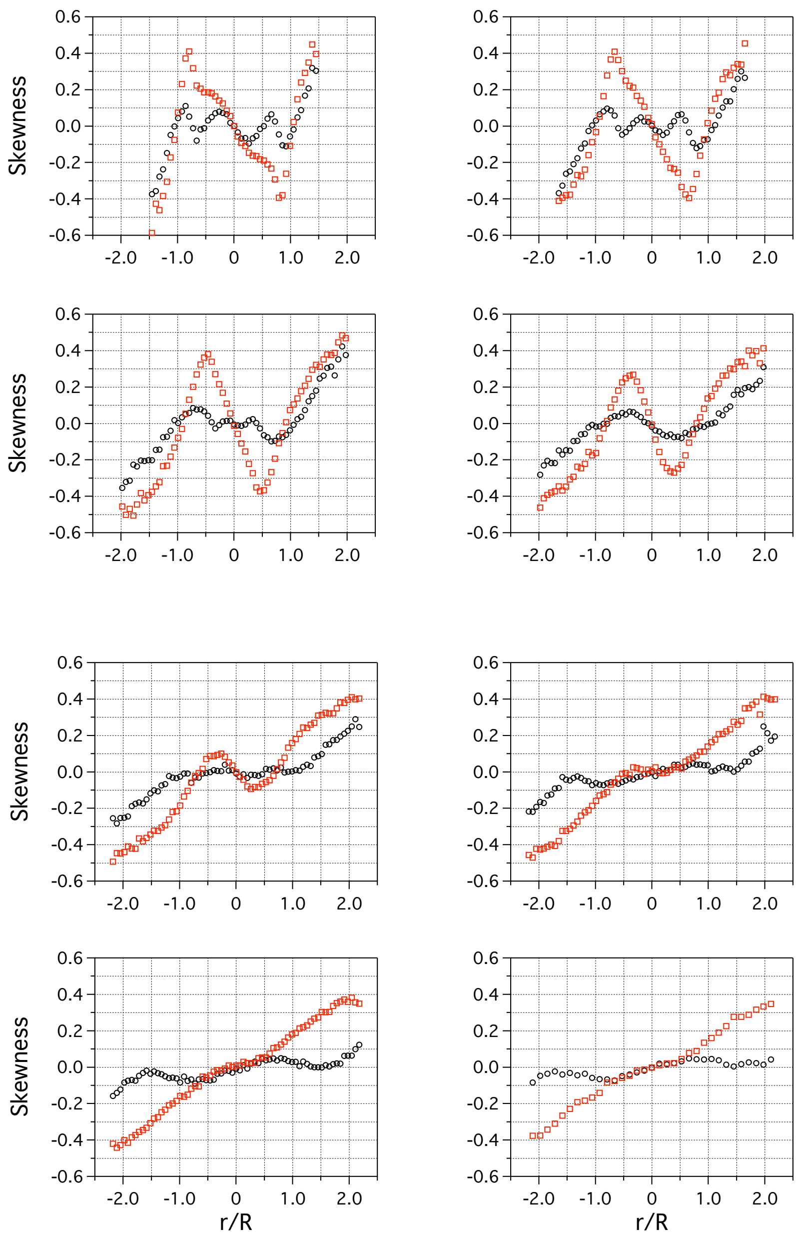

FIGURE 8.15. Skewness of azimuthal ○ and radial □ velocity at Re=24000, S=0.5, disposition of the figures as for the turbulence intensity.

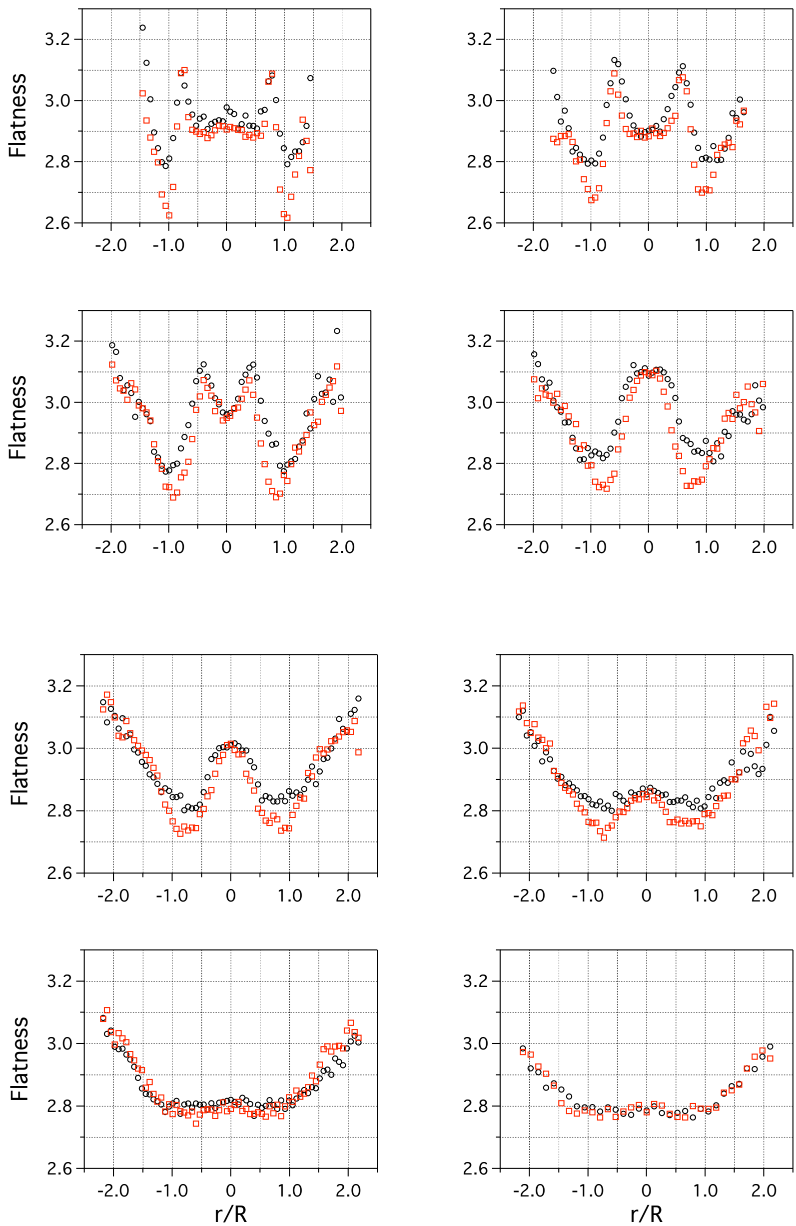

FIGURE 8.16. Flatness of azimuthal ○ and radial □ velocity at Re=24000, S=0.5, disposition of the figures as for the turbulence intensity.

8.2.3. *Axial development of turbulence*

The variation of the turbulence level on the centreline as function of the downstream distance is shown in figures 8.17 and 8.18. Data were obtained for the three Reynolds numbers (12000, 24000 and 33500) and three values of the swirl number (0, 0.2 and 0.5). The data presented in the two figures were obtained with LDV and hot-wire anemometry, respectively. There are of course also data for the streamwise fluctuations available from the hot-wire measurements and they are in good agreement with the LDV-data (at worst a 10% difference). We therefore restrict ourselves to present only the LDV-data in figure 8.17.

The variation of the turbulence level of the axial component (u'/U_b) along the x-axis, is shown in figure 8.17a–c. The turbulence level close to the outlet is only weakly affected by Reynolds number and swirl rate. There is also an initial region where there is only a weak increase in the turbulence level (up to x/D=2–3). We have earlier denoted this the "potential" core region. Downstream this region the turbulence level increases significantly, reaches a maximum around x/D=6 and then decreases. The curves seem to cross around $x/D = 10$. It is clearly seen that the onset of the increase in turbulence level moves upstream as the swirl is increased due to the enhanced mixing (with the associated decrease in core length) and that the maximum of the turbulence moves likewise. However the axial position of the peak is almost constant for each swirl rate irrespectively of the Reynolds number. All in all one may say that for the present Reynolds number range there is a very small variation in the beaviour of the turbulence at the centreline. Finally we have included data from Rose (1962) in figure 8.17a. For the non-rotating case these data overlap with the present data, for the rotating case the data of Rose (1962) show an even larger effect of the rotation than in our case. To some extent this may be due to the fact that their swirl number was 0.6 as compared to the highest in the present study which was 0.5.

Figure 8.18 shows the axial development at the centreline of the turbulence level for the orthogonal component v'/U_b.[1] These data show a similar picture as for the u_{rms}-data, there is only a small influence of the Reynolds number, but a significant influence of the swirl. It can also be noted that the initial increase of v_{rms} seem to start somewhat closer to the exit than for the streamwise fluctautions. This may be due to the fact that even in the potential core large scale structures in the outer region may give a "buffeting" to the core which gives rise to fluctuations in a plane normal to the streamwise direction.

[1]We chose to call this component "orthogonal" at the centreline since the azimuthal component is not well defined there.

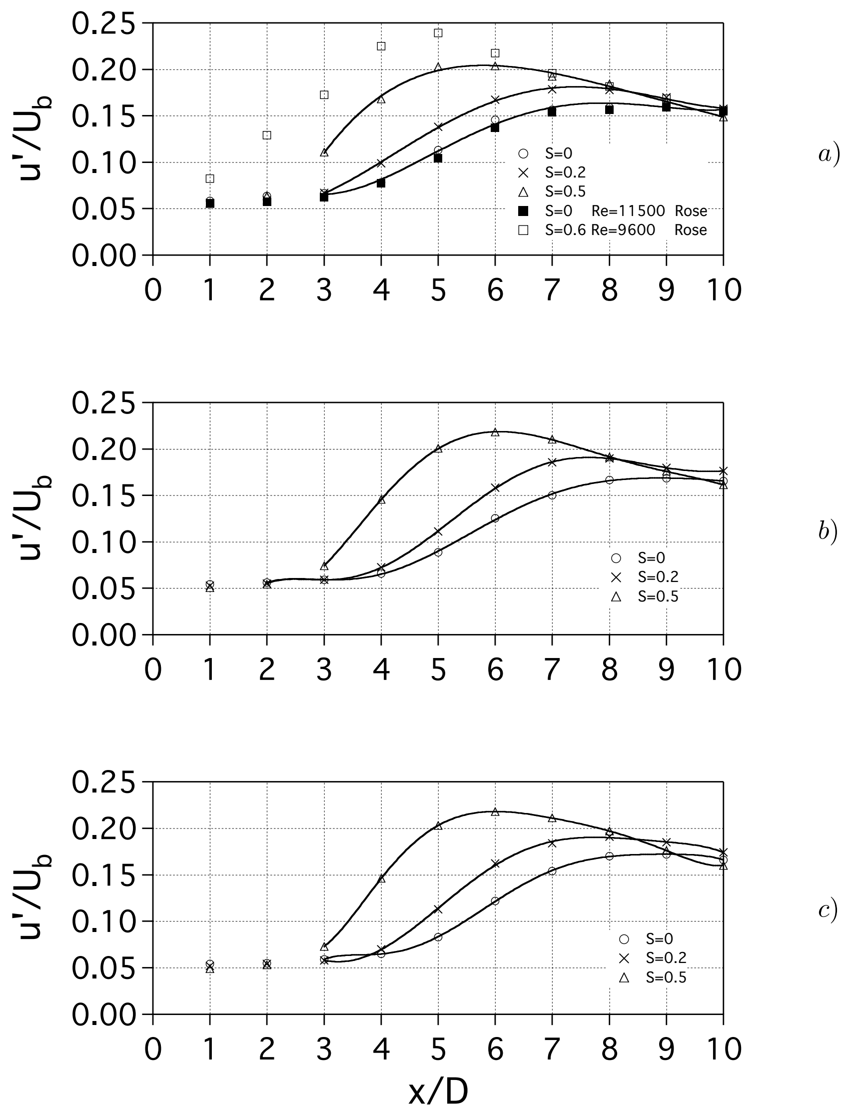

FIGURE 8.17. Turbulence intensity of the streamwise velocity component at the centreline, a) Re=12000, also includes data from Rose (1962), b) Re=24000, c) Re=33500. Full lines are for visual aid only.

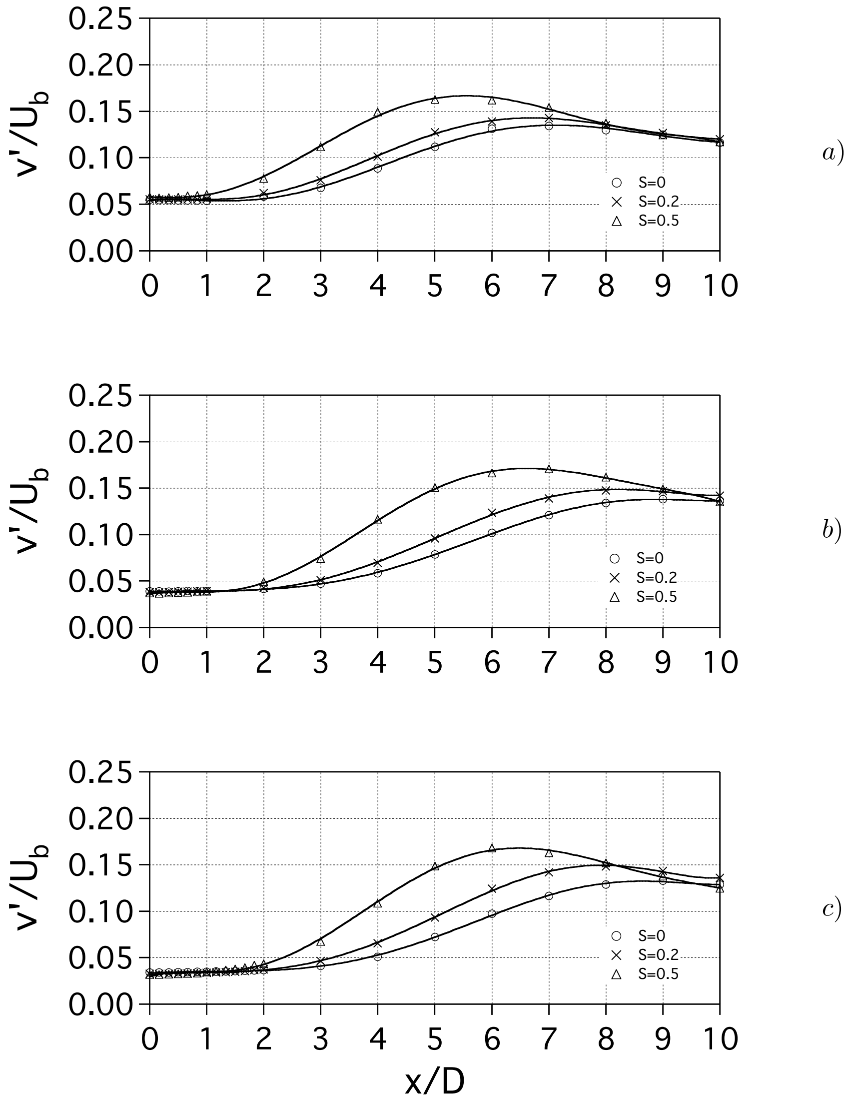

FIGURE 8.18. Turbulence intensity of the orthogonal velocity component at the centreline, a) Re=12000, b) Re=24000, c) Re=33500. Full lines are for visual aid only.

8.2.4. *Spectral information*

The flow field in the near-exit region of the jet is quite complex and in order to understand the development of the flow structures time resolved measurements as well as two-point measurements are needed to get the temporal and spatial evolution of the flow field. This is beyond the scope of the present work but in order to give some information concerning the vortical structures we will present a few results obtained from spectral analysis. For this analysis we use hot-wire anemometry data which was collected by an X-probe. The data were taken at the centreline at x/D=2 and 6 for Re=33500. Both the streamwise (u) and the orthognal (v) components were analysed. The spectra are shown in figures 8.19 and 8.20.

Figure 8.19a shows that at x/D=2 a distinct peak in the u-components is detected for all three swirl numbers. If the frequency is normalised by the bulk velocity and pipe diameter, a Strouhal number of about 0.5 is obtained, which remains constant for all swirl numbers studied here. This peak is also present at the other Reynolds number studied. The St-value of 0.5 is within the range of values reported in previous studies (see section 4.1.1). It is interesting to compare with the spectra measured at the pipe outlet which show no evidence of a similar peak (see figure 7.18).

Since the spectra here are plotted in such a way that the area under the spectra is directly proportional to the energy content of the signal it is clear that the rms for the three signals are fairly similar although the S=0 case is the one with the largest rms (cf. figure 8.17c). However in figure 8.19b we see a dramatic change in the spectra. First of all there is now large differences in energy content between the three different swirl numbers, and in contrast to the situation at x/D=2 the S=0.5 case shows the largest energy. The distinct peak that previously was easily seen has also disappeared and the spectra now has a broad band character. The maximum varies between St=0.35 for S=0.5 to St=0.55 for S=0. The broadening of the spectra is due to the interaction and breakdown of the structures and the spectra obtain a shape which is typical for turbulent jets.

Also the spectra (figure 8.20) of the orthogonal component show a similar behaviour, however at x/D=2 the largest peak is seen for S=0.5. In this case the Strouhal number of the peak seem to change somewhat with S. At x/D=6 the spectra broadens much in the same way as was observed for the spectra for the streamwise component.

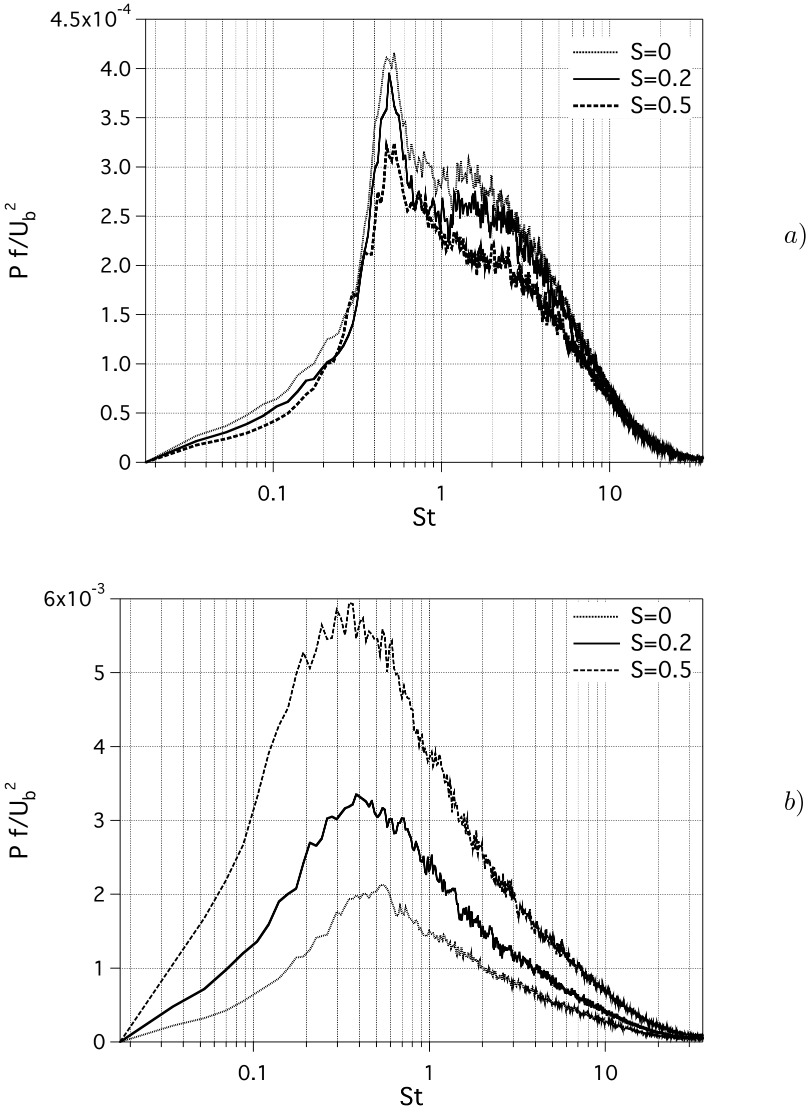

FIGURE 8.19. Spectra of u-component at centreline for Re=33500. a) x/D=2, b) x/D=6.

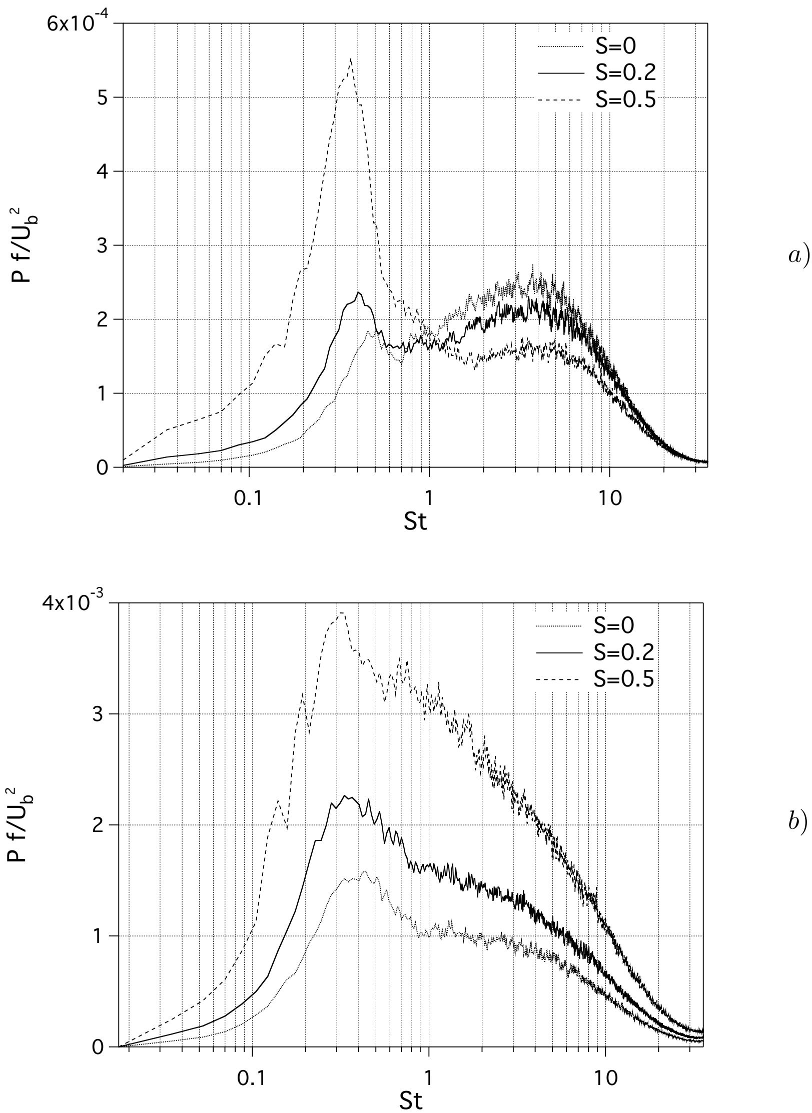

FIGURE 8.20. Spectra of v-component at centreline for Re=33500. a) x/D=2, b) x/D=6.

8.3. Instantaneous flow angle measurements

Free shear flows may show large instantaneous flow angles, i.e. the angle between the velocity vector and the streamwise direction, and in some cases even back flow. This is the case in for instance the outer region of jet flows. In the following we present some results to illustrate this and also give a comparison between the LDV and hot-wire techniques used in the present study.

To display the behaviour of the flow angle we plot the instantaneous measured points directly on the calibration region (see figure 8.21). As can be seen the calibration curve is limited to $\pm 40°$. The data in the figure are taken at r/R=0.335 for two swirl numbers (S=0 and 0.5) and it is possible to follow the evolution of the cloud of points for different downstream positions (x/D=0, 2, 6). In all the figures the same amount (1600 measured points) of experimental data is plotted. For x/D=0 and x/D=2, the swirl shifts the points towards a higher axial velocity and at the same time the azimuthal component gives a shift of the cloud from the zero-angle line. At x/D=6 an opposite effect on the axial component is observed, i.e. the axial velocity has decreased. Clearly, moving downstream, the cloud spreads and its covered area in the calibration curve is enlarged. With swirl the growth of this area becomes larger. In the case of x/D=6 it is possible to register some data points which lie outside the region limited by the calibration.

Figures 8.22 and 8.23 show the mean angle at the pipe outlet (x/D=0) measured with the X-probe and the LDV, respectively. The data are all for S=0.5, but for the three different Reynolds numbers. As can be seen there is only a small difference between the different Re as expected. It should be noted that the hot-wire measurements were corrected according to the procedure described in section 5.2.2.

In figure 8.24 the data from the two different techniques at Re=24000 are directly compared and it is seen that the agreement is nearly perfect. In this figure we also plotted the uncorrected hot-wire data. As expected the largest corrections occur in the outer part of the jet, however they are still fiarly small.

Figure 8.25 shows the mean and 99% interval of the instantaneous angle measured with the hot-wire. In the figures three groups of lines, marking different downstream positions, are plotted. The central curve of each group corresponds to the mean value of the flow angle as already shown in figures 8.22 and 8.23. The upper and lower curves display the region for which 99% of the data are located (i.e. at each side of these lines 0.5% of the data are found).

When moving downstream, the mean flow angle between the axial and azimuthal velocity components decreases. At the same time the angle interval is amplified especially in the outer radial positions. Moreover, from the figure itself it is possible to note that the probability density function is skewed since the upper and the lower curves are not equally distanced from the mean curve. Even if the mean values are relatively small, the lines of 99% interval can exceed the range of the calibration curve ($\pm 40°$) due to the large fluctuations present in the flow.

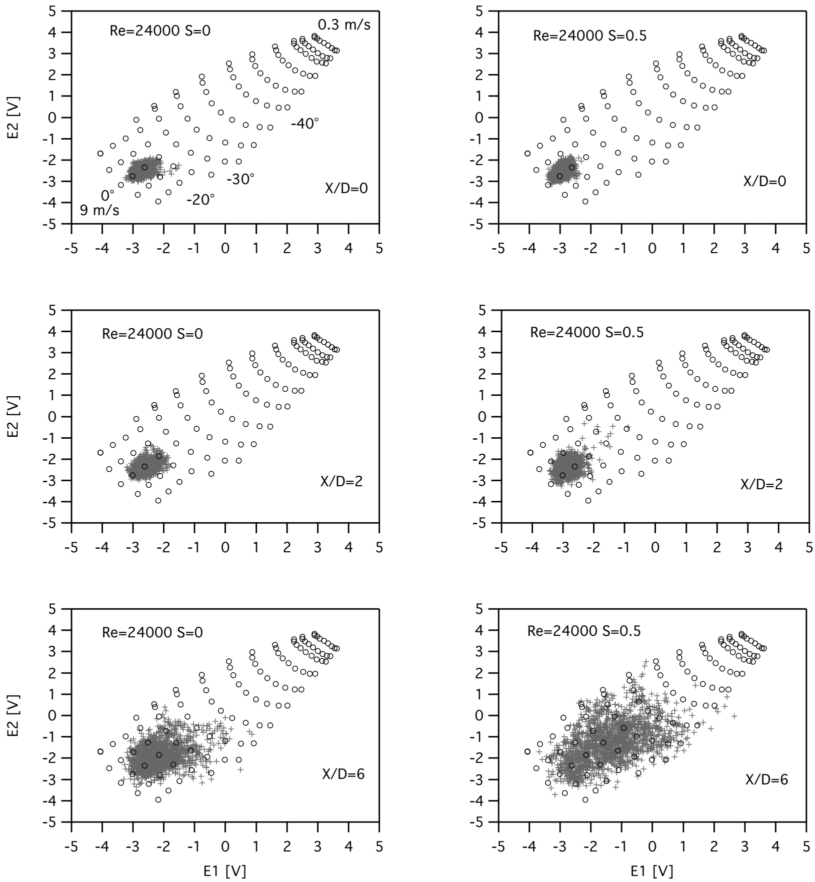

FIGURE 8.21. Hot-wire calibration region with instantaneous measurement data. The calibration is done wat 13 different velocities ranging from 0.3 m/s to 9 m/s and at different angles in 5° steps.

Finally it can be noted that at x/D=6 it seems that the mean flow angle in the central region changes sign. This observation leads to a more careful investigation of the jet in this region.

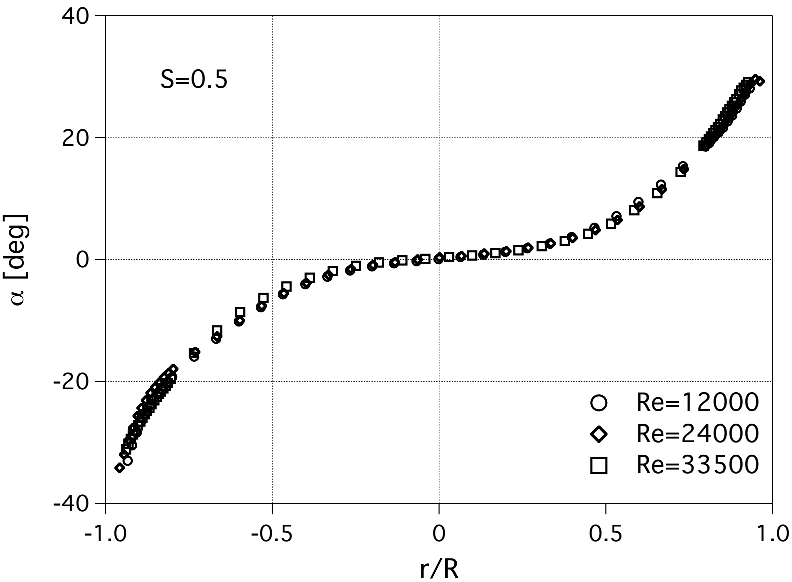

FIGURE 8.22. Flow angle between axial and azimuthal mean velocity components at the pipe exit measured with X-probe.

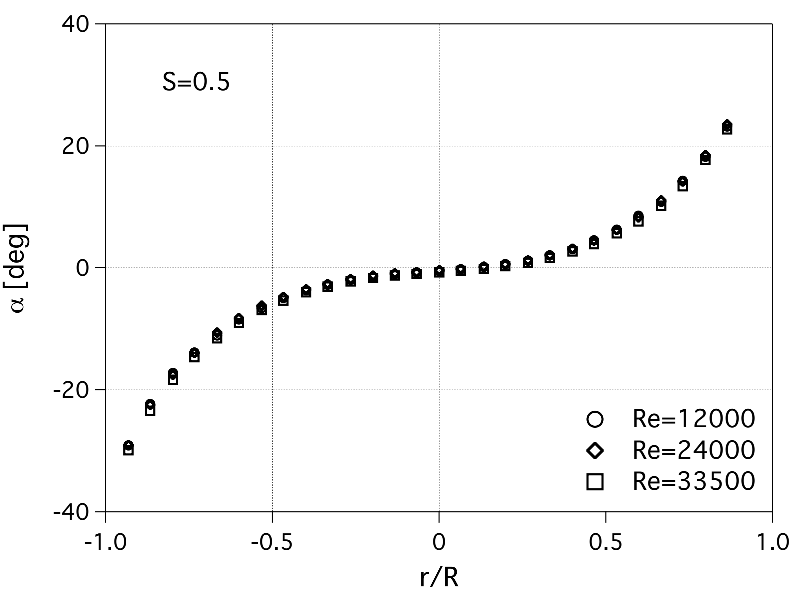

FIGURE 8.23. Flow angle between axial and azimuthal mean velocity components at the pipe exit measured with LDV.

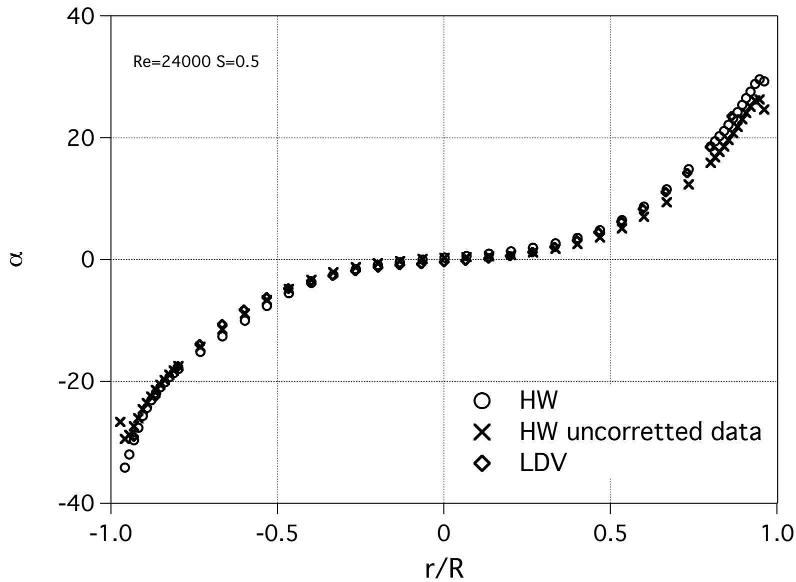

FIGURE 8.24. Comparison between the flow angles in figures 8.22 and 8.23 for Re=24000.

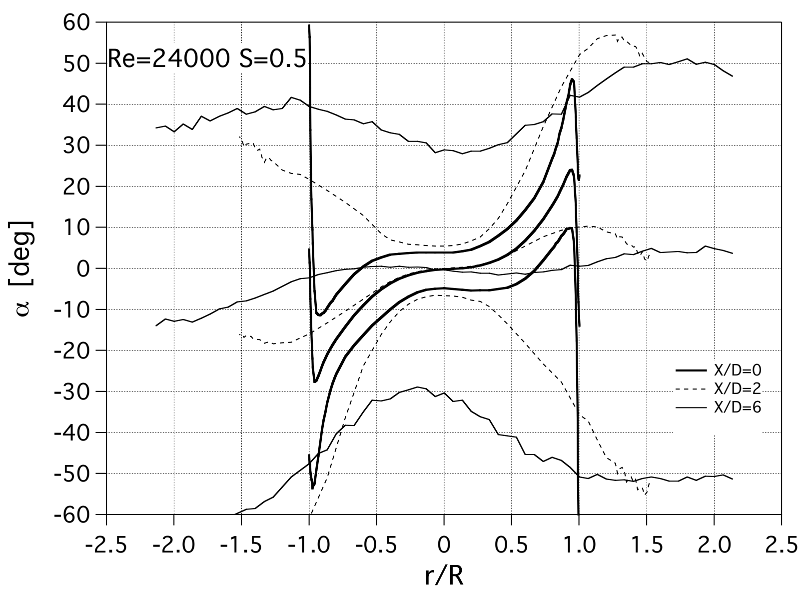

FIGURE 8.25. Mean and 99% interval for the angle between axial and azimuthal instantaneous velocity at Re=24000 S=0.5 measured with hot-wire anemometry for x/D=0, 2 and 6.

8.4. The counter rotating core of the swirling jet

Considering again the LDV data for the azimuthal velocity component shown in figure 8.3 we focus our attention on the central region of the jet. Figure 8.26 shows a close-up of the data already presented in figure 8.3 in the region under consideration. The black line is a polynomial fit of the data points at the pipe outlet which is very close to the parabola $(r/R)^2$. As can be noted the LDV data in this region lay on the curve until x/D=3 showing that the "parabolic" velocity profile is preserved in the central region. Further downstream, the azimuthal velocity starts to decrease. but at x/D=5 the velocity profile is still monotonic. However at x/D=6 the profiles reveals a change in the sign meaning that in average the jet, in the central region, rotates in a direction which is opposite to that imposed by the rotating pipe. Even in this case the lines for $6\leqslant x/D \leqslant 8$ are polynomial fit of the LDV data for visual aid.

The azimuthal velocity of the counter rotating core is fairly small, less than 1% of V/V_w, and it covers a region slightly smaller than the pipe diameter as indicated also by the hot wire data in figure 8.25. The counter rotating region starts between 5 and 6 diameters downstream the pipe outlet then it increases in magnitude and reaching a maximum between 6 and 8 diameters.

A parallel experiment not presented here shows that for higher Reynolds number and same swirl the start of the counter rotating core moves upstream.

Also the instantaneous DNS simulation in figure 8.27 displays the counter rotating core of the azimuthal velocity starting from a downstream position greater than x/D=5. In this case the counter rotation represents a much bigger quantity compared with the pipe wall velocity. The simulation is also able to catch the preservation of the "parabolic" profile in the central region of the jet close to the pipe outlet. Note also that the maximum of the velocity profile first moves towards the centre of the pipe and then, slowly, it moves outside. The same behaviour happens in the real jet (compare figure 8.3) but the process in the simulation is much slower since the expansion of the flow is ruled only by the diffusivity.

The DNS results illustrate that the reason for the formation of a counter rotating flow could be seen in the jet initial flow field that is the pipe flow since the equations for the pipe flow used to simulate the jet are already enough to explain the presence of a counter rotating core. We have already pointed out that the azimuthal-radial Reynolds stress acts in the direction opposite to the pipe rotation preventing, in the case of turbulent flow, to reach the solid body rotation (see eq. 2.17).

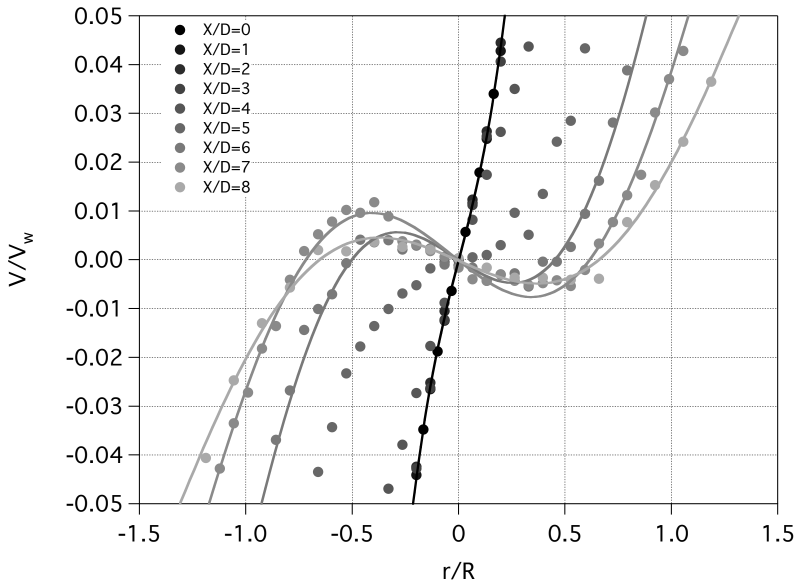

FIGURE 8.26. Close up of the azimuthal velocity in the core of the jet from figure 8.3.

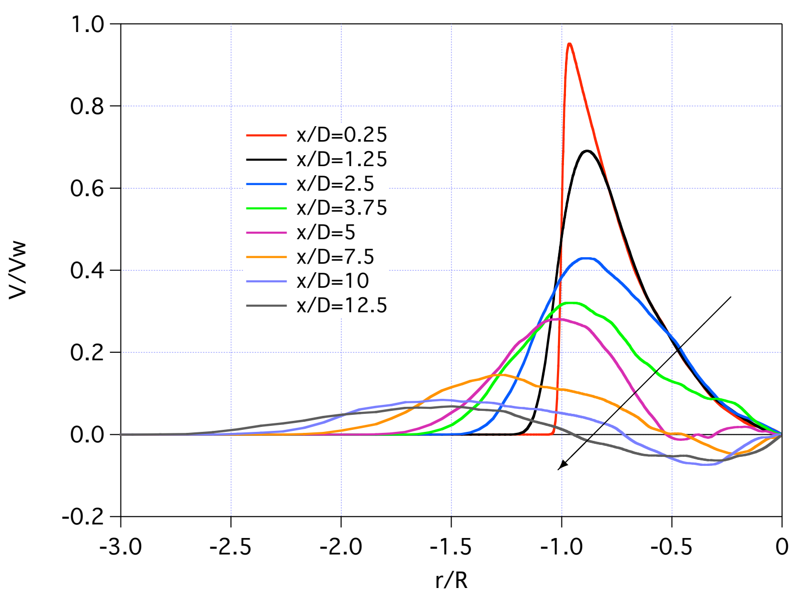

FIGURE 8.27. Instantaneous azimuthal velocity from DNS. The arrow points the direction of increasing x/D.

The evolution of the normalised azimuthal-radial Reynolds stress in the jet flow is plotted in figure 8.28. As already stated, the Reynolds stress is almost proportional to the radius in the pipe flow. The values in the figure are so normalised as shown in the pipe flow. As soon as the flow leaves the pipe the shear layer develops and the cross Reynolds stress increases. At x/D=1, while in the central region of the jet the values of the Reynolds stress are very small and close to what seen in the pipe flow, two high peaks cover the outermost parts. Then, moving downstream those peaks become broader and less intense, penetrating inside the jet. For $x/D \leqslant 4$ the peaks seems to be located at the same radial position, around r/R=1, then their position start to move going outwards in the radial direction. Note also that at x/D=4 the Reynolds stress reaches its highest value in the internal part of the jet. For larger x/D it starts to decay.

Figure 8.29 shows at the top the development of the azimuthal-radial Reynolds stress in the streamwise direction for fixed radial positions in the central part of the jet. The curves shows the mean values in the correspondent $|r/R|$ positions. The maximum is reached between 3 and 4 diameters downstream the pipe outlet for all the considered radial positions. In the bottom of the figure the mean azimuthal velocity are plotted for the same radial positions as in the top. The counter rotating core is barely seen at x/D=6 and 7.

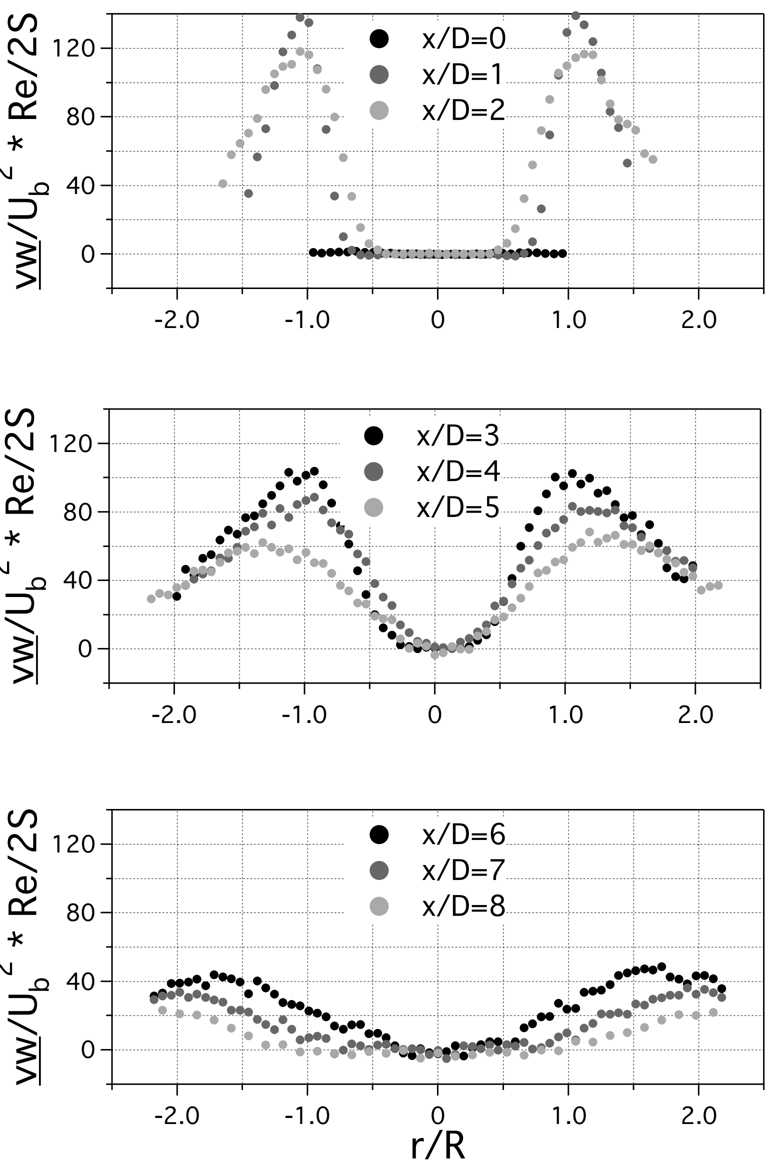

FIGURE 8.28. Normalised azimuthal-radial Reynolds stress in the jet, LDV data

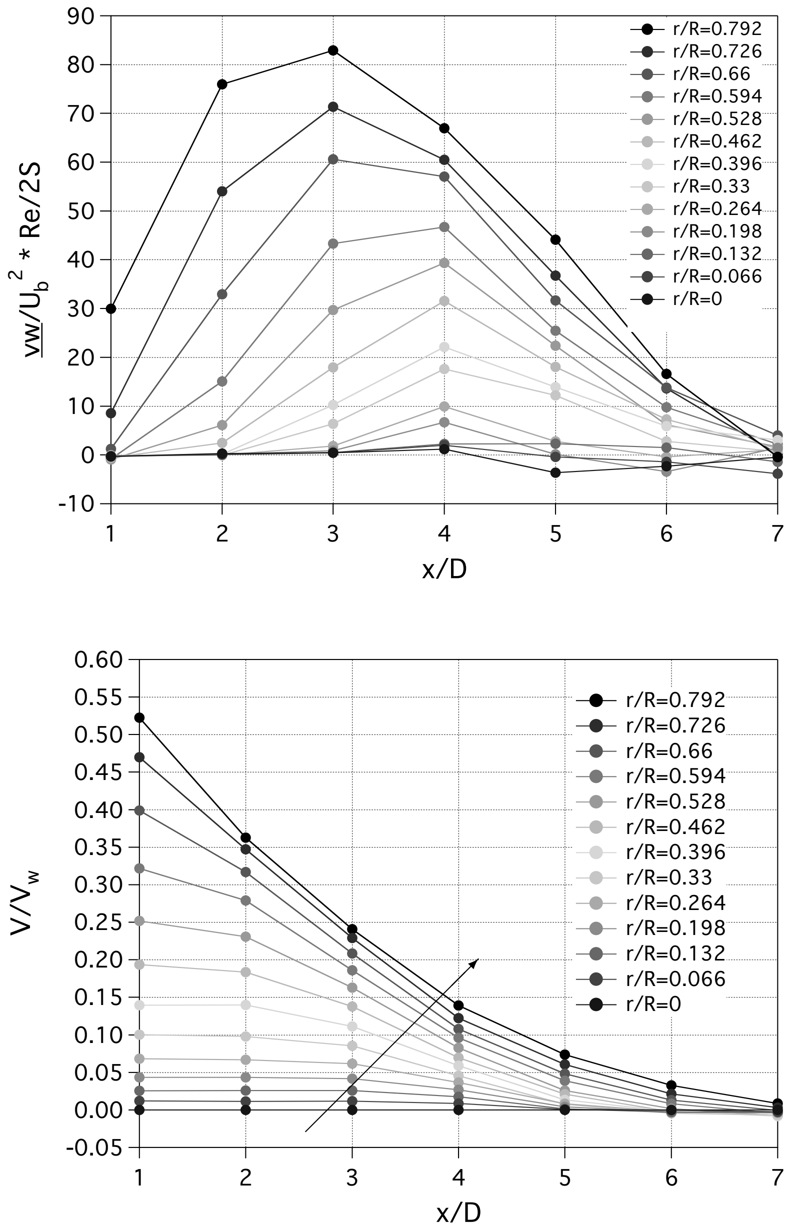

FIGURE 8.29. Evolution of the azimuthal-radial Reynolds stress (top) and of the mean azimuthal velocity (bottom) along fixed radial positions in the jet core. The arrow points the direction of increasing r/R.

8.4.1. *Stereoscoipic PIV measurements*

A stereoscopic PIV sytem has been used to further investigate the flow field in order to inspect the counter rotating core. For this reason, knowing the results from HW anemometry and LDV, it has been chosen to investigate the region around x/D=6 for Re=24000 at S=0.5. A first setup configuration has been utilised to cut the jet with the laser sheet perpendicular to its axis. The averaged velocity field of the cross section seen by the cameras has been presented in figure 8.30: the colour scale (not reported) is related to the absolute velocity of the vector, the sum of the three components. The picture represents the jet flow running from the pipe towards the reader: at the centreline of the jet the vectors have mainly an axial velocity component and so they are directed normal to the plane of the cross section. Moving radially the azimuthal and the radial components grow and add to the axial velocity making the vector more visible on the plane. Basically, from this point of view, it is possible to read only the components in the cross plane. The outermost part of the figure easily shows the clockwise rotation of the jet imposed by the pipe. On the other hand, focusing the attention in the central region of the jet is clear that the vectors are in the opposite direction. Following a horizontal line from the centre of the jet and moving radially to the left it is possible to note that the vectors, initially too small and close to zero to be seen, start to point to the upper right corner of the figure that means they have a positive azimuthal and radial velocity component. Then it starts to tilt until the vector is practically horizontal that means it has only a radial component while the azimuthal one is zero. The tilting of the vector then continues and the azimuthal component changes sign to follow the rotation of the pipe. The behaviour just described certify the counter rotating core of the swirling jet. A similar scenario is present in almost all the radial directions.

Starting from the three dimensional vector field we now consider only the axial component. The contour plot is presented in figure 8.31. The velocity reported is in meter per second whilst the dimension of the flow field is in millimetre. As can be seen the cameras cover roughly the space of two diameters of the pipe in the horizontal direction, something less in the vertical one. The contour lines are fairly circular showing the symmetry of the flow especially in the central part of the jet. In evaluating the stereo PIV images it has to be taken into account that, although the average is taken over all the 3072 collected images, due to the highly turbulent nature of the flow, it is not possible to calculate a vector in each position seen by the cameras in all the images. The behaviour of the jet does not allow the smoke particles to fill all the image field since air without seeding particles is captured from the surroundings (only the air passing through the pipe is seeded with smoke) and the jet itself moves so that, basically, only in the centre of the image is always possible to calculate the vectors. This is one of the reasons why the statistics is more accurate in the centre than in the outermost parts of the flow field.

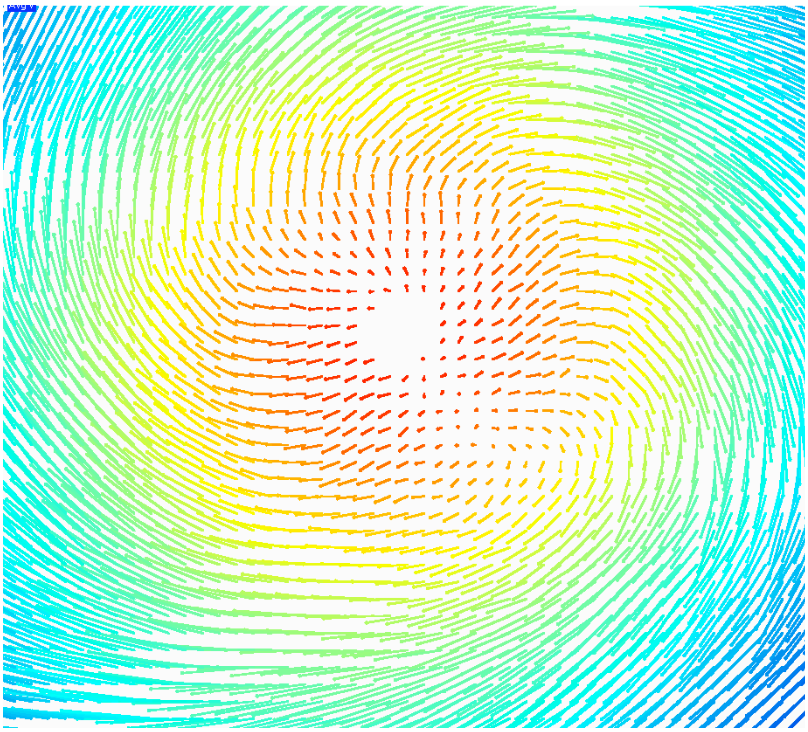

FIGURE 8.30. Close-up of the mean velocity vector field in the central region of the jet at x/D=6, stereo PIV.

From the concentric contour lines it is possible to obtain the fluid dynamic centre of the axial velocity component that results to be very close to the geometrical centre of the jet. When the centre is obtained an axial velocity profile can be calculated for each radial direction. In figure 8.32 the mean profile calculate over all the radial direction is shown. Beside the lack of vectors as already stated, since the images is not circular, the outermost radial positions ($r/R \gtrsim 1.7$) do not contain the same number of samples thus the statistics is not so accurate as in the inner radial positions. In the same picture also the LDV data are presented. The agreement between the two experiments is almost perfect along the radius, there is just a small gap close to the centreline where the stereo PIV data have slightly higher values that, anyway, represent a disarrangement of just a few percent. The reason of this gap can be found in the possible not perfect arrangement of the LDV system and the PIV system that results to be particularly sensitive in the region with high velocity or even in a small difference in the Reynolds numbers used during the two experiments.

The same analysis can be applied to the azimuthal velocity component. Taking into consideration the fluid dynamic centre of the axial velocity, the vector field of figure 8.30 has been transformed from a cartesian to a cylindrical coordinate system even if the dynamic fluid centre for the azimuthal velocity component may not be coincident with that of the streamwise velocity. In figure 8.33 the resulting contour plot is displayed. As convention, in the picture the direction of the pipe rotation has been chosen as positive. In this case the contour lines do not show a perfect symmetric path but it is still possible to distinguish a region with negative azimuthal velocity in the centre of the image (see the velocity scale). Again, considering all the radial directions departing from the stated centre, we get a mean profile displayed in figure 8.34.

In the same picture there are also the LDV data to compare with. The two profiles collapse at least for $r/R \leqslant 1.5$ where the PIV data have, also in this case, slightly higher values. Note the region of the counter rotating core in $0 \leqslant r/R \lesssim 0.4$. The LDV shows a maximum that is somewhat higher than the maximum of the PIV and also positioned at a larger radial position. Due to the presence of not seeded air entrapped by the jet, the LDV system is not able to measure with a good statistics in this outermost region. The quantity of seeding particles for the LDV is much less compared with the amount used in the PIV system in order to avoid to have too many particles at the same time in the measuring volume and to have problems with overloading of the photo detector. This means that in the outermost radial region only the smoke particles that show high velocity can be detected while the entrained flow, not seeded and with lower velocity does not generate any signal in the LDV system and so is not taken in account. This could explain the divergence of the two measurements and the scattered data for the LDV. The same is true also for the axial velocity component of course but the problem does not seem to appear there: actually the axial velocity is much higher compared with the azimuthal component and the scattering of the data is so not appreciable. What said about the statistics for the axial component with the PIV is still valid also here for the azimuthal velocity.

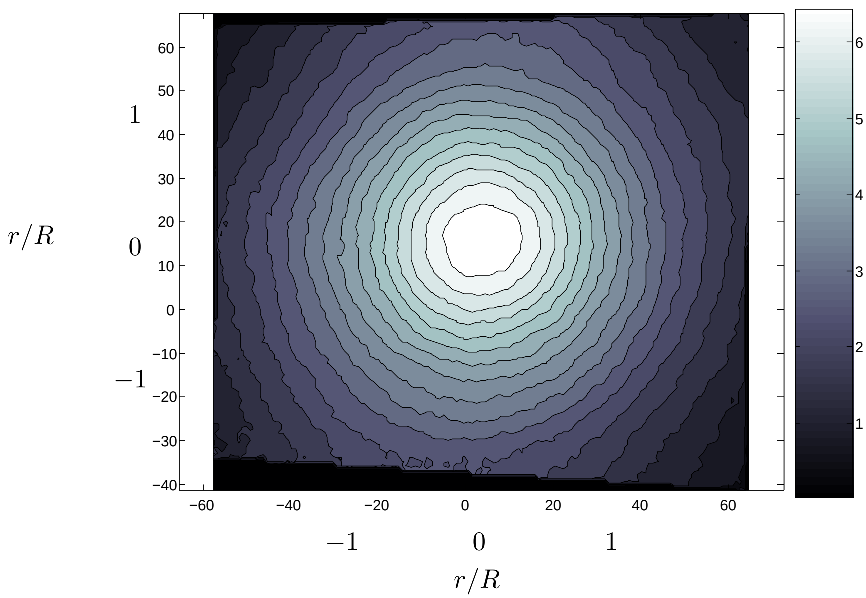

FIGURE 8.31. Mean axial velocity at x/D=6, stereo PIV. The dimension are in mm and the scale of velocity is in m/s.

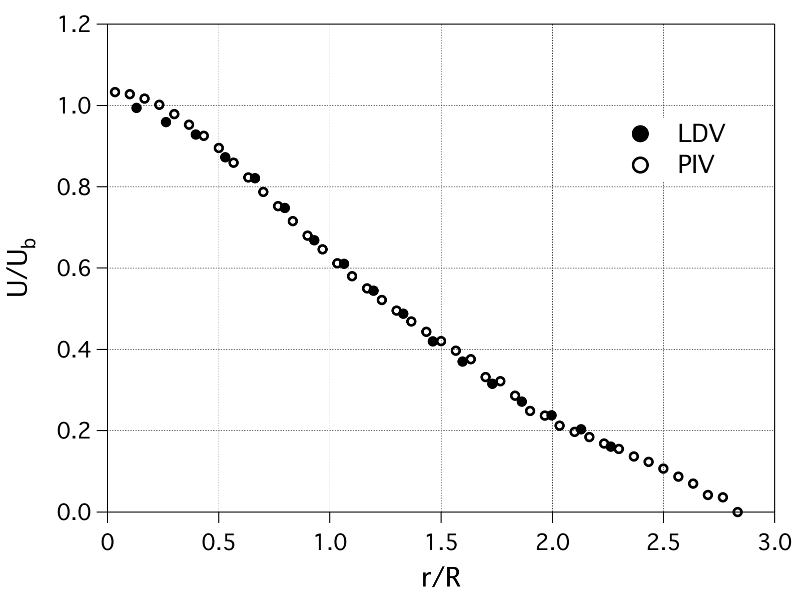

FIGURE 8.32. Mean axial velocity at x/D=6. Comparison between PIV and LDV data.

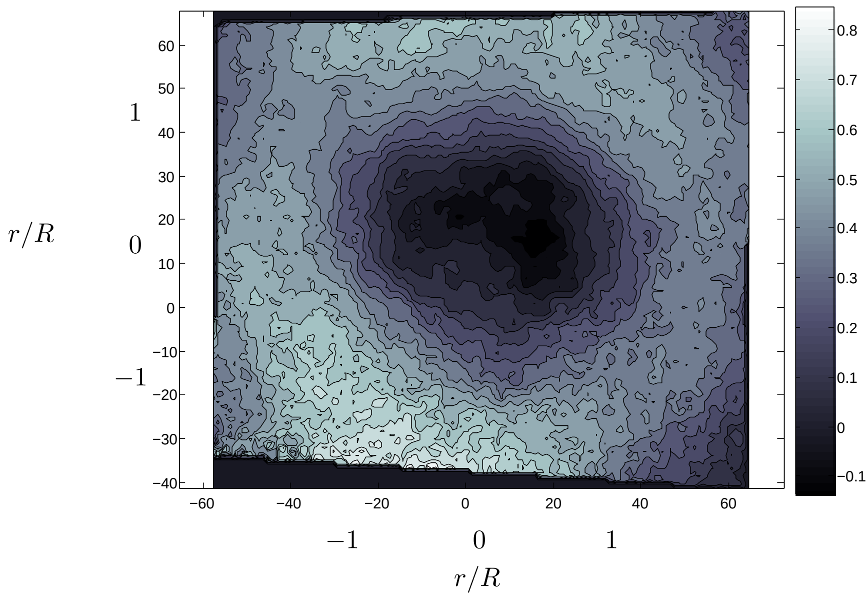

FIGURE 8.33. Mean azimuthal velocity at x/D=6, stereo PIV. The dimension are in mm and the scale of velocity is in m/s.

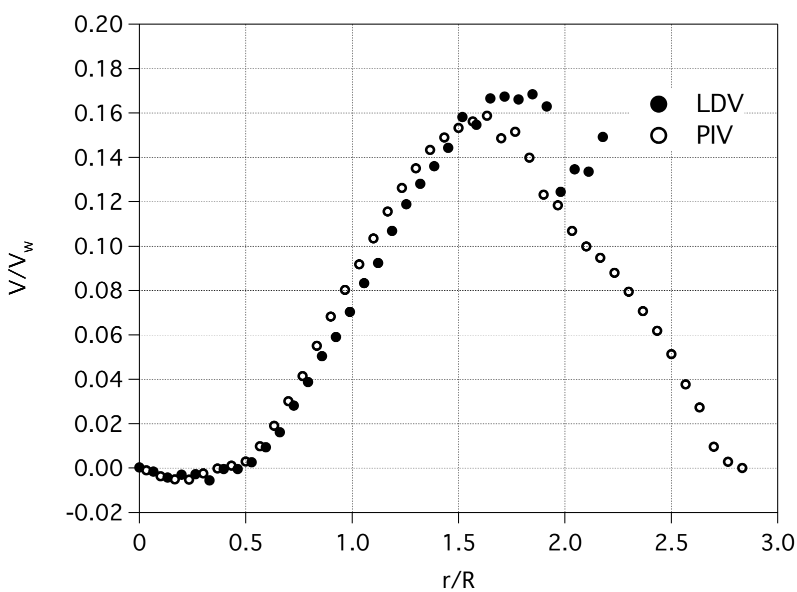

FIGURE 8.34. Mean azimuthal velocity at x/D=6. Comparison between PIV and LDV data.

The stereoscopic PIV technique has also been used to investigate the counter rotating region in a different set up. The laser sheet has been positioned to cut the jet along its axis as shown already in figure 5.7 with the cameras in the forward-forward configuration. The centres of the images in the two cameras are set at x/D ≈6. The field covered by both the images is about 5.1$\leqslant x/D \leqslant$6.85 and -1.45$\leqslant r/R \leqslant$1.45: this is sufficient to catch the formation of the counter rotating core.

Also this experiment is done at at a Reynolds number of about 24000 and at S ≈0.5. The same number of images, 3072, covering 123 seconds has been used for the statistics as in the previously presented analysis. The position x/D=6 corresponds to about −11 mm on the horizontal axis in figure 8.35 and 8.36 while the axis of symmetry is at 10.5 mm on the vertical axis. Also for this experiment is valid what already discussed about the different accuracy of the statistics for different radial positions.

The contour lines for the axial velocity are plotted in figure 8.35. The picture is obtained by taking the mean of the part of plane above and the side of plane below the axis of symmetry and then mirroring the result. The scale shows negative velocities since the flow run from the right side to the left one while the axis in the cartesian coordinate of the cameras points in the opposite direction. It is clearly detected the decay of the axial velocity, faster at the centreline, slower at larger $|r/R|$: the contour lines seem to be almost parallel at $|r/R|$ ≈1 indicating a constant axial velocity. This was already pointed out discussing figure 8.1 where a common crossing point appears at about $|r/R|$ ≈1.

Figure 8.36 shows the azimuthal velocity component. Also here the velocity profiles have been averaged and then mirrored. A positive velocity means the flow is directed outside the plane of the image, towards the reader, a negative velocity states the vectors are pointed in the opposite direction, inside the page. At the centreline the azimuthal velocity is, obviously, close to zero. Moving from the right side to the left it is possible to note as the azimuthal velocity decays, the contour lines spread and the zero level becomes larger and larger. At x/D ≈5.5 (i.e. ≈ 20 mm in the horizontal scale) a first anomaly is encountered: a region with negative velocity is present in the plane above the axis of symmetry where the velocities are supposed to be positive. The opposite of course happens in the lower part of the plane. This is the first sign of the formation of the counter rotating core. Then the change of sign in the azimuthal velocity propagates in the axial direction, becoming more intense and covering a larger radial region. Note that at the centreline the velocity is everywhere zero. What seen in the LDV experiment is confirmed by the pictures from the PIV: the counter rotating core is formed between x/D=5 and x/D=6 and then it increases in intensity. The maximum of the amplitude of the counter rotating core seems to be reached at x/D ≈6.6.

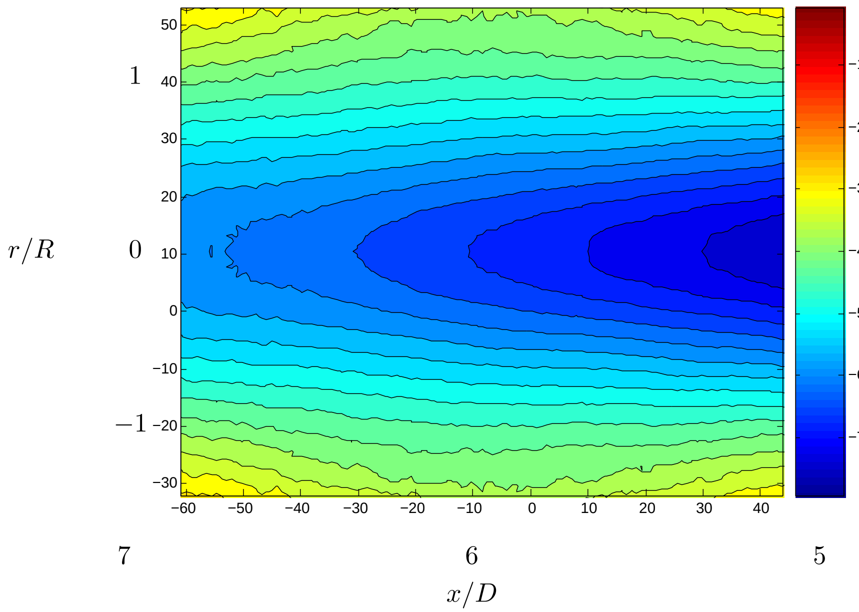

FIGURE 8.35. Mean axial velocity between x/D=5 and 7, stereo PIV. The dimension are in mm and the scale of velocity is in m/s.

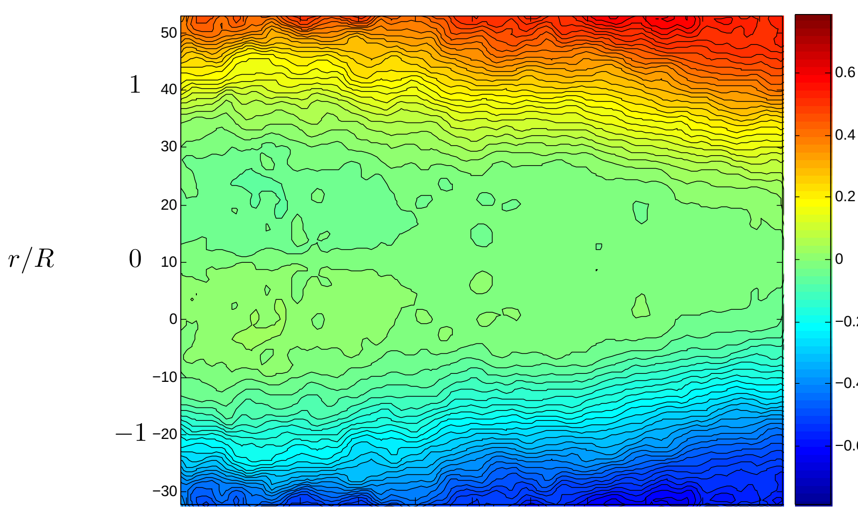

FIGURE 8.36. Mean azimuthal velocity between x/D=5 and 7, stereo PIV. The dimension are in mm and the scale of velocity is in m/s.

8.4.2. *Structures in the counter rotating core region obtained with PIV*

By analysing the time and space resolved data from the stereoscopic PIV it is possible to capture the evolution of the flow and its structures.

The visualisation at the cross section x/D=6 allows the analysis of the structure in the azimuthal-radial plane of the flow. The pictures in figure 8.37 compare the swirling jet S=0.5, on the right side, with the non swirling jet S=0, on the left side. The colour of the vectors denote the absolute velocity. The images are shown at a frequency f=75Hz to follow the motion of the flow, how it evolves in time, which structures appear and how they are organised. Although these are only a few snapshots long sequences are available and the discussion below is based on viewing the flow for much longer times.

The first impression is that the swirling jet is subject to more violent and larger scale phenomena that involve all the visualised flow field. From the comparison between the mean axial velocity at x/D=6 for the swirling and the non-swirling jet as shown in figure 8.1 it is clear that, close to the axis, the distribution of velocity is much higher in the second case. The instantaneous pictures help to understand the reason of this behaviour: although the range of the absolute velocity is practically identical in both the cases, the distribution is evidently different. The non-swirling jet has always a concentric distribution of velocities, with the highest values in its central region and decreasing velocities moving radially towards the external part of it. On the contrary the swirling jet presents a more complex distribution in the flow field. It is not anymore possible to see a concentric distribution of the velocity since the centre of the jet itself is not stable as in the previous case: it moves shifted and stretched by strong and fast radial motions that looks like eruptions of flow towards the periphery of the jet. This explains also the higher averaged velocity at greater radial positions, the larger spreading of the jet and also its higher turbulence intensity compared with the non-swirling case.

The sequence of images from the side point of view in figure 8.38 shows the development of the azimuthal, on the left, and the absolute velocity, on the right, along the axial section of the swirling jet in the region of the counter rotating core. The colour for the azimuthal component means opposite directions of the flow, positive towards the reader, negative inside the page. Here the images are shown at a frequency f=150Hz.

The flow is organised in consecutive, packed structures having opposite azimuthal direction and that tend to assume an arched shape. This shape is explained as an effect of the shear flow: the jet is faster in the centre and slower in the upper and lower region as it is possible to follow in the images on the right side. So, the central part of these structures moves faster compared to the tails producing the visualised stretched form. Furthermore, from the absolute velocity it is possible to recognise a wavy motion of the jet that confirm the variation of the position of the centre as already noted in the cross-section visualisation.

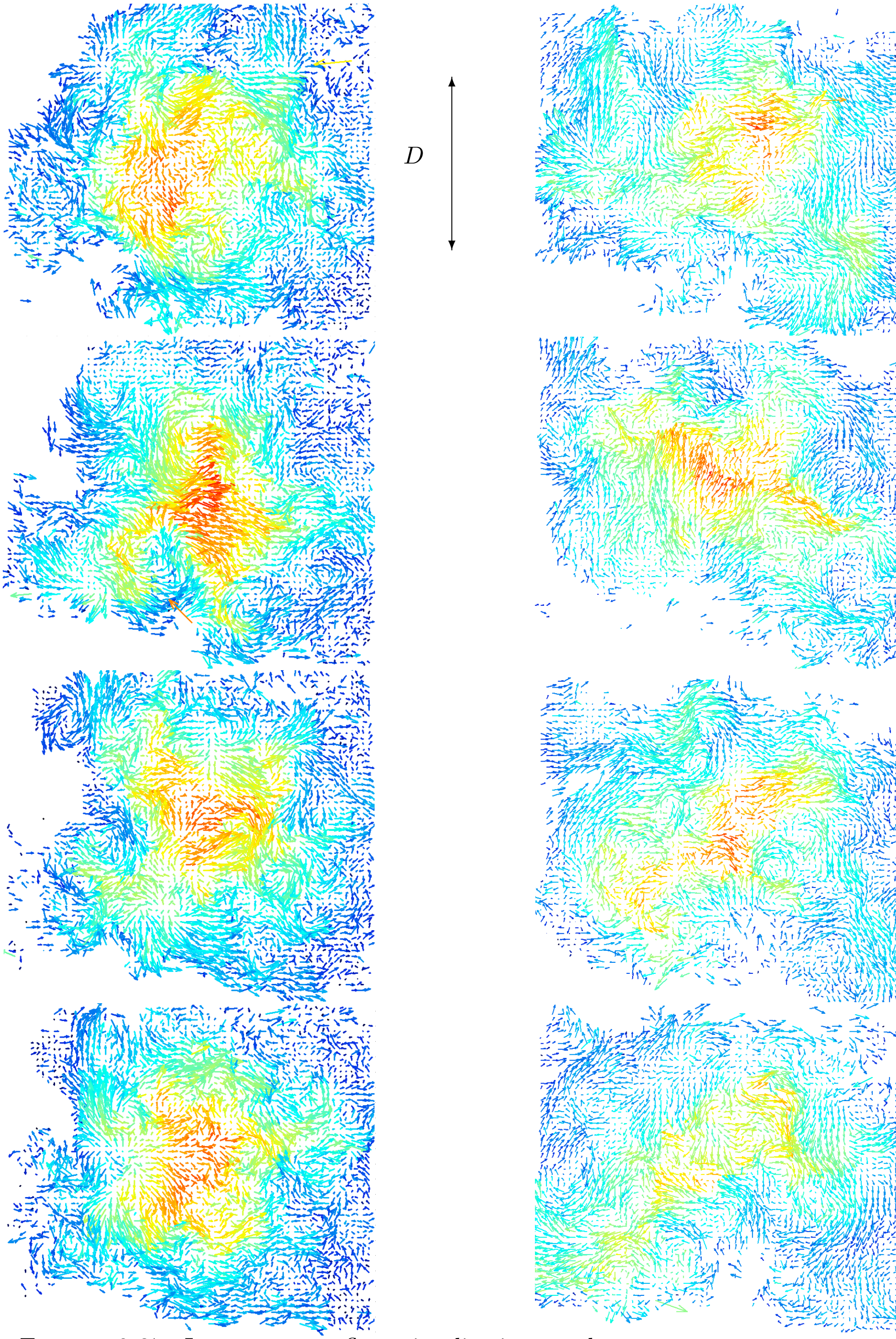

FIGURE 8.37. Instantaneous flow visualisation at the cross section x/D=6 at S=0 (left) and S=0.5 (right), stereo PIV. The dimension of the pipe diameter is shown by the arrow.

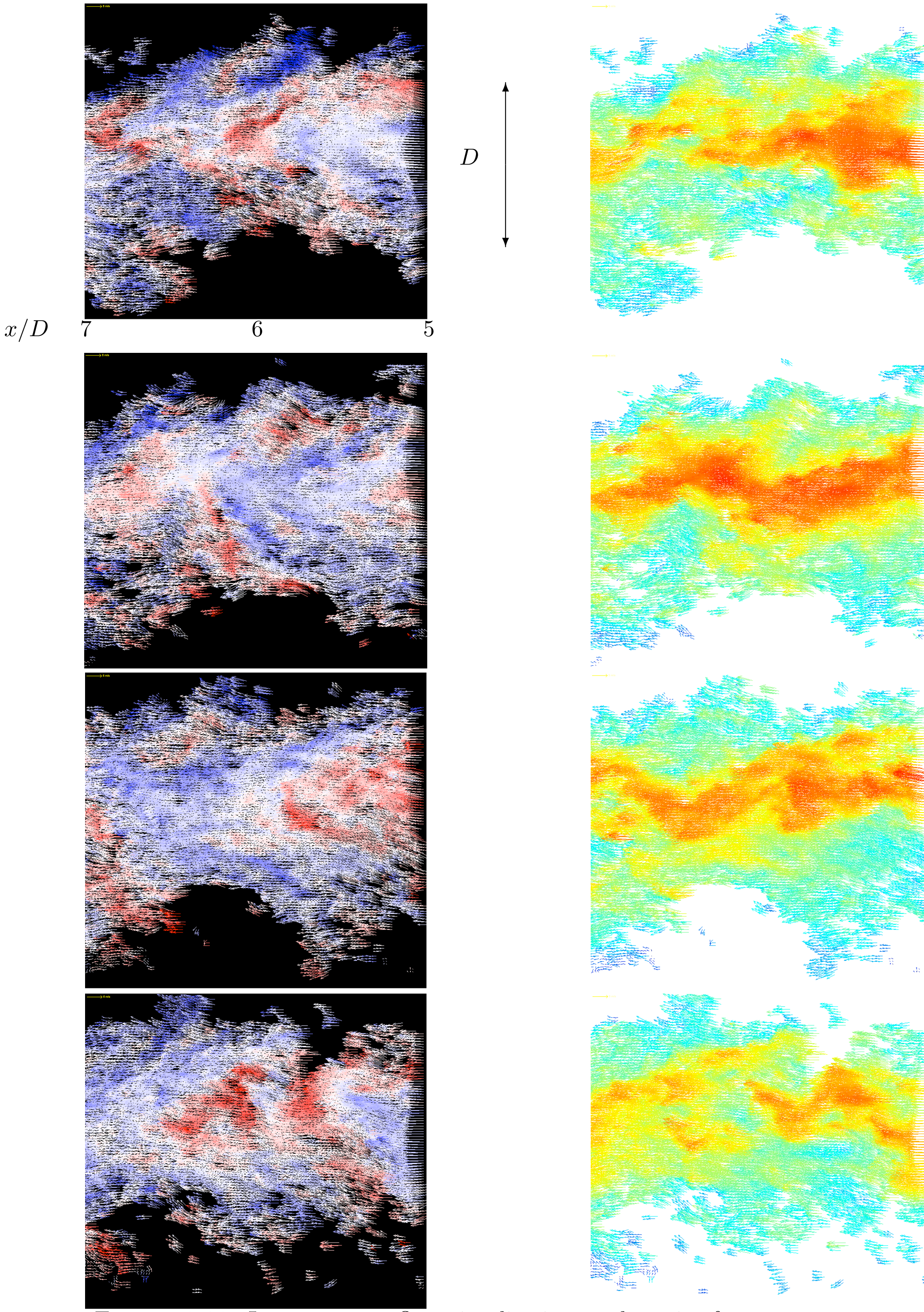

FIGURE 8.38. Instantaneous flow visualisation at the axis of the jet 5< x/D <7 of the azimuthal (left) and the total velocity (right) at S=0.5, stereo PIV. The dimension of the pipe diameter is shown by the arrow.

CHAPTER 9

Summary, discussion and conclusions

The experimental work has been aimed towards the investigation of rotating flows, both turbulent rotating pipe flow as well as swirling jet flow. A new experimental set-up has been designed which has been shown to give a fully developed turbulent pipe flow. Particular attention has been paid during the design and the construction of the set-up in order to have a high quality flow with a low level of disturbances coming from the upstream conditions or vibrations of the pipe. For the jet experiments this is highly valuable since the exit conditions can be viewed as independent of the geometry which would not be the case using swirl generators or adding secondary injection flows. The jet was studied in the near exit region, up to 10 diameters from the exit plane.

The flow field has been investigated using hot-wire anemometry, LDV and stereo PIV and also through a time evolving direct numerical simulation. In cases where comparisons have been possible there is a good correspondence between all the methods. It is worthwhile to point out that the present measurements using the stereoscopic PIV has shown the potential of the PIV system to measure all three velocity components simultaneously, a very useful feature in complex three dimensional flows.

The parameter space for the experiments is defined by the Reynolds number and the swirl number. For swirl numbers up to 0.5, the Reynolds number has been varied between 12000 and 33500, whereas the pipe flow has been studied for swirl numbers up to 1.5 at a Re=12000. In the DNS the Reynolds number has been fixed at 5000, for the pipe, and 10000 for the jet, though also the laminar flow has been evaluated and not included in this work.

In the following some of the findings of the present work are highlighted and two issues connected to the influence of the cross stream Reynolds stress are discussed in more detail.

Turbulent pipe flow - summary

- The change of the axial profile towards a parabolic shape was verified when rotation is applied.

- Accurate measurements of the azimuthal profile in a turbulent flow shows a close to parabolic shape independent of Re for S >0. The profile becomes linear with the radius in the region close to the pipe wall as confirmed by the DNS simulation.

- An expression for the $\overline{vw}$ Reynolds stress term has been derived under the assumption that the azimuthal velocity is parabolic. It is shown to vary linearly with r. Experiments and simulation confirm the trend for a large portion of the radius of the pipe.

- The mean flow data were compared with recent theoretical scaling results of Oberlack (1999). The experimental results seem to follow the theoretical results closely, while the DNS strongly support them.

Turbulent pipe flow - discussion

It is well known that system rotation can strongly affect a shear flow, i.e. in the rotating system the fluid can be viewed to be affected by a Coriolis force. In the case of an axially rotating pipe (or jet) flow the Coriolis force will always be in cross stream plane since

$$\mathbf{f}_{cor} = -2\mathbf{\Omega} \times \mathbf{u}$$

Tritton & Davies (1985) used a displaced particle argument to describe the effect of rotation on the stability of a shear flow (i.e. a shear flow undergoing spanwise rotation). With this reasoning they were able to show both the destabilizing and stabilizing effects of such a system rotation.

One of the intriguing observations for the rotating pipe flow is the fact that the azimuthal velocity lags behind a velocity distribution corresponding to solid body rotation. For the pipe flow it can be shown that this implies that $\overline{vw}$ is larger than 0 (see eq. 7.1) which is contrary to what one would expect through a simple displaced particle argument. However in the rotating system it is natural to see whether the the Coriolis force may play a role.

If we assume that the fluid is rotating as a solid body a fluid element at certain radius r would have the angular velocity Ωr. If this fluid particle was decelerated (i.e. would have a negative velocity with respect to fluid particles in solid body rotation) the fluid particle would be affected by a Coriolis force towards the centre of rotation and thereby start to move towards the centre. On the other hand if the fluid particle would be accelerated with respect to the solid body rotation the Coriolis force would be directed outwards and the fluid particle would start to move outwards. Both these scenarios would give rise to a that the velocity disturbances v and w either both are positive or negative and hence the correlation $\overline{vw}$ would be positive. On the other hand, if assume that a fluid element is displaced in the radial direction (i.e. $w > 0$) the Coriolis force would be directed in such a way that its angular velocity would decrease. The fluid particle would hence obtain an angular velocity smaller than that at the position to which it was displaced, thus $v < 0$. For such a movement $\overline{vw}$ would be smaller than zero. Hence this analysis cannot in itself explain the observed behaviour of $\overline{vw}$.

An interesting observation is that the azimuthal velocity distribution seems to be parabolic for all S and Re in the present study but also for other studies with S and Re outside the present range. We have shown that a parabolic azimuthal velocity profile corresponds to a linear distribution of $\overline{vw}$ according to the expression

$$\frac{\overline{vw}}{U_b^2} = \frac{2S}{Re}\frac{r}{R}$$

If we instead write the expression in the form of the correlation (a_{vw}) between v and w defined as

$$a_{vw} = \frac{\overline{vw}}{v_{rms}w_{rms}}$$

we obtain

$$\frac{\overline{vw}}{U_b^2} = a_{vw}\frac{v_{rms}w_{rms}}{U_b^2} = \frac{2S}{Re}\frac{r}{R}$$

We have shown that v_{rms}/U_b and w_{rms}/U_b also are fairly independent of Re and S and of the order of 0.05 throughout the pipe (see figures 7.11 and 7.12). This means that when Re increases a_{vw} must decrease. On the other hand, with increasing S we find that a_{vw} will increase. For $S = 0.5$ and $Re = 10000$, which are representative values in the present study, we obtain a correlation coefficient that roughly varies in the interval 0 to 0.04 in the pipe, i.e. a very small correlation (compare for instance with a_{uw} which is of the order of -0.4 across the most part of the pipe). It is interesting that, despite its smallness, it is this correlation between v and w that makes the azimuthal velocity distribution deviate from the one of solid body rotation.

In an earlier work the positive value of $\overline{vw}$ was explained with a displaced particle argument taking the Coriolis force into account (Facciolo & Alfredsson (2004)). Unfortunately that analysis was not correct and in view of what is said above it is clear that an inviscid analysis is inadequate to explain the behaviour of $\overline{vw}$. In the equation for the Reynolds stress itself (see Appendix A) it is not clear how the production terms will affect $\overline{vw}$, however it is seen that the rotation influences $\overline{vw}$ through the term $S(\overline{vv} - \overline{ww})$, showing a delicate balance between the cross stream Reynolds stresses. Wallin & Johansson (2000) modelled the $\overline{vw}$ and also showed that this term needed careful modelling in order to provide correct results for the azimuthal mean velocity.

Swirling jet flow - summary

- All three velocity components have been measured in the near field of a swirling jet with different techniques. These data constitute a well defined data base for a complex flow field, ideal for comparisons with numerical modeling attempts.

- Flow entrainment measurements show that the entrainment increases with rotation as compared with the non-rotation case, since rotation makes the potential core break down faster. The entrainment decreases for increasing Reynolds number due to the smaller size of the structures in the shear layer for higher Reynolds.

- An interesting result is that the azimuthal velocity changes sign in the core of the jet at $x/D > 5$ for the investigated Reynolds number range. This is observed with hot-wire, LDV, stereo PIV measurements and DNS simulation.

- The time resolved PIV measurements shows interesting differences between the the non-swirling and swirling jets with regard to large scale structures inside the jet. Future work needs to be done in order to characterize these structures.

Swirling jet flow - discussion

There are many interesting features of the swirling jet, for instance the increased entrainment as compared to the non-rotating case and the vortex breakdown phenomenon. However here we will restrict the discussion to the observation that the jet actually becomes counter rotating at some distance downstream the outlet of the rotating pipe.

It was shown in chapter 2 that in the pipe flow geometry the Navier-Stokes equation in the azimuthal direction (eq. 2.8) became significantly simplified since several of the convective terms are identically zero and the equation reduces to a balance between the viscous term and the term containing the Reynolds stress $\overline{vw}$. In the jet on the other hand the viscous term becomes negligible and the Reynolds stress term instead is balanced by the convective terms. We also know that $\overline{vw}$ is much larger in the jet than in the pipe (see figure 8.28). We may hence write

$$U\frac{\partial V}{\partial x} + W\frac{\partial V}{\partial r} + \frac{VW}{r} + \frac{\partial \overline{uv}}{\partial x} + \frac{1}{r^2}\frac{\partial}{\partial r}\left(r^2\overline{vw}\right) = 0 \qquad (9.1)$$

By now multiplying with r^2 and integrating from 0 to r we obtain

$$r^2\overline{vw} = -\int_0^r r^2\left(U\frac{\partial V}{\partial x} + W\frac{\partial V}{\partial r} + \frac{VW}{r} + \frac{\partial \overline{uv}}{\partial x}\right)dr \qquad (9.2)$$

which also after using the continuity equation can be written

$$r^2\overline{vw} = -\frac{\partial}{\partial x}\int_0^r r^2(UV + \overline{uv})dr - \int_0^r r^2\left(\frac{\partial}{\partial r}VW + \frac{2VW}{r}\right)dr \qquad (9.3)$$

Hence the azimuthal velocity V is determined by several factors, the cross stream Reynolds stress $\overline{vw}$, the change in the downstream variation of U (the change in $\overline{uv}$ can probably be neglected) and the variation of W in the radial direction. By assuming that V and W both vary linearly with r near $r = 0$ the second integral in eq. (9.3) can easily be calculated and becomes equal to r^2VW, hence if the balance was only between the left hand side and this term we would obtain

$$\overline{vw} = -VW$$

It is seen that a positive $\overline{vw}$ would give VW negative, i.e. V has to be negative as in the counter rotating core. Using the measured data at x/D=6 (from figures 8.4, 8.26 and 8.28, assuming $V, W \sim r$ and $\overline{vw} \sim r^2$) to determine these quantities near $r = 0$ we find that the two terms are of the same order, although the LHS is about twice as large. However the first term on the may make up for the difference although it has not been possible to estiamte it accurately. The expression above is clearly inadequate close to the jet exit where V is positive, however in that case the first term on the RHS will be positive and may balance $\overline{vw}$.

In order to verify the analysis above accurate data are necessary and it would be very useful to have a direct numerical simulation of a spatially developing swirling jet. It should be noted however that the behaviour discussed here is not only restricted to a swirling jet emanating from a pipe flow but may also be valid for swirling jets in general.

Concluding remarks

It is clear that the axially rotating pipe flow and the swirling jet both are interesting and complex flow situations. At present we do not have full understanding of these flows and it would probably be worthwhile to study the flow structures in more detail, especially for the jet flow. With the time resolved stereoscopic PIV-system such measurements are possible and would certainly increase our understanding of the complex flow processes leading to increased entrainment and the counter rotating core. It would also be interesting to investigate whether the counter rotating core has an influence on vortex breakdown.

Acknowledgements

This research has been sponsored by the Swedish Energy Agency (STEM) and this support is gratefully acknowledged. The PIV system was acquired with funding from Knut and Alice Wallenberg foundation which is also gratefully acknowledged.

First of all I would like to thank my supervisor Prof. Henrik Alfredsson for his guidance and support in following my ideas in the research. His knowledge and suggestions helped me to progress in the fluid-dynamics research.

I would not know much about simulations if it was not for Prof. Paolo Orlandi who assisted me in the Eternal City.

Dr. Nils Tillmark is acknowledged for his help and taking care of me in the early stages of my PhD studies and Prof. Alessandro Talamelli for his assistance and discussions of the work.

I also want to thank Prof. Bengt Sundén who coordinated the larger project in which this work is a part and the groups working at Lund Institute of Technology for their collaboration.

A special thank to Marcus Gällstedt and Ulf Landén for their many high quality works in the workshop.

I am very thankful towards my friends Davide and Marco for being an important support during all my years in Sweden.

Finally I would like to thank the professors and colleagues at KTH Mekanik who create a pleasant and friendly environment. Special thanks to Dr. Fredrik Lundell and Dr. Luca Brandt for the advises and the helpful discussions.

Of course I can not forget all the friends, the old ones and the new ones, who have been with me during all this time.

To the Isacson family which adopted me like a son, I thank you from the bottom of my heart.

Un sentito ringraziamento alla mia famiglia che mi é sempre stata vicina in ogni occasione.

APPENDIX A

For completeness the equations for the normal Reynolds stresses eqs. A.1, A.2 and A.3 as well as the cross Reynolds stresses, eqs. A.4, A.5 and A.6 are given here in a rotating cylindrical coordinate system. In these equations overbar means an ensemble average.

$$\begin{aligned}\frac{\partial\overline{uu}}{\partial t} &= -\frac{1}{r}\frac{\partial r\overline{wuu}}{\partial r} - 2\overline{uw}\frac{\partial U}{\partial r} + \\ &-2\overline{u\frac{\partial p}{\partial x}} + \frac{1}{Re}\left\{\frac{1}{r}\frac{\partial}{\partial r}r\frac{\partial\overline{uu}}{\partial r}\right\} + \\ -\frac{2}{Re}&\left\{\overline{\left(\frac{\partial u}{\partial r}\right)^2} + \overline{\left(\frac{1}{r}\frac{\partial u}{\partial\theta}\right)^2} + \overline{\left(\frac{\partial u}{\partial x}\right)^2}\right\}\end{aligned} \tag{A.1}$$

$$\begin{aligned}\frac{\partial\overline{vv}}{\partial t} &= -\frac{1}{r}\frac{\partial r\overline{wvv}}{\partial r} - \frac{2}{r}\overline{wvv} - 2\overline{vw}\frac{\partial V}{\partial r} + \\ &-2\overline{vw}(\frac{V}{r} + S) - 2\overline{\frac{1}{r}v\frac{\partial p}{\partial\theta}} + \\ &+\frac{1}{Re}\left\{\frac{1}{r}\frac{\partial}{\partial r}r\frac{\partial\overline{vv}}{\partial r}\right\} - \frac{2}{Re}\left\{\frac{\overline{vv}}{r^2} - \frac{\overline{ww}}{r^2}\right\} + \\ -\frac{2}{Re}&\left\{\overline{\left(\frac{\partial v}{\partial r}\right)^2} + \overline{\left(\frac{1}{r}\frac{\partial v}{\partial\theta} + \frac{w}{r}\right)^2} + \overline{\left(\frac{\partial v}{\partial x}\right)^2}\right\}\end{aligned} \tag{A.2}$$

$$\begin{aligned}\frac{\partial\overline{ww}}{\partial t} &= -\frac{1}{r}\frac{\partial r\overline{www}}{\partial r} + \frac{2}{r}\overline{wvv} + 2\overline{vw}\frac{\partial V}{\partial r} + \\ &+2\overline{vw}(\frac{V}{r} - S) - 2\overline{w\frac{\partial p}{\partial r}} + \\ &+\frac{1}{Re}\left\{\frac{1}{r}\frac{\partial}{\partial r}r\frac{\partial\overline{ww}}{\partial r}\right\} - \frac{2}{Re}\left\{\frac{\overline{ww}}{r^2} - \frac{\overline{vv}}{r^2}\right\} + \\ -\frac{2}{Re}&\left\{\overline{\left(\frac{\partial w}{\partial r}\right)^2} + \overline{\left(\frac{1}{r}\frac{\partial w}{\partial\theta} - \frac{v}{r}\right)^2} + \overline{\left(\frac{\partial w}{\partial x}\right)^2}\right\}\end{aligned} \tag{A.3}$$

$$
\begin{aligned}
\frac{\partial \overline{uv}}{\partial t} = &-\frac{1}{r}\frac{\partial r\overline{uvw}}{\partial r} - \frac{\overline{uvw}}{r} + \\
&-uw\frac{\partial V}{\partial r} - \overline{vw}\frac{\partial U}{\partial r} + \\
&-\overline{uw}(\frac{V}{r} + S) + \\
&-\overline{\frac{1}{r}u\frac{\partial p}{\partial \theta}} - \overline{v\frac{\partial p}{\partial x}} + \\
&+\frac{1}{Re}\left\{\frac{1}{r}\frac{\partial}{\partial r}r\frac{\partial \overline{uv}}{\partial r}\right\} - \frac{1}{Re}\frac{\overline{uv}}{r^2} + \\
&-\frac{2}{Re}\left\{\overline{\frac{\partial u}{\partial r}\frac{\partial v}{\partial r}} + \overline{\left(\frac{1}{r}\frac{\partial v}{\partial \theta} + \frac{w}{r}\right)\left(\frac{1}{r}\frac{\partial u}{\partial \theta}\right)} + \overline{\frac{\partial u}{\partial x}\frac{\partial v}{\partial x}}\right\}
\end{aligned}
\tag{A.4}
$$

$$
\begin{aligned}
\frac{\partial \overline{uw}}{\partial t} = &-\frac{1}{r}\frac{\partial r\overline{uww}}{\partial r} + \frac{1}{r}\overline{uvv} + \\
&-\overline{ww}\frac{\partial U}{\partial r} + \overline{uv}\frac{V}{r} + \\
&+\overline{uv}(\frac{V}{r} + S) - \overline{w\frac{\partial p}{\partial r}} - \overline{u\frac{\partial p}{\partial x}} + \\
&+\frac{1}{Re}\left\{\frac{1}{r}\frac{\partial}{\partial r}r\frac{\partial \overline{uw}}{\partial r}\right\} - \frac{1}{Re}\frac{\overline{uw}}{r^2} + \\
&-\frac{2}{Re}\left\{\overline{\frac{\partial u}{\partial r}\frac{\partial w}{\partial r}} + \overline{\left(\frac{1}{r}\frac{\partial w}{\partial \theta} - \frac{v}{r}\right)\left(\frac{1}{r}\frac{\partial u}{\partial \theta}\right)} + \overline{\frac{\partial w}{\partial x}\frac{\partial u}{\partial x}}\right\}
\end{aligned}
\tag{A.5}
$$

$$
\begin{aligned}
\frac{\partial \overline{vw}}{\partial t} = &-\frac{1}{r}\frac{\partial r\overline{vww}}{\partial r} - \frac{\overline{vww}}{r} + \frac{\overline{vvv}}{r} + \\
&-\overline{ww}\frac{\partial V}{\partial r} + \overline{vv}\frac{V}{r} + \\
&-\overline{ww}(\frac{V}{r} + S) + \overline{vv}(\frac{V}{r} + S) + \\
&-\overline{\frac{1}{r}w\frac{\partial p}{\partial \theta}} - \overline{v\frac{\partial p}{\partial r}} + \\
&+\frac{1}{Re}\left\{\frac{1}{r}\frac{\partial}{\partial r}r\frac{\partial \overline{vw}}{\partial r}\right\} - \frac{4}{Re}\frac{\overline{vw}}{r^2} + \\
&-\frac{2}{Re}\left\{\overline{\frac{\partial v}{\partial r}\frac{\partial w}{\partial r}} + \overline{\left(\frac{1}{r}\frac{\partial w}{\partial \theta} + \frac{v}{r}\right)\left(\frac{1}{r}\frac{\partial v}{\partial \theta} - \frac{w}{r}\right)} + \overline{\frac{\partial w}{\partial x}\frac{\partial v}{\partial x}}\right\}
\end{aligned}
\tag{A.6}
$$

Bibliography

ABRAMOVICH, G. N. 1963 *The theory of turbulent jets*. MIT Press.

ALFREDSSON, P. H. & JOHANSSON, A. V. 1982 Experimental studies of turbulent channel flow. Technical Report, Dept. Mechanics, KTH, Stockholm, Sweden.

ALFREDSSON, P. H., JOHANSSON, A. V., HARITONIDIS, J. H. & ECKELMANN, H. 1988 The fluctuating wall-shear stress and the velocity field in the viscous sublayer. *Phys. Fluids* **31**, 1026–1033.

BARNES, D. & KERSWELL, R. 2000 New results in rotating Hagen-Poiseuille flow. *J. Fluid Mech.* **417**, 103–126.

BEÉR, J. M. & CHIGIER, N. A. 1972 *Combustion aerodynamics*. Applied Science Publishers LTD, London.

BILLANT, P., CHOMAZ, J.-M. & HUERRE, P. 1998 Experimental study of vortex breakdown in swirling jets. *J. Fluid Mech.* **376**, 183–219.

BRADSHAW, P. 1969 The analogy between streamline curvature and buoyancy in turbulent shear flow. *J. Fluid Mech.* **36**, 177–191.

CHIGIER, N. A. & CHERVINSKY, A. 1967 Experimental investigation of swirling vortex motion in jets. *J. Appl. Mech.* **34**, 443–451.

EGGELS, J. 1994 Direct and large eddy simulation of turbulent flow in a cylindrical pipe geometry. PhD thesis, Delft University of Technology, The Netherlands.

EGGELS, J. G. M., UNGER, F., WEISS, M. H., WESTERWEEL, J., ADRIAN, R. J., FRIEDRICH, R. & NIEUWSTADT, F. T. M. 1994 Fully developed turbulent pipe flow: a comparison between direct numerical simulation and experiment. *J. Fluid Mech.* **268**, 175–209.

FACCIOLO, L. & ALFREDSSON, P. 2004 The counter-rotating core of a swirling turbulent jet issued from a rotating pipe flow. *Phys. Fluids* **16**, L71–L73.

FACCIOLO, L., TILLMARK, N. & TALAMELLI, A. 2003 Experimental investigation of jets produced by rotating fully developed pipe flow. In *Proc. Third Int. Symp. Turbulence and Shear Flow Phenomena, Sendai*, pp. 1217–1222.

FAROKHI, S., TAGHAVI, R. & RICE, E. J. 1988 Effect of initial swirl distribution on the evolution of a turbulent jet. *AIAA J.* **27**, 700–706.

FAROKHI, S., TAGHAVI, R. & RICE, E. J. 1992 Modern development in shear flow control with swirl. *AIAA J.* **30**, 1482–706.

FEIZ, A., OULD-ROUIS, M. & LAURIAT, G. 2003 Large eddy simulation of turbulent flow in a rotating pipe. *Int. J. Heat Fluid Flow* **24**, 412–420.

HIRAI, S., TAKAGI, T. & MATSUMOTO, M. 1988 Predictions of the laminarization phenomena in an axially rotating pipe flow. *J. Fluids Engng.* **110**, 424–430.

HOWARD, L. & GUPTA, A. 1962 On the hydrodynamic and hydromagnetic stability of swirling flows. *J. Fluid Mech.* **14**, 463–476.

HU, G.-H., SUN, D.-J. & YIN, X.-Y. 2001 A numerical study of dynamics of a temporally evolving swirling jet. *Phys. Fluids* **13**, 951–965.

HUSSAIN, A. K. M. F. 1986 Coherent structures and turbulence. *J. Fluid Mech.* **173**, 303–356.

IMAO, S., ITOH, M. & HARADA, T. 1996 Turbulent characteristics of the flow in an axially rotating pipe. *Int. J. Heat Fluid Flow* **17**, 444–451.

IMAO, S., ITOH, M., YAMADA, Y. & ZHANG, Q. 1992 The characteristics of spiral waves in an axially rotating pipe. *Exp. Fluids* **12**, 277–285.

JUNG, D., GAMARD, S. & GEORGE, W. 2004 Downstream evolution of the most energetic modes in a turbulent axisymmetric jet at high Reynolds number. Part 1. The near field region. *J. Fluid Mech.* **514**, 173–204.

KHORRAMI, M. R. 1995 Stability of a compressible axisymmetric swirling jet. *AIAA J.* **4**, 650–658.

KIKUYAMA, K., MURAKAMI, M., NISHIBORI, K. & MAEDA, K. 1983 Flow in an axially rotating pipe. *Bull. JSME* **26**, 506–513.

KIM, J., MOIN, P. & MOSER, R. 1987 Turbulence statistics in fully developed channel flow at low reynolds number. *J. Fluid Mech.* **177**, 133–166.

KOMORI, S. & UEDA, H. 1985 Turbulent flow structure in the near field of a swirling round free jet. *Phys. Fluids* **28**, 2075–2082.

KURBATSKII, A. & POROSEVA, S. 1999 Modeling turbulent diffusion in a rotating cylindrical pipe flow. *Int. J. Heat and Fluid Flow* **20**, 341–348.

LEIBOVICH, S. & STEWARTSON, K. 1983 A sufficient condition for the instability of columnar vortices. *J. Fluid Mech.* **126**, 335–356.

LESSEN, M. & PAILLET, F. 1974 The stability of a trailing line vortex. Part 2. Viscous theory. *J. Fluid Mech.* **65**, 769–779.

LESSEN, M., SINGH, P. J. & PAILLET, F. 1974 The stability of a trailing line vortex. Part 1. Inviscid theory. *J. Fluid Mech.* **63**, 753–763.

LIEPMANN, D. & GHARIB, M. 1992 The role of streamwise vorticity in the near-field entrainment of round jets. *J. Fluid Mech.* **245**, 643–668.

LILLEY, D. G. 1999 Annular vane swirler performance. *J. Propul. Power* **15**, 248–252.

LIM, D. W. & REDEKOPP, L. G. 1998 Absolute instability conditions for variable density, swirling jet flows. *Eur. J. Mech. B/Fluids* **17**, 165–185.

LOISELEUX, T. & CHOMAZ, J. M. 2003 Breaking of rotational symmetry in a swirling jet experiment. *Phys. Fluids* **15**, 511–523.

LOISELEUX, T., CHOMAZ, J. M. & HUERRE, P. 1998 The effect of swirl on jets wakes: Linear instability of the Rankine vortex with axial flow. *Phys. Fluids* **10**, 1120–1134.

MALIN, M. & YOUNIS, B. 1997 Prediction of turbulent transport in an axially rotating pipe. *Int. Comm. Heat Mass Transfer* **24**, 89–98.

MARTIN, J. E. & MEIBURG, E. 1994 On the stability of the swirling jet shear layer. *Phys. Fluids* **6**, 424–426.

MARTIN, J. E. & MEIBURG, E. 1998 The growth and nonlinear evolution of helical perturbations in a swirling jet model. *Eur. J. Mech. B/Fluids* **17**, 639–651.

Maslowe, S. 1974 Instability of rigidly rotating flows to non-axisymmetric disturbances. *J. Fluid Mech.* **64**, 307–317.

Mayer, E. W. & Powell, K. G. 1992 Similarity solutions for viscous vortex cores. *J. Fluid Mech.* **238**, 487–507.

McIlwain, S. & Pollard, A. 2002 Large eddy simulation of the effects of mild swirl on the near field of a round free jet. *Phys. Fluids* **14**, 653–661.

Metha, R. D., Wood, D. H. & Clausen, P. D. 1991 Some effects of swirl on turbulent mixing layer development. *Phys. Fluids A* **3**, 2716–2724.

Michalke, A. 1984 Survey on jet instability theory. *Prog. Aerospace Sci.* **21**, 159–199.

Michalke, A. 1999 Absolute inviscid instability of a ring jet with back-flow and swirl. *Eur. J. Mech. B/Fluids* **18**, 3–12.

Moser, R. D., Kim, J. & Mansour, N. N. 1999 Direct numerical simulation of turbulent channel flow up to Re_τ=590. *Phys. Fluids A* **11**, 943–945.

Murakami, M. & Kikuyama, K. 1980 Turbulent flow in axially rotating pipes. *J. Fluids Eng.* **102**, 97–103.

Nagib, H., Lavan, Z. & Fejer, A. 1971 Stability of pipe flow with superposed solid body rotation. *Phys. Fluids* **14**, 766–768.

Oberlack, M. 1999 Similarity in non-rotating and rotating turbulent pipe flows. *J. Fluid Mech.* **379**, 1–22.

Oberlack, M. 2001 A unified approach for symmetries in plane parallel turbulent shear flows. *J. Fluid Mech.* **427**, 299–328.

Orlandi, P. 1997 Helicity fluctuations and turbulent energy production in rotating and non-rotating pipes. *Phys. Fluids* **9**, 2045–2056.

Orlandi, P. & Ebstein, D. 2000 Turbulent budgets in rotating pipes by DNS. *Int. J. Heat Fluid Flow* **21**, 499–505.

Orlandi, P. & Fatica, M. 1997 Direct simulations of turbulent flow in a pipe rotating about its axis. *J. Fluid Mech.* **343**, 43–72.

Österlund, J. M. 1999 Experimental studies of zero pressure-gradient turbulent boundary layer flow. PhD thesis, TRITA-MEK Tech. Rep. 1999:16, Dept. Mech., KTH, Stockholm, Sweden.

Österlund, J. M., Johansson, A., Nagib, H. M. & Hites, M. H. 2000 A note on the overlap region in turbulent boundary layers. *Phys. Fluids* **12**, 1–4.

Panda, J. & McLaughlin, D. K. 1994 Experiments on the instabilities of a swirling jet. *Phys Fluids* **6**, 263–276.

Park, S. H. & Shin, H. D. 1993 Measurement of entrainment characteristics of swirling jets. *Int. J. Heat Mass Tran* **136**, 4009–4018.

Pedley, T. 1968 On the instability of rapidly rotating shear flows to non-axisymmetric disturbances. *J. Fluid Mech.* **31**, 603–607.

Pedley, T. 1969 On the instability of viscous flow in a rapidly rotating pipe. *J. Fluid Mech.* **35**, 97–115.

Pratte, B. D. & Keffer, J. F. 1972 The swirling turbulent jet. *J. Basic Eng., Trans. ASME* **93**, 739–748.

Rahai, H. R. & Wong, T. W. 2001 Velocity field characteristics of turbulent jets from round tubes with coil inserts. *Appl. Thermal Eng.* **22**, 1037–1045.

Rayleigh, L. 1916 On the dynamics of revolving fluids. *Proc. R. Soc. London* **A 93**, 148–154.

Reich, G. & Beer, H. 1989 Fluid flow and heat transfer in an axially rotating pipe –I. Effect of rotation on turbulent pipe flow. *Int. J. Heat Mass Transfer* **32**, 551–562.

Rinck, K.-J. & Beer, H. 1998 Numerical calculation of the fully developed turbulent flow in an axially rotating pipe with a second-moment closure. *J. Fluids Engng.* **120**, 274–279.

Rose, W. G. 1962 A swirling round turbulent jet. *J. Appl. Mech.* **29**, 615–625.

Satake, S. & Kunugi, T. 2002 Direct numerical simulation of turbulent heat transfer in an axially rotating pipe flow. Reynolds shear stress and scalar flux budgets. *Int. J. Num. Methods Heat Fluid Flow* **12**, 958–1008.

Sislian, J. P. & Cusworth, R. A. 1986 Measurements of mean velocity and turbulent intensities in a free isothermal swirling jet. *AIAA J.* **24**, 303–309.

Speziale, C., Younis, B. & Berger, S. 2000 Analysis and modelling of turbulent flow in an axially rotating pipe. *J. Fluid Mech.* **407**, 1–26.

Synge, L. 1933 The stability of heterogeneous liquids. *Trans. R. Soc. Canada* **27**, 1–18.

Talamelli, A., Westin, K. J. A. & Alfredsson, P. A. 2000 An experimental investigation of the response of hot wire X-probes in shear flows. *Exp. Fluids* **23**, 425–435.

Thomas, F. O. 1991 structure of mixing layers and jets. *Appl. Mech. Rev.* **44**, 119–153.

Toplosky, N. & Akylas, T. 1988 Nonlinear spiral waves in rotating pipe flow. *J. Fluid Mech.* **190**, 39–54.

Tritton, D. & Davies, P. 1985 Instabilities in geophysical fluid dynamics. In *Hydrodynamic Instabilities and the Transition to Turbulence.* Topics in Applied Physics, vol. 45, 2nd edn. Springer.

Wallin, S. & Johansson, A. 2000 An explicit algebraic Reynolds stress model for incompressible and compressible turbulent flow. *J. Fluid Mech.* **403**, 89–132.

Weigand, B. & Beer, H. 1994 On the universality of the velocity profiles of a turbulent flow in an axially rotating pipe. *Appl. Sci. Res.* **52**, 115–132.

White, A. 1964 Flow of a fluid in an axially rotating pipe. *J. Mech. Engng. Sci.* **6**, 47–52.

Yang, Z. 2000 Large eddy simulation of fully developed turbulent flow in a rotating pipe. *Int. J. Numer. Meth. Fluids* **33**, 681–694.